Electronic Structure of Cobalt Octahedral Complexes in Aqueous Solution

im Fachbereich Physik Freien Universität Berlin
eingereichte Dissertation

zur Erlangung des akademischen Grades
eines Doktors der Naturwissenschaften (Dr. rer. nat.)

vorgelegt von

Sreeju Sreekantan Nair Lalithambika

Berlin, March 2019

Gutachter:

1. Dr. Bernd Winter
   Department of Molecular Physics, Fritz-Haber-Institut der Max-Planck-Gesellschaft, Berlin

2. Prof. Dr. Wolfgang Kuch
   Institut für Experimentalphysik, Freie Universität Berlin

Tag der Disputation: 29. Mai 2019

Abstract

This thesis reports on the electronic structure of aqueous cobalt octahedral complexes using soft X-ray spectroscopic techniques. Cobalt complexes have emerged as an essential group of molecules in the field of energy–material research, especially with focus on solar energy conversion and photocatalytic water splitting. Applying liquid-jet and flow-cell techniques, electronic structure details are elucidated by resonant inelastic scattering (RIXS), non-resonant X-ray emission (XE), resonant photoemission (RPE), partial fluorescence yield X-ray absorption (PFY-XA) and partial electron yield X-ray absorption (PEY-XA) methods. Ground-state density functional theory (DFT) calculations, DFT/restricted open shell configuration interaction singles (DFT/ROCIS), and time dependent-DFT methods are used for interpreting the experimental spectra.

I have studied the aqueous hexacyanocobaltate ($[Co(CN)_6]^{3-}$) complex using electron and photon detection methods, by exciting the Co (metal) L-edge and N (ligand) K-edge. Non-resonant photoelectron spectroscopy provides solute electron binding energies, whereas RPE spectra measured at the Co L-edge and N K-edge identify metal–ligand orbital overlaps. The binding energies of orbitals and their metal and ligand characters are qualitatively derived from the RPE and RIXS spectra, and DFT calculations supplement these findings. The calculated XA spectra of Co L-edge and N K-edge well reproduce the experimental PFY-XA and PEY-XA spectra. The comparison of experimental and calculated XA spectra enables the quantification of the main σ and π bonding interactions. Particularly, the strength of π-backbonding between metal and ligand is directly inferred from the intensity change of π^* and σ^* peaks in the Co L-edge and N K-edge XA spectra.

The other cobalt complexes studied here are the aqueous cobalt (II) tris-bipyridine and cobalt (III) tris-bipyridine($[Co(bpy)_3]^{2+}$ and $[Co(bpy)_3]^{3+}$) using RIXS spectroscopy. The PFY-XA spectra measured at the Co L-edges are intricate and necessitate consideration of high-spin (HS) and low-spin (LS) configurations of the molecules. DFT/ROCIS method is employed for calculating the Co L-edge XA spectra of different spin configurations of the molecules. It is observed that a linear combination of the calculated XA spectra of various spin states well reproduces the experimental spectra. For $[Co(bpy)_3]^{2+}$, the study reveals approximately 43% of LS and 57% HS character, whereas a much higher LS nature is observed for $[Co(bpy)_3]^{3+}$ with approximately 80% LS and 20% HS. The N K-edge PFY-XA spectra from both the samples exhibit similar features, and TD-DFT XA calculations substantiate these findings. The similarities of N K-edge PFY-XA spectra suggest the insensitivity of the ligand edge to spin states.

The final part of this thesis is presented as an outlook study where the experimental RIXS spectrum of aqueous $[Cr(CN)_6]^{3-}$ is compared with DFT/ROCIS-generated RIXS maps. The calculated RIXS maps are generated by selected molecular orbitals based on their metal and ligand character, respectively.

Kurzfassung

Diese Arbeit befasst sich mit oktaedrischen Kobaltkomplexen in Wasser, die mittels Spektroskopie im Bereich weicher Röntgenstrahlung untersucht wurden. Im Forschungsfeld der Energie-Materialien haben sich insbesondere die Kobaltkomplexe als eine der Hauptmolekülgruppen für die Konversion von Sonnenenergie und photokatalytischer Wasserspaltung etabliert. Durch die Kombination mehrerer zukunftsweisender experimenteller Techniken, darunter Flüssigjet und Durchflusszellen zur Untersuchung von Flüssigkeiten, sowie neuartiger Spektroskopietechniken, wie Resonanter Inelastischer Röntgenstreuung (RIXS), Röntgenemission (XE), Resonanter Elektronenemission (RPE), partieller Röntgen- und Elektronenabsorption (PFY-XA, PEY-XA), wurde die elektronische Struktur auf komplexe Details untersucht. Zusätzliche theoretische Betrachtungen mit modernsten Techniken (DFT, DFT/ROCIS, TD-DFT) wurden bei der Interpretation der Spektren eingesetzt.

Der erste zu untersuchende Komplex war Hexacyanokobaltat $[Co(CN)_6]^{3-}$, welcher mit den verschiedenen Techniken an der Kobalt L-Kante (Metall) und seiner Stickstoff K-Kante (Ligand) angeregt wurde. Hierbei hat die nicht-resonante Elektronenemission Einsicht in die Elektronenbindungsenergien geliefert und, in Kombination mit den RPE Spektren, Untersuchungen vom Metall–Liganden Orbitalüberlapp ermöglicht. Unter Zuhilfenahme von XE und RIXS Spektroskopie konnten die Bindungsenergien und der Orbitalcharakter bestimmt und mit theoretischen Berechnungen unterstützt werden. Ebenfalls wiesen die über Berechnungen erlangten XA Spektren eine “Ein-Zu-Eins" Übereinstimmung mit den experimentellen PFY-XA und PEY-XA Spektren auf. Durch die Kombination aller Techniken konnte schlussfolgernd eine quantitative Bestimmung der σ- und π-Bindungsinteraktionen erfolgen. Insbesondere die überraschende Stärke der π-Rückbindung sei hier genannt, welche mithilfe der Intensitätsvariationen der π^*- und σ^*- Signale direkt erklärt werden kann.

Weiterhin berichte ich in dieser Arbeit über die elektronische Struktur von $[Co(bpy)_3]^{2+}$ und $[Co(bpy)_3]^{3+}$ in Wasser. Insbesondere die PFY-XA Spektren an der Kobalt L-Kante sind komplex und verlangen eine tiefgehende Analyse der Spin-Konfigurationen (high spin (HS), low spin (LS)) der Moleküle. Zu diesem Zweck wurden verschiedenste Spin-Zustände mit DFT/ROCIS berechnet und analysiert. Es zeigt sich, dass nur eine lineare Kombination der berechneten XA-Spektren die Experimente korrekt darstellen kann. Demnach besitzt $[Co(bpy)_3]^{2+}$ 43% LS und 57% HS Charakter und $[Co(bpy)_3]^{3+}$ besitzt 20% HS und 80% LS Charakter. Vergleichende Untersuchungen an der Stickstoff K-Kante zeigen unwesentliche Unterschiede zwischen beiden Molekülen; dieses Verhalten wird durch berechnete TD-DFT XA Spektren bestätigt. Insbesondere die Ähnlichkeiten im Stickstoff K-Kanten PFY-XA Spektrum legen eine Unempfindlichkeit der Ligandenkante auf Änderungen des Spin-Zustandes nahe.

Im Ausblick stelle ich experimentelle RIXS Spektren von $[Cr(CN)_6]^{3-}$ in Wasser vor, welche mit RIXS-Maps, basierend auf theoretischen Berechnungen, verglichen werden.

Contents

1. Introduction

The use of electromagnetic radiation for the study of materials dates back centuries. Among them, a class of radiation called 'X-rays' has played an essential role in human scientific endeavors over the last century ever since their discovery by Wilhelm Conrad Röntgen in 1895 [1]. The energy of X-rays ranges from 10^2 - 10^6 eV. A broad classification is made such that X-rays up to 1000 eV are termed as 'soft X-rays', between 1000 and 5000 eV is the region of 'tender X-rays', and photon energies above 5000 eV are referred to as 'hard X-rays' [2]. Presently, synchrotron and free-electron-laser facilities around the world provide these unique radiations with high brilliance for structural studies of matter. A synchrotron radiation facility produces the broad X-ray spectral energy range by accelerating electrons to nearly the speed of light and bending them in a static magnetic field.

Understanding matter in the fullest details is of prime importance in the field of physics, chemistry, biology, and material science. The physical and chemical properties of matter (condensed, gas, or liquid phase) are determined by the electronic configuration, especially in the valence region. Each electron is tied to an atomic or molecular orbital with a specific energy, its binding energy. The soft X-rays have sufficiently large energies to also ionize core levels which makes them an essential probe for studying the electronic structure of most of the matter around us and materials we develop. A variety of methods based on soft X-rays have been established.

In this thesis, I present the study on aqueous-phase transition metal complexes using two synchrotron-radiation specific spectroscopic methods, resonant inelastic X-ray scattering (RIXS) and resonant photoelectron (RPE) spectroscopy. The former analyzes X-rays emitted from the sample while the latter detects the simultaneously emitted electrons. Both these techniques are well established, yet measurements from aqueous-phase systems pose a challenge due to the vacuum conditions typically necessary for soft X-ray measurements.

Aqueous solution phase electronic structure studies of molecules are relevant in energy material research. This includes solar cell and catalysis research, requiring molecules which can be modified for better device performance. Standard analytical methods like UV-Vis and infrared spectroscopies can be used to gain information about molecules of interest, but the information of electronic structure requires the use of synchrotron-based X-ray spectroscopies [3]. Here, one exploits the unique characteristics of synchrotron X-rays: (i)

X-ray energies are tunable over a wide range, (ii) X-ray energy can be precisely matched with the valence or core orbital energies of specific atoms, thus enabling the so called resonance spectroscopies, (iii) high flux and brilliance of the X-rays are a requirement when studying dilute systems [2, 4, 5].

In the quest for earth-abundant materials for sustainable renewable energy applications, compounds with cobalt–active centers are being extensively investigated over the past decades [6]. Applications ranging from magnetic materials [7], catalysts, and electrode materials, to specific photo-active centers functional in water splitting and dye-sensitized solar cell systems use cobalt–containing complexes as main ingredients [8–10]. For example, in the case of water splitting catalysis, reduction process of proton into hydrogen can be achieved with cobalt(I) porphyrins, cobalt phthalocyanines and various octahedral cobalt-polypyridyl molecules [11–13]. These are efficient and cheap alternatives compared to noble metal catalysts like platinum and ruthenium. The cobalt-polypyridyl group can also act as efficient electron mediator in various catalytic systems. The important factor in such applications is the molecules' easily tunable redox potential. For example, the electrode potential of $[Co(bpy)_3]^{2+/3+}$ on TiO_2 is 0.56 V. When the ligand is changed to phenanthroline,*i.e.*, $[Co(phen)_3]^{2+/3+}$, the potential becomes 0.62 V [14]. This implies that redox ability is directly linked to the metal–ligand bonding [15].

In a broader context, the electronic structure of these materials is characterized by hybridization, charge transfer and spin-state, and plays a crucial role in determining the overall chemistry in such multi-component systems. There exist a plethora of articles regarding the varieties of Co-polypyridine complexes functioning as catalysts, electrode materials, and as photosensitizers [16, 17]. Despite the large application potential of these materials information on the electronic structure is rather scarce, especially in aqueous phase which reasonably well mimics the ambient conditions that exist in a working solar cell or a water-splitting catalytic reactor [14, 18]. Questions naturally come to one's mind such as: (1) "what is the local structure of the molecule around the Co metal center?", (2) "what is the strength of bonding between the metal center and the ligand bonding?", (3) "will the environment affect the local structure of the molecule?", (4) "what are the details about various charge-transfer processes occurring in the molecule?", and (5) "whether the molecule is existing in high spin or low spin state?" All these questions can be addressed using soft X-ray spectroscopies. Owing to the tunability of X-rays, the above mentioned questions can be investigated by probing the metal center upon exciting the Co L-edge and also by exciting the K-edge of ligands.

In the past decade, many studies on transition metal (TM) complexes in solution phase have been reported employing electron- and photon-out spectroscopy methods [19, 20]. Mostly, the main studies were focused on the central TM atoms. These studies range from simple Fe^{2+} ions in solution [21, 22] to large porphyrin molecules [23–25]. Some studies have also reported the electronic structure of solvent molecules (pure and in solution form) using photon-out spectroscopy methods [26–28]. For example, by studying

the X-ray absorption spectrum of the oxygen atom in pure water and various aqueous solutions ($FeCl_3$, $CrCl_3$ and $AlCl_3$) Näslund et al. [28] showed the orbital mixing of solvent and solute molecules. The electron-out/ photoelectron spectroscopy from the liquid phase can determine the binding energies of solute and solvent molecules. This experimental determination of binding energy is crucial to the general field of chemistry [29]. Studies combining electron and photon relaxation channels are scarce [30]. It should be emphasized that a major section of this thesis reports on combining these two methods for studying the electronic structure of the aqueous solution phase, exemplified for hexacyanocobaltate model complex.

1.1 Outline of the Thesis

This thesis is organized as follows. Section 1.2 presents a brief introduction to X-ray–matter interaction, and the resulting electron and photon emission channels. Section 1.3 introduces sigma and pi bonding discussed in this thesis. In Chapter 2, Section 2.1 describes core-level electron and photon-out spectroscopic methods. Section 2.2 describes the BESSY II (Berliner Elektronenspeicherring-Gesellschaft für Synchrotronstrahlung) storage ring, various beamlines and experimental stations used in this work. Section 2.3 gives a brief description of the sample handling techniques used. Short accounts of various computational methods used for simulating the spectra are described in Section 2.4. The following Chapter 3 presents the major findings of this study, which is divided into three main sections. Section 3.1 investigates the detailed electronic structure of the $[Co(CN)_6]^{3-}$ complex in aqueous solutions using electron- and photon-out methods. Section 3.2 explores the ground-state spin configurations of aqueous $[Co(bpy)_3]^{2+}$ and $[Co(bpy)_3]^{3+}$. Section 3.3 is presented as a prospective study, where preliminary RIXS results from the aqueous $[Cr(CN)_6]^{3-}$ studies are introduced. Chapter 4 presents the summary and outlook of this study.

1.2 X-ray–Matter Interaction

The complexity of electronic structure studies increases from gaseous molecules to condensed matter phases. One of the essential analytical tools for unravel the complexity is the use of X-ray based techniques. Some of these techniques are applied, based on absorption, emission (radiative and non-radiative) and diffraction of X-rays. The absorption process occurs when X-ray photons with certain energy impinge on matter causing an electronic transition. The absorption process can result in various secondary processes depending on the energy of the X-rays. If the energy of the X-rays is higher than a particular electron binding energy, a direct electron gets ejected. This is the photoelectron; its kinetic energy equals the incident energy of the X-ray photon minus the binding energy of the particular shell. This process is called photoionization which leaves the system in an ionized

state. Depending on the photon energy, the ionized atom can have a core-level vacancy or a valence-level vacancy. In the case of core vacancy, the electronically highly excited atom lowers its energy by two competing processes. First, by filling the core-level vacancy by an upper-lying electron and releasing the excess energy as a photon. This process is called fluorescence emission. Second, by emitting an electron (non-radiative process), called Auger electron (or more generally autoionization) decay with a characteristic energy, which is the difference between the excited state and the final state. A more detailed discussion on various emission processes is available in Chapter 2, Section 2.1. The quantum yields of these two processes depend on the atomic number as illustrated in Figure 1.1 [31–33]. The competition favors Auger electron yield for low atomic number (Z) atoms, and fluorescence yield is favorable for high Z atoms [31].

Another important factor which influences the X-ray–matter interaction is the scattering cross section. Scattering cross section (σ) defines the number of photons interacting with the system under investigation. Figure 1.2(a) shows the total absorption cross sections for Co, Cr and N atoms.

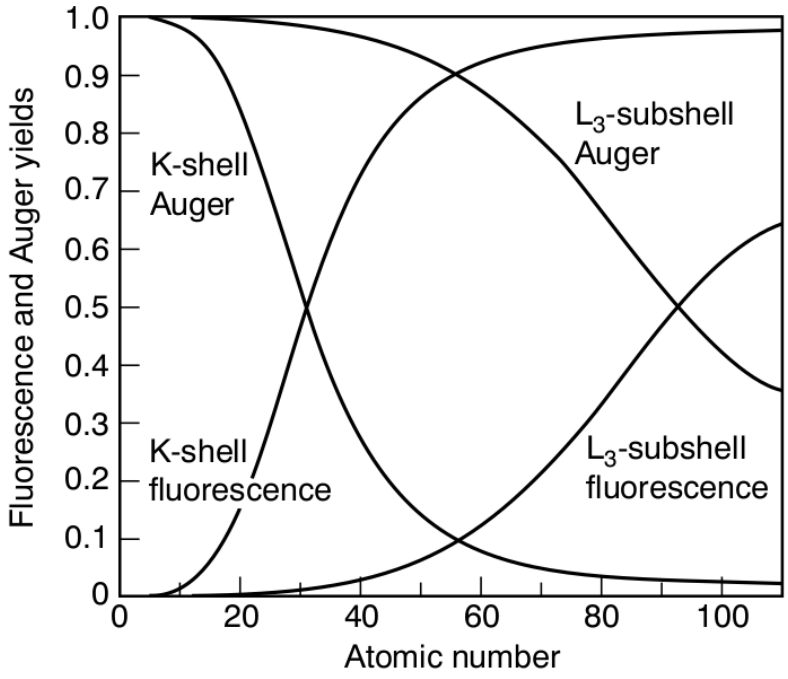

Figure 1.1: Auger and fluorescence yield for K and L_3 subshell as a funtion of atomic numbers. Image taken from reference [31].

The total scattering cross section decreases as a function of photon energy E as $\sigma_{ph} \propto \frac{1}{E^3}$ [34]. The sharp edged features in Figure 1.2(a) occur due to sudden ejection of electrons into an unoccupied level when the photon energy matches the binding energy of the electron; this match in photon energy is also called resonance energy. Simplified shell and orbital divisions of an atom are shown in Figure 1.2(b), with arrows indicating various absorption edges (K, L and M edges). The phenomenon of rapid increase and variations in absorption

cross sections at and across the resonance energies of atomic orbitals are extensively used to study the electronic structure of molecules and solid-sate phases. These variations in absorption cross sections also follow certain selection rules. Chapter 2 discusses these selection rules and various X-ray based absorption and emission pathways.

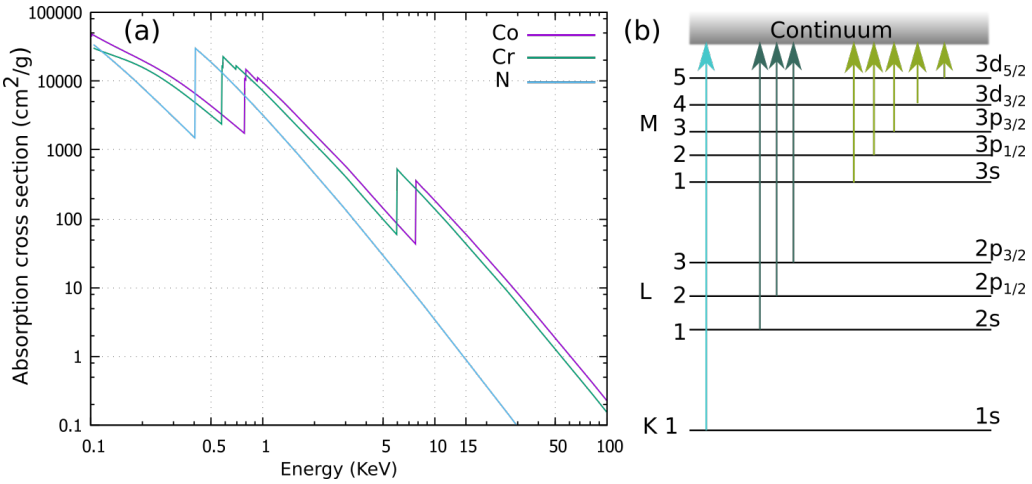

Figure 1.2: (a) Variation of total absorption cross sections of Co, Cr and N atoms as a function of photon energy in log scale. Sharp increase in absorption occurs when the photon energy equals the binding energy of a particular shell and ejects an electron to the vacuum, these transitions are illustrated in (b). Data for (a) obtained from `https://physics.nist.gov/PhysRefData/FFast/html/form.html`, Chantler *et al.* [35].

1.3 Ligand Field Theory

Bonding in TM complexes can be described using different theories, such as crystal field theory, ligand field theory or angular overlap method. The most suitable one for describing the valence molecular orbital (MO) of metal complexes is the ligand field theory [15, 36]. This thesis studies molecules with (near) octahedral symmetry. According to the O_h

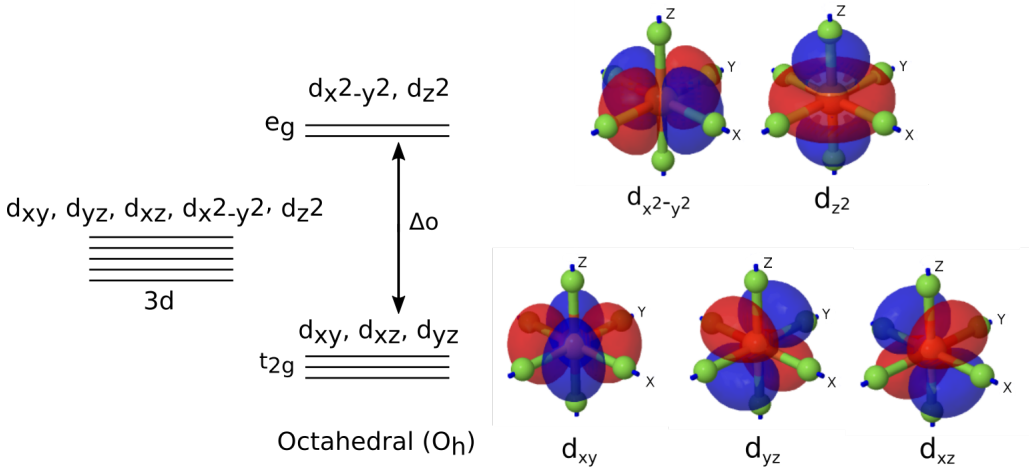

Figure 1.3: The octahedral crystal field splitting and the boundary surfaces of 3*d* orbitals [37].

symmetry table, the d orbitals in octahedral ligand field split into two degenerate groups, such as t_{2g} (d_{xy}, d_{xz} and d_{yz}) and e_g ($d_{x^2-y^2}$, d_{z^2}). Figure 1.3 illustrates the octahedral splitting and different d orbital symmetries. The energetic difference between t_{2g} and e_g is referred to as Δ_o or $10D_q$. The Δ_o value varies for different complexes, and depends on the strength of the ligand. A strong ligand field results in a large Δ_o, whereas weak ligand field results in small Δ_o values. The strength of the ligand field also influences the electronic distribution in valence d orbitals for d^4 to d^7 complexes which leads to high-spin and low-spin states in complexes. A strong ligand field (e.g., CN^-) pushes the complex to a low-spin state state, whereas a weak field ligand leads to high-spin state complex, depending on whether Δ_o is greater than the energy for pairing two electrons or not [36].

According to ligand field theory the bonding occurs by the overlap of symmetry-selected metal and ligand orbitals [15]. This results in two MOs, namely bonding and antibonding orbitals. Sigma (σ) bonding and pi (π) bonding are the two central bonding schemes in TM complexes. The valence s, p and $d(e_g)$ orbitals can form sigma bonding and antibonding orbitals with symmetry allowed ligand σ orbitals. Whereas the metal $d(t_{2g})$ orbitals remain as nonbonding orbitals under sigma bonding condition. The formation of a metal–ligand sigma bonding is illustrated in Figure 1.4(a).

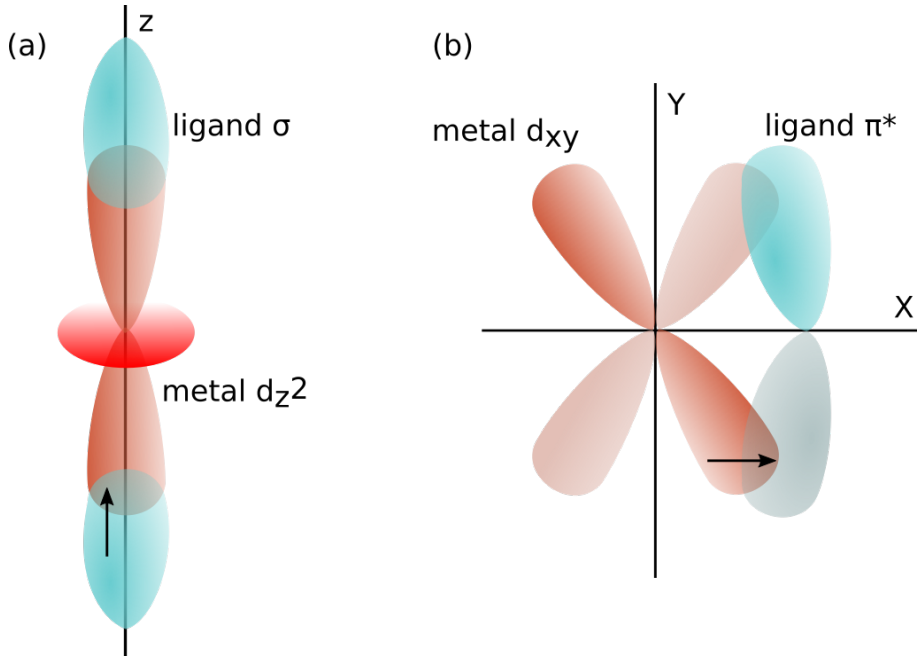

Figure 1.4: The sigma (a) and pi (b) bonding between metal $3d$ and ligand $2p$ orbitals. The arrows indicate electron donation direction; ligand→metal σ charge transfer bonding in (a), and metal→ligand charge transfer π bonding in (b) [15, 36].

A π bonding or antibonding orbital occurs when the metal t_{2g} orbitals having π symmetry, is in the vicinity of ligand orbitals, with π local symmetry. This is depicted in Figure 1.4(b). The π symmetry of the ligand can lead to two distinct situations. In one case the ligand has a filled π orbitals. Then the π bonding results by donating the filled

electron density to the metal side; this is called π donation. In the other case the ligand possesses empty π orbital to which the metal can donate or back-donate electron density. This is termed π back-donation, and is illustrated by the arrow in Figure 1.4(b). π bonds formed through π donation and π back-donation lead to significant electronic stabilization [36].

This thesis examines the bonding of Co and Cr in an octahedral CN^- ligand field. The CN^- can engage in simultaneous σ and π bonding with the metal centers, through σ donation, and π back-donation. The valence levels of CN^- are characterized by filled σ orbital and two empty π^* orbitals. The sigma donation occurs when electron density is transferred from the filled σ orbitals to the metal $3de_g$ orbitals. The π bonding interactions occur through metal $3dt_{2g}$ orbitals with 2π MOs of CN^-. The schematic energy level diagram illustrating the π bonding or π back-donation is shown in Figure 1.5.

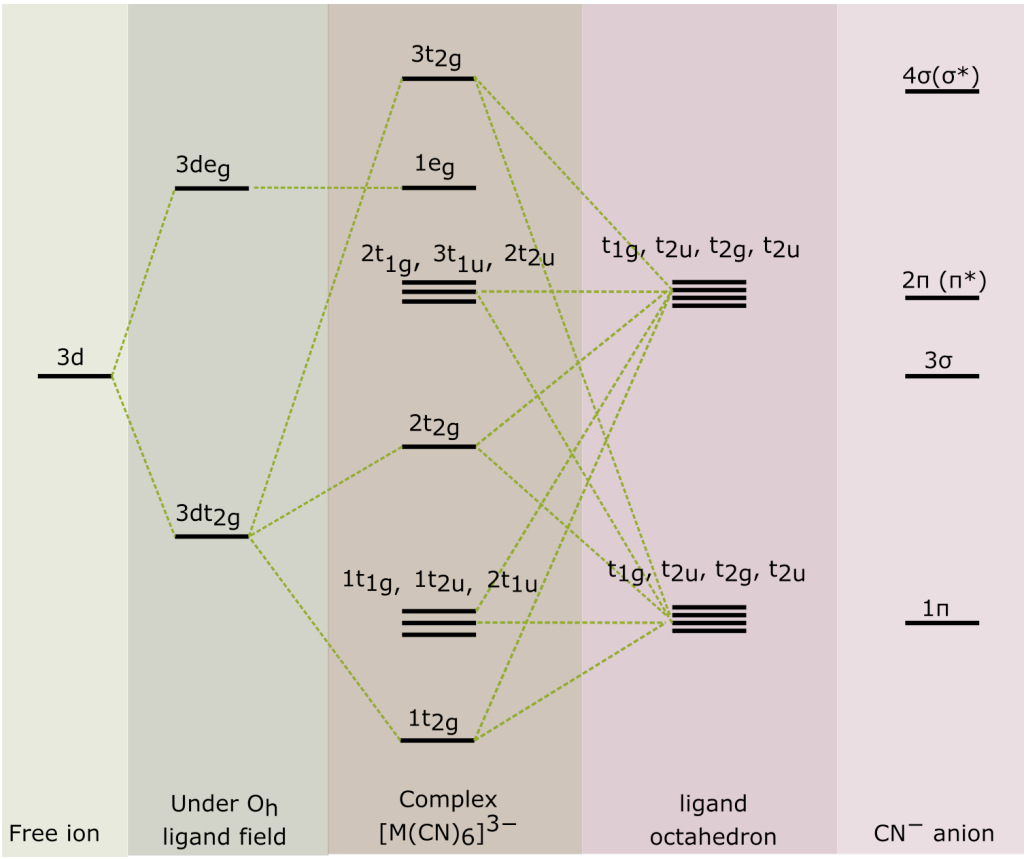

Figure 1.5: Schematic energy level diagram for an $[M(CN)_6]^{3-}$ complex, where M=Co or Cr [38].

The 2π MOs have irreducible representations as t_{1g}, t_{2u}, t_{2g} and t_{2u} symmetries under octahedral symmetry [38]. For the complex $[M(CN)_6]^{3-}$, the metal–ligand overlap leads to two occupied $1t_{2g}$ (bonding), $2t_{2g}$ (antibonding) orbitals and an unoccupied $3t_{2g}$ molecular orbital; see Figure 1.5. For the case of $[Co(CN)_6]^{3-}$ the $2t_{2g}$ level is fully occupied, leading to a ground-state configuration of ${2t_{2g}}^6$; for $[Cr(CN)_6]^{3-}$ it is a partially filled state.

In certain electronic situations, there exist deviations from octahedral symmetry. These

deviations are explained by the Jahn-Teller theorem [39] and are common in octahedral symmetry complexes. The theorem states that degeneracy of orbitals is removed in the case of an unequal distribution of electrons. An example is the low-spin configuration of Co^{2+} studied in this thesis (Chapter 3, Section 3.2), where the e_g ($t_{2g}{}^6$, $e_g{}^1$) level is singly occupied. The distortion appears as an elongation or compression along a particular direction of the complex.

2. Experimental and Theoretical Details

This chapter provides a brief insight on the fundamental aspects of soft X-ray based core-level spectroscopy. I arranged this chapter in the way that the beginning sections describe various X-ray spectroscopic methodologies, followed by details about BESSY II X-ray beamlines and experimental stations used during my studies. The final section describes theoretical basics of density functional theory (DFT), time dependent-DFT (TD-DFT) and post-Hartree Fock methods. A short description about how these methodologies are implemented in the ORCA program package for obtaining electronic ground-state and excited-state information is also provided.

2.1 Introduction to Core-level Spectroscopy

Synchrotron radiation experiments are at the pivotal point of physics, chemistry and material science in understanding matter to the very finest details. Among them X-ray based core-level spectroscopies are unique in probing detailed electronic structure, owing to their element and environment specific nature. The element specific investigation is facilitated by the ability to tune the photon energy over a wide range. For a model single atom, valence and core levels are shown in Figure 2.1. The interaction with X-rays can be divided into two cases. The first one, in which the incident photon energy is tuned precisely to the difference between the core level and empty valence level energies is the so-called resonant excitation. In the second case, the photon energy is larger than the core–level binding energy, leading to non-resonant excitations (ionization). The conventional laboratory-based X-ray photoelectron spectroscopy (XPS) setup, providing fixed photon energies is usually applicable for the study of non-resonant processes, typically used to determine electron binding energies.

Central to all these processes is the core hole. It is created by the absorption of an incident X-ray photon, creating a vacancy in the core level and leaving the system under investigation in an excited state. The system returns to the electronic ground state when an energetically higher-lying electron fills the core hole; this happens within the core-hole lifetime, typically $\sim 10^{-15}$ seconds (femtosecond regime). At this point, the valence

electrons undergo subtle rearrangements accompanied by different radiative and/or non-radiative relaxation processes.

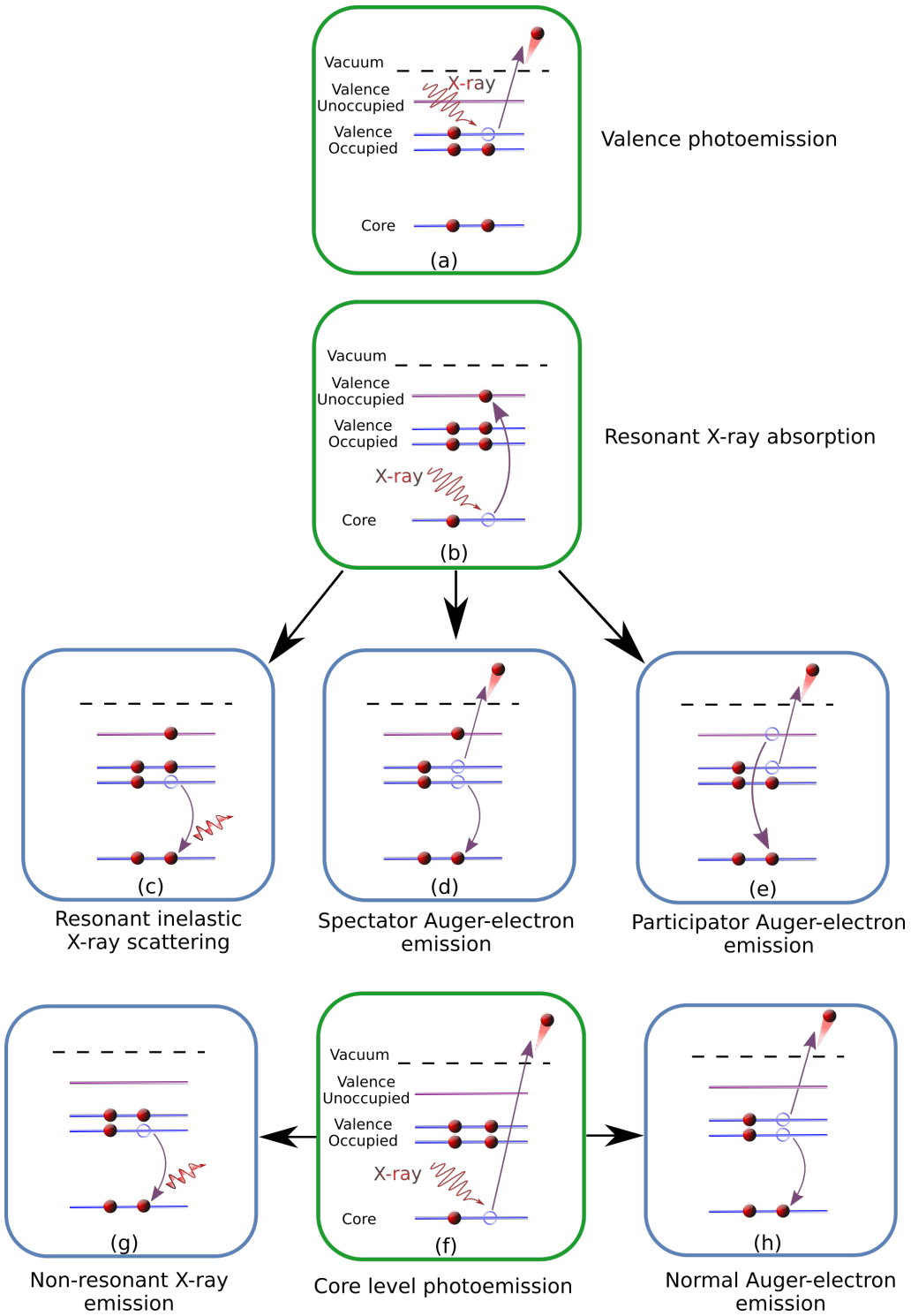

Figure 2.1: Schematic representations of different emission/absorption channels from a molecular system upon interaction with an X-ray photon. Direct absorption/emission and secondary emission processes are shown in green and blue boxes.

Figure 2.1 is a simple schematic representation of various relaxation channels available upon X-ray valence ionization (a), resonant excitations (b), and core-level ionizations (f), respectively. Here, I present a molecular system with discrete occupied and unoccupied valence levels, which in this thesis are hybridized metal ($3d$)- ligand ($2p$) orbitals. The core level represents $2p$ orbitals of cobalt and chromium and $1s$ orbital of nitrogen atoms. Figure 2.1(a) depicts valence photoemission, originating from the valence occupied orbitals after interacting with a photon of typically less than 200 eV energy [40]. And here we are mostly interested in the lowest ionization energy which is crucial for understanding chemical reactivity, and also serving here in the interpretation of the XA spectra [29]. This will be detailed in Section 3.1.3.

Figure 2.1(b) shows the resonant X-ray absorption process. The resulting core-excited state can decay via two processes. The first one, radiative decay as shown in Figure 2.1(c), is also known as fluorescence emission or resonant X-ray emission. The second process, non-radiative or resonant Auger electron emission, which takes effect either through the spectator Auger electron emission, shown in Figure 2.1(d), or as a participator Auger emission is shown in Figure 2.1(e). When the photon energy is increased well above the resonance, the core-level electrons get ejected into the continuum, yielding core-level photoemission as sketched in Figure 2.1(f). This results in a core–ionized state, and the core hole is subsequently filled through mechanisms shown in Figure 2.1(g) and Figure 2.1(h). The former is referred to as the normal X-ray emission (XE), and the latter— the normal Auger-electron emission. Each of the above-mentioned absorption and emission pathways are exploited in this thesis.

2.1.1 X-ray Absorption Spectroscopy

When the photon energy is scanned across a given resonance, this first-order optical absorption process results in an X-ray absorption (XA) spectrum. A typical XA spectrum is characterized by sharp peaks, the absorption bands. These absorption bands mark the transition of electrons from core level to one of the unoccupied valence levels. Probing these unoccupied valence levels is of particular focus because these valence electronic configurations fundamentally characterize properties of any material. Before proceeding further, some fundamental aspects of XA spectroscopy need to be discussed.

An XA spectrum can be obtained using various methods. One basic and most accurate method is the transmission mode method, in which an X-ray beam with an intensity I_0 is allowed to pass through a thin sample, of thickness d. The intensity of the transmitted X-rays is given by the Beer-Lambert law for linear absorption,

$$\frac{I}{I_0} = e^{-\mu(E)d}, \tag{2.1}$$

where the energy-dependent parameter $\mu(E)$ is the absorption coefficient, an inherent property of the material. Varying the incident energy results in different absorbance/absorption

coefficients. A plot of scanned energy versus absorbance results in XA spectra with characteristic sharp peaks mapping the energetic difference of core and valence levels. Broadly, an XA spectrum can be divided into three parts known as pre-edge, main edge and post-edge region. The pre-edge region arises due to transitions to the bound unoccupied density of states, whereas the main edge region marks the electron promotion into continuum states. The pre-edge and main edge regions are commonly called near edge X-ray absorption fine structure (NEXAFS). Figure 2.2(a) depicts a typical K-edge XA spectrum (schematic), obtained by scanning the photon energy for a large energy range, sometimes above 1000 eV. The NEXAFS is extremely sensitive to the local electronic structure of the excited atom, revealing information about the *local electronic* environment of the molecule [33], including hybridization, oxidation state, spin-state and geometry with respect to the target atom [41]. The post-edge part of an XA spectrum can be obtained by scanning photon energies well above the ionization threshold. This part commonly termed as extended X-ray absorption fine structure (EXAFS), is characterized by oscillations formed by constructive interferences of ejected photoelectrons, which are dominantly scattered from the neighboring atoms [42]. The information about *local geometry* around the target atom can be elucidated from the oscillations of EXAFS spectrum [33]. The EXAFS spectroscopy plays a crucial role in structure determination of biologically relevant materials such as metalloproteins [43]. This thesis restricts itself to the NEXAFS region, concentrating on the local electronic structure of the target atoms using soft X-rays. Soft X-rays up to 1000 eV can ionize $2p$ core levels of the first-row transition metals (Co and Cr) and $1s$ core levels of important atoms like C, N and O.

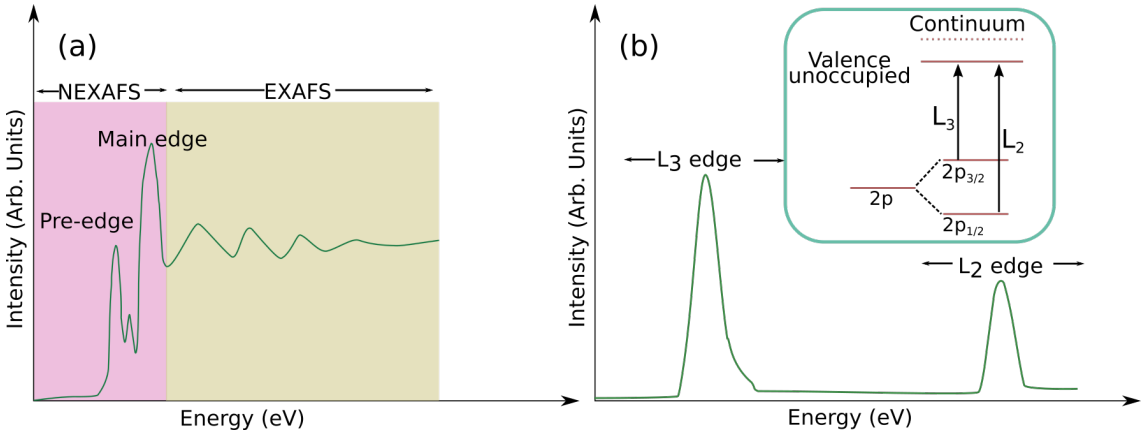

Figure 2.2: (a) Schematic diagram showing NEXAFS and EXAFS regions in a typical K-edge XA spectrum. The transitions in the NEXAFS region can be visualized as shown in Figure 2.1(b). In EXAFS the core electrons are excited well above the absorption threshold (normally above 1000 eV). (b) Typical L-edge XA spectrum of a TM system with L_3 and L_2 splitting.

The intensity of each absorption peak depends on the transition probability between the core level and the unoccupied valence levels involved. The transition probability can

be expressed by *Fermi's golden rule* [44]:

$$T_{fg} = \frac{2\pi}{\hbar}\left|\langle\psi_f|\, T\, |\psi_g\rangle\right|^2 \delta(E_f - E_g - \hbar\Omega) \tag{2.2}$$

Here ψ_g represents the electronic ground state with an energy E_g, and the final state is represented by ψ_f with an energy E_f. T represents the transition operator, acting under the incident photon energy $\hbar\Omega$. The Dirac δ function ensures the conservation of energy [45]. These transitions are restricted by the selection rules $\Delta l{=}\pm1$ and $\Delta s{=}0$, where l and s are the angular momentum and spin quantum numbers [32]. The NEXAFS spectrum of first-row transition metals consists of transitions of electrons from a $2s^2 2p^6$ state into an unoccupied $3d$ valence orbital. Here, the transition $2p^6 \rightarrow 3d$ is favored, more intense, owing to the dipole selection rule $\Delta l{=}\pm1$. The $2s^2 \rightarrow 3d$ transition denoted by L_1 is dipole forbidden. In contrast to the K-edge XA spectrum shown in Figure 2.2(a), the L-edge XA spectrum consists of two distinct edges, namely L_3 and L_2, shown in Figure 2.2(b). These two edges arise due to the spin-orbit coupling of the core excited $2p^5$ level; see Figure 2.2(b) inset. The $2p$ level splits accordingly to $j = l + s = \frac{3}{2}$ and $j = l - s = \frac{1}{2}$ with an intensity ratio of 2:1, where j is the total angular momentum [46]. The transitions originating from $2p_{j_{\frac{3}{2}}}$ and $2p_{j_{\frac{1}{2}}}$ are manifested in the L-edge XA spectrum as the L_3 and L_2 edges. The energetic separation between L_3 and L_2 varies for different elements. For example, they are separated by ≈5 eV for Ti, and ≈20 eV for Cu L-edges [47].

Although the ideal way of measuring an XA spectrum is using the transmission mode, this method requires extremely thin samples (in the range of ≈100 nm) for the transmission of X-rays, and challenges its application to the measurements of liquid samples. One way to overcome this challenge is to use the so-called yield methods such as electron yield (EY) or fluorescence yield (FY). Both methods rely on secondary relaxation channels after a resonant X-ray absorption. This is illustrated in Figure 2.1(c), (d) and (e). Here, the important assumption is that the absorption cross-section is directly proportional to the electrons and photons generated in the second-order relaxation processes, in which the created core hole is being filled by some higher lying valence electrons. In the electron emission case these are the auto-ionization processes. One can collect all the electrons originating from the sample upon X-ray irradiation, and this is called the total electron yield (TEY) method. The use of an energy analyzer allows for selection of emitted electrons within a certain kinetic energy window; this is called the partial electron yield (PEY) method. One then measures the signal from a given Auger/autoionization channel. On the other hand, one can collect the photons emitted after the core hole is refilled; this is called the fluorescence yield method or X-ray emission (XE). One can use a photo-diode, silicon drift detector or a grating spectrometer for detection. When using a photodiode, all the photons can be collected but X-ray energies are not resolved; this method is termed as the total fluorescence yield (TFY) technique. The use of a spectrometer allows for the dispersive detection of photons with different energies, and this is called the partial

fluorescence yield (PFY) method. Note that the fluorescence channel is much weaker in the soft X-ray region (<1000 eV of binding energy) [48, 49]; see the quantum yields for fluorescence and Auger emission in Figure 1.1. One of the critical limitations of the FY method are self-absorption effects [50, 51]. It is the energy-dependent reduction of intensities in an FY spectrum, due to the re-absorption of the emitted photons inside the sample itself. This phenomenon occurs mostly in the case of highly concentrated samples [52].

2.1.2 Resonant X-ray Emission Spectroscopy

Resonant X-ray emission spectroscopy or resonant inelastic X-ray scattering spectroscopy (RIXS) is a second-order optical process [44, 53, 54], i.e., a core hole is created by resonant photon absorption and followed by the emission of a photon upon filling the core hole by a valence or another higher-lying electron; this is illustrated in Figure 2.1(b) and (c). To facilitate the discussion, I introduce a simplified schematic representation of the RIXS process in Figure 2.3, adapted from [55].

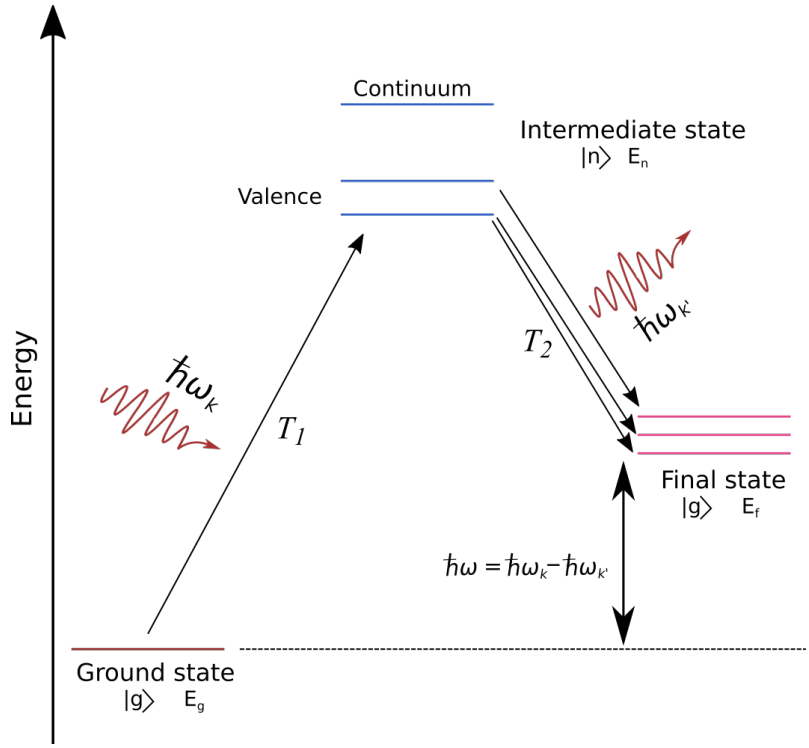

Figure 2.3: Schematic representation of the RIXS process. The system reaches the intermediate state by the transition operator T_1 with the creation of a core hole. The intermediate state decays to the final state by the transition operator T_2. The final state may not necessarily be the electronic ground state.

When the incident photon energy ($\hbar\omega_k$) is tuned to the absorption edge of a ground-state system $|g\rangle$ with energy E_g, the electrons from the core level is scattered to a valence unoccupied orbital, creating a core hole; the intermediate state is represented by $|n\rangle$ with

energy E_n. The dipole operator for this photon absorption process is represented by T_1. The intermediate state decays to one of the final states represented by $|f\rangle$ with energy E_f by emitting a photon of energy ($\hbar\omega_{k'}$).

Mathematically, the RIXS scattering cross section is described by the Kramers-Heisenberg equation [56, 57],

$$\frac{d^2\sigma}{d\omega d\Omega} \propto \sum_f \left| \sum_n \frac{\langle f| T_2 |n\rangle \langle n| T_1 |g\rangle}{E_g + \hbar\omega_k - E_n + i\Gamma_n} \right|^2 \delta(E_g + \hbar\omega - E_f), \tag{2.3}$$

Here, Γ represents the spectral broadening due to the core-hole life-time, which is independent of the intermediate state energy. The transferred energy is represented by $\hbar\omega = \hbar\omega_k - \hbar\omega_{k'}$. The selection rule for RIXS, within the dipole approximation can be written as [58]

$$\langle n'l'm'| T_i |nlm\rangle \neq 0 \quad \Delta l = \pm 1 \quad \text{and} \quad \Delta m = 0, \pm 1, \tag{2.4}$$

where T_i represents a simplified transition dipole operator, $|nlm\rangle$ and $|n'l'm'\rangle$ represent initial and final states, with n-principal, l-angular momentum and m-magnetic quantum numbers.

There is a finite probability that the excited electron itself can refill the core hole, i.e., the final state coincides with the initial state in Figure 2.3; this is called the elastic emission. In contrast, when energy transfer ($\hbar\omega$) occurs, the system undergoes elementary excitations. These elementary excitations manifest as energy-loss (Raman) features in a RIXS spectrum. Typical elementary excitations can range from a few eV to meV; examples are plasmons, charge-transfer excitations, crystal-field excitations, magnetic excitations, and phonons [59, 60]. Among them, charge transfer (CT) excitations and crystal field excitations are studied in this thesis. For TM complexes, charge transfer excitations originate when the electrons from the metal site are excited into the ligand site or vice versa. The crystal field excitations, or commonly known as d-d excitations, arise due to the electronic transition between d orbitals ($3d$ levels in the case of first-row transition metals). The conventional UV-Vis spectroscopy can also access information about d-d excitations, but with the RIXS technique, information output is much higher owing to its element selectivity and relaxed selection rules [61].

Another class of loss features that is part of a RIXS spectrum, and is independent of the incident photon energy, is called the fluorescence or the normal X-ray emission; see Figure 2.1(g). The fluorescence originates when the photon energy is tuned well above the absorption edge thereby creating a core-ionized atom, as shown in Figure 2.1(f). An electron subsequently fills the core hole from the occupied orbitals, and energy is released by emission of photons. An alternative non-radiative channel is also highly probable as shown in Figure 2.1(h); the following Section 2.1.3 describes this in detail.

Sweeping the photon energy from just below the absorption edge to well above the

resonance, one obtains an experimental RIXS spectrum. The obtained individual RIXS spectra can be presented as a map with the incident photon energy along the y-axis and the emitted photon energy along the x-axis, where intensities are given by colors; or as a line spectrum either obtained for constant incident energy, i.e., a horizontal cut from the RIXS map. The map or spectrum is usually a convolution of elastic, energy-loss and fluorescence features. The elastic and energy loss features appear as diagonal stripes, whereas the fluorescence features remain as vertical stripes along constant emission energy. Another way of plotting the RIXS map or line spectrum is by plotting the incident energy versus energy-loss scale. The energy-loss scale is obtained by subtracting the incident photon energy from the emitted photon energy. In the energy-loss representation, the loss (Raman) features appear as vertical lines, and the fluorescence features as diagonal traces.

2.1.3 Non-Resonant and Resonant Photoelectron Spectroscopy

The underlying principle of photoelectron spectroscopy is the photoelectric effect; the method measures the kinetic energy of the emitted electrons from the sample after X-ray impingement [62]. In the case of solids, the photoemission process is described by a three step model [62]: the excitation of the electron, propagation of electrons to the surface, and its liberation through the surface into vacuum. Aqueous systems present a disordered and isotropic bulk nature compared to solid systems [63]. The photoemission leaves the system in an ionized state. It can occur from the valence orbitals or from the core orbitals, depending on the energy of the incident photon. These two emission channels are illustrated in Figure 2.1(a) and (f).

The energy of the incident photons ($\hbar\omega$) determines the kinetic energy (KE) of the ejected electron as

$$\mathrm{KE} = \hbar\omega - \mathrm{BE}, \qquad \hbar\omega > \mathrm{BE}, \tag{2.5}$$

where BE is the binding energy of the electrons with respect to vacuum. The binding energy of the electrons is an inherent characteristic of the atom under study. Thus, the measurement of KE of electrons connects to an important property, the ionization energy, understood through Koopmans' theorem. Koopmans' theorem states that the binding energy or the ionization potential of an electron is equal to the negative of its orbital energy [49]. If the electronic-ground state of a system is represented by $|\psi_g\rangle\,(n)$, the Schrödinger equation is

$$H(n)\psi_g(n) = E_g(n)\psi_g(n), \tag{2.6}$$

where $H(n)$ is the n- electron Hamiltonian and $E_g(n)$ the ground-state energy. After photoemission, the $(n-1)$-electron Schrödinger equation reads as

$$H(n-1)\psi_i(n-1) = E_i(n-1)\psi_i(n-1), \tag{2.7}$$

where $H(n-1)$ is the $(n-1)$ electron Hamiltonian and $E_i(n-1)$ is the energy in the

ionized state. The transition probability between the ground and ionized state is governed by Fermi's Golden Rule, see equation 2.2. By the law of conservation of energy and Koopmans' theorem, the ionization potential ($IP(i)$) is given by

$$IP(i) = E_i(n-1) - E_g = -E_b, \tag{2.8}$$

where E_b is the orbital energy [49, 64]. The determination of the orbital binding energy using Koopmans' theorem is approximate and not always accurate due to the lack of consideration of the electron correlation, especially in the valence orbitals [65]. The change of Hamiltonian from $H(n)$ to $H(n-1)$ is treated as instantaneous, also the ejection of a 'one electron' event is so rapid, this is commonly referred to as the sudden approximation treatment. Validity of the sudden approximation is rationalized as long as the ejected electron is excited well above the ionization potential [49, 66, 67].

For the direct photoemission from a core orbital, the core hole can be filled by an electron from the valence orbitals by emitting a photon or an electron (called normal Auger electron). The normal Auger-electron emission leaves the system in a doubly ionized state. The sequence of events are shown in Figure 2.1(f) and (h). The kinetic energy of the Auger electrons will be independent of the incident photon energy.

At resonance, the incoming X-rays promote an electron into one of the unoccupied levels, such that the incoming photon energy $\hbar\omega = E_i - E_g$, where E_i is now not the ionized state energy but the excited state energy with neutral charge. The situation is identical to the resonant X-ray absorption described above, followed by relaxation via non-radiative channels. The expected sequence of events for a non-radiative emission following a resonant photon absorption is illustrated in Figure 2.1(b), (d) and (e). The detection of Auger electrons under a resonance condition is called resonant photoelectron spectroscopy. Here, the resonant Auger-electron emission can occur in two ways as shown in Figure 2.1(d) and (e), corresponding to spectator Auger emission and participator Auger emission. Compared to the normal Auger emission, the resonant Auger emission leaves the system in a singly ionized state. The resonant Auger-emission channel can be exploited as it increases the photoemission signal intensity, especially in the valence region. This significant increase in the signal intensity arises from the coherent superposition of Auger electrons with the direct photoelectrons from valence ionization. At resonance, both electrons are indistinguishable, having the same energy.

The emitted photoelectrons are not isotropic in distribution. An efficient detection of the photoelectrons is possible when the electron analyzer is oriented at a certain angle with respect to the polarization of the incident X-rays. The angular distribution of photoelectrons for randomly oriented molecules interacting with linearly polarized light can be expressed by the differential scattering cross section $\frac{d\sigma}{d\Omega}$ as,

$$\frac{d\sigma}{d\Omega} = \frac{\sigma}{4\pi}[1 + \frac{\beta}{2}(3\cos^2\theta - 1)], \tag{2.9}$$

where σ is the total ionization cross section, Ω is the solid angle of detection, β is the anisotrpy (asymmetry) parameter, and θ is the angle between direction of the ejected electrons and the polarization vector [68, 69]. The value of anisotropy parameter (β) varies between -1 and 2. The electron measurements in this thesis were carried out at an angle $\theta = 54.7°$ for eliminating the anisotropy parameter. This angle is commonly referred as 'magic angle'.

2.2 BESSY II Storage Ring, Beamlines and Experimental Stations

BESSY II (Berliner Elektronenspeicherring-Gesellschaft für Synchrotronstrahlung) is a third-generation synchrotron light facility operated at an energy of 1.7 GeV, a core facility of Helmholtz-Zentrum Berlin, Germany [70]. It provides high brilliance VUV to hard X-ray radiation for fundamental research, energy material research and industrial applications [71–73]. At its core, BESSY II has a 90 kV triode gun in *Pierce-type geometry* (EIMAC Y-845 cathode) with a 0.5 cm^2 emissive area. Electrons produced are fed into a 50 MeV linac with repetition rate varying from 1 to 10 Hz, which accelerates the electrons to 99.99% of the speed of light. These electrons are further increased in energy to 1.9 GeV inside a booster synchrotron, which has a circumference of 96 m. These high-energy electrons are injected into the storage ring, which has a circumference of 240 m. More than 50 beamlines are attached to the storage ring, which mainly operates in the top-up mode [74] with a near-constant ring current of 250 mA.

The present work has been carried out at two plane-grating monochromator (PGM) beamlines, U41-PGM and U49-2 PGM-1 [75]. The core-level spectroscopic study of TM complexes presented in this work requires photon energies ranging from 200 to 1000 eV with high photon flux. The tunability of photon energies combined with a high photon flux and a microfocus beam size were crucial for resonant X-ray studies from the solution phase.

2.2.1 The U41-PGM and U49-2 PGM-1 Beamlines

The U41-PGM beamline (dismantled in 2015) was a micro-focus high brilliance beamline with an open port for flexible experimental station capability. The undulator had a period length of 41 mm and 80 periods. The beamline was designed to operate in the energy range between 170-2000 eV. With a 600 lines/mm grating the beamline delivered a photon flux between 10^{12} and 10^{13} photons over the 170-1500 eV energy range. The layout of the beamline is shown in Figure 2.4(a). The first optical element is a toroidal mirror (M_1) which collimates the photons from the undulator. Photons are monochromatized using the combination of a plane grating (G) and plane mirror (M_2). The grating is placed close to the source for preserving the highly brilliant photons. This monochromatic collimated

beam is then focussed onto the exit slit using a cylindrical mirror (M_3). Behind the exit slit, the beam is refocused using another toroidal mirror (M_4). The best focus size of 36 μm x 12 μm (horizontal x vertical) could be achieved with an exit slit of 20 μm and C_{ff} 0.1 [76].

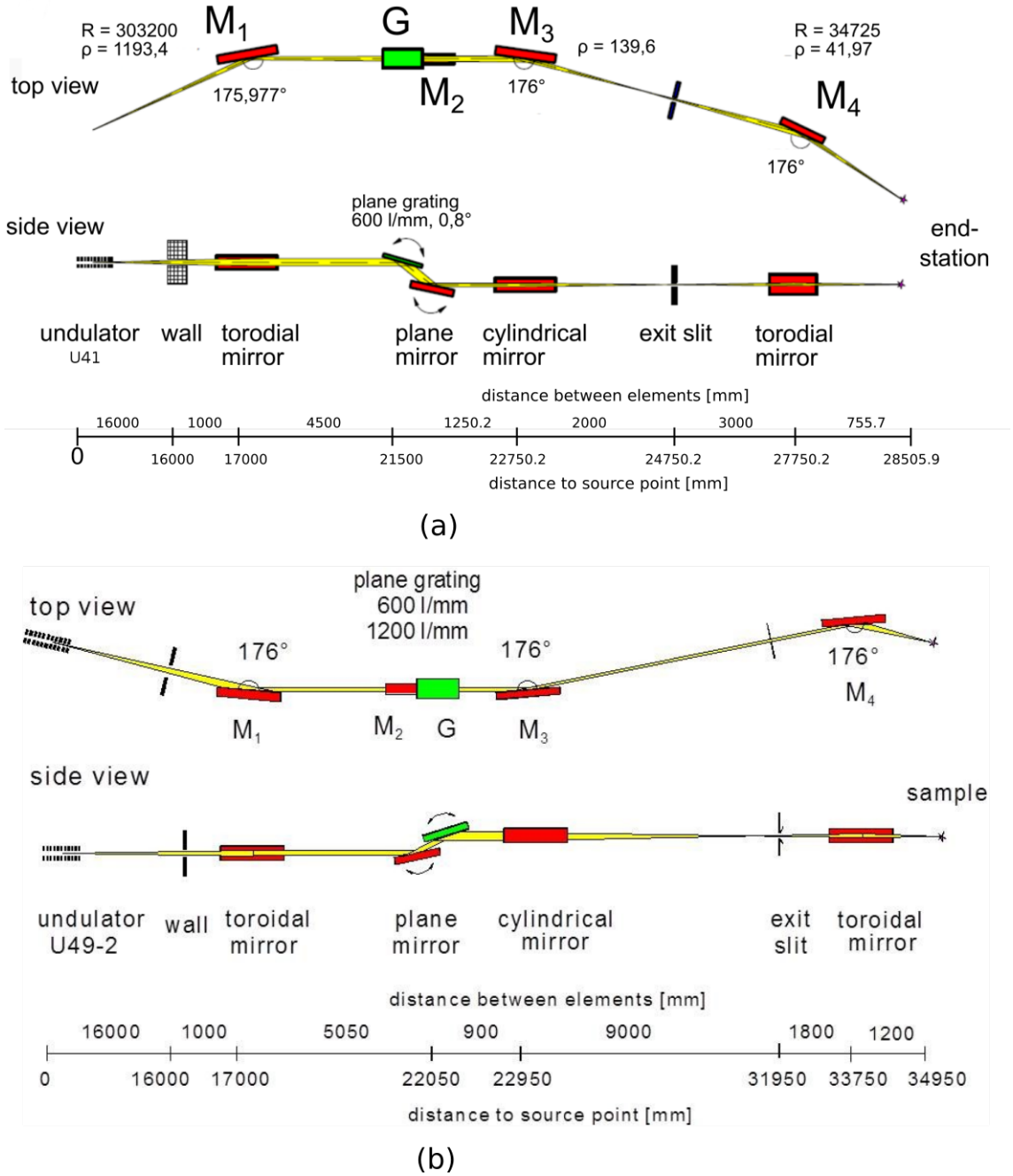

Figure 2.4: Top and side view of (a) U41-PGM and (b) U49-2 PGM-1 beamline optics. [77, 78]

The fixfocus constant(C_{ff}), defined as the ratio of the cosine of the diffraction angle and the cosine of the incidence angle at the grating, can be varied in a wide range but

with values <1. This allowed the beamline operation in either high flux or high energy resolution, according to the requirements. The high photon flux and microfocus spot are crucial for liquid measurements, especially in dilute aqueous solution systems studied in this thesis using liquid microjet and flow-cell techniques. The U41-PGM has been upgraded and commissioned in 2016, and the fixed experimental station PEAXIS is now connected to it.

The layout of the U49-2 PGM-1 beamline is shown in Figure 2.4(b). This beamline is primarily designed for high energy resolution and high photon flux. The undulator U49-2 consists of 84 periods with a period length of 49 mm. It provides photon energies in the range of 70 to 1500 eV with linear polarization [78]. Unlike the U41-PGM the plane mirror (M_2) is located in front of the grating in the monochromator section. To achieve a better resolution compared to the U41-PGM, the U49-2 PGM-1 is equipped with two plane gratings with 600 lines/mm and 1200 lines/mm. The beamline provides an energy resolution of $\frac{E}{\Delta E} = 25,000$ (between 80–500 eV) and $\frac{E}{\Delta E} = 15,000$ (500– 1500 eV) with the standard grating. The focal size of the beam is as small as 80 μm x 22 μm. The experimental stations attached to these beamlines for RPE and RIXS studies are the LiquidPES and the LiXEdrom setups, described below.

2.2.2 LiXEdrom – Experimental Setup for RIXS Spectroscopy

The *LiXEdrom* is a mobile experimental station for conducting high-resolution RIXS measurements from solution and colloidal phases [79, 80]. A schematic diagram is shown in Figure 2.5(a) and a simplified top view is shown in Figure 2.5(b). This experimental station has three sections, the main chamber, where X-rays interact with the sample, a differential pumping section for coupling the main chamber to the beamline, and a spectrometer. The main chamber pressure is in the range of 10^{-4} – 10^{-5} mbar for liquid-jet and 10^{-7} mbar for flow-cell measurements. The spectrometer and differential coupling sections are separated by pinholes from the main chamber, this serves to maintain a pressure of $\sim 10^{-9}$ mbar in both the sections with differential pumping and cooling. The main chamber is designed to handle liquid-jet and flow-cell techniques, a micrometer precision XYZ manipulator is used for aligning the sample with the beamline and the spectrometer. The RIXS spectrometer, based on Rowland circle geometry, consists of a grating chamber and an X-ray photon detector. Two variable-line-spacing (VLS) spherical gratings are currently in use, covering the photon energy ranges 200 – 500 eV and 400 – 1200 eV with line densities 1200 1/mm and 2400 1/mm respectively. The X-ray photon detector is a combination of a micro-channel plate (MCP), a phosphorous screen and a charge coupled device (CCD) camera. The detector section is connected to the grating chamber via a metal bellow and mounted on a motorized manipulator, which enables x, y translation and rotational motion of the detector.

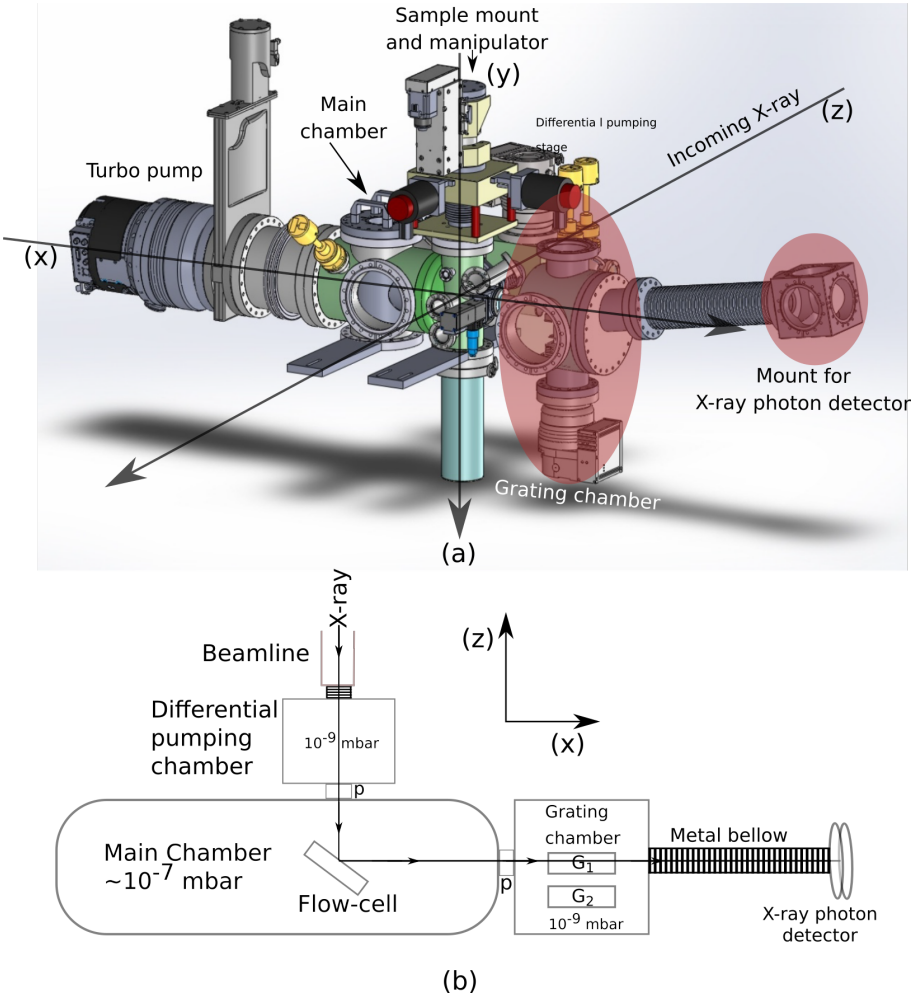

Figure 2.5: (a) A schematic view of the LiXEdrom experimental station. The spectrometer section includes a grating chamber and an X-ray photon detector. (b) Simplified top view of the setup, P is the pinhole separating the main chamber from differential pumping and grating chamber. 3D schematic picture is by *Ronny Golnak* [79].

2.2.3 LiquidPES – Experimental Setup for RPE Spectroscopy

Photoelectron spectroscopy from liquid phase is well adopted by the *LiquidPES* experimental station at BESSY II. A sketch of the setup is shown in Figure 2.6. The setup consists of a main (jet) chamber, a differential pumping stage and a hemispherical electron analyzer. Interaction of X-rays with liquid jet takes place in the main chamber. Pressure values in this chamber can be maintained approximately in $10^{-4}/10^{-5}$ mbar during operations, which is enabled by a high-performance turbo molecular pump and liquid nitrogen cooling trap (LN_2). The differential pumping stage separates the main chamber from the beamline and ensures a pressure of $\approx 10^{-9}$ mbar in the last refocusing chamber of the beamline. A liquid jet of 24 μm diameter was introduced into the main chamber by a high pressure liquid chromatography (HPLC) pump through a loop system. Jet velocity was typically 40 ms^{-1}, and the sample reservoir temperature was 12°C. After interaction

with the X-rays the liquid jet shoots further towards another cold trap and gets collected as icicles. The polarization axis of the incoming X-rays is along with the jet flow. In a

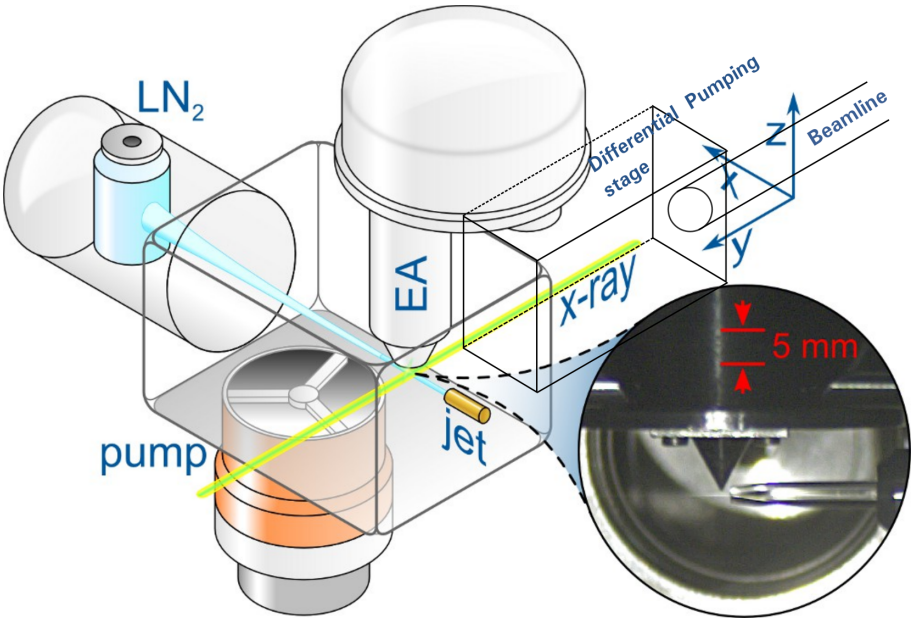

Figure 2.6: A schematic view of the LiquidPES experimental station. The inset photograph shows the liquid jet – X-ray interaction region; the conical aperture is the entrance (500 μm) to the hemispherical electron analyzer [81].

default geometry, shown in Figure 2.6, the hemispherical electron energy analyzer (EA) (Specs Leybold EA 10 multichannel detector) is arranged such that the detection axis is perpendicular to the polarization axis of the incoming X-rays. However, the photoelectron spectroscopy measurements presented in this thesis were obtained at the magic-angle geometry, i.e., an angle of 54.7° was set between the synchrotron light polarization axis and the EA so that the electron intensity is independent of detection angle. Pressure inside the EA was 10^{-7} mbar during measurements. In order to eliminate the earth's magnetic field on the photoelectrons, a Helmholtz cage is used. Extensive details about the *LiquidPES* setup can be found in references [82, 83].

2.3 Sample Handling in Vacuum

Due to the strong absorption of soft X-rays with the surrounding atmosphere, vacuum condition is crucial for L-edge and K-edge studies on TM complexes as well as on elements like C, N and O [84]. The introduction of samples into the vacuum chamber is achieved by two methods, the liquid-jet and by the flow-cell technique, as illustrated in Figure 2.7. In the liquid-jet technique the solution is pushed directly into the vacuum chamber, whereas in the case of a flow-cell a thin membrane acts as an interface separating the liquid from vacuum. The liquid jet technique allows the detection of both electrons and photons emitted upon soft X-ray sample interaction. In contrast, the flow-cell technique is mostly applicable for

photon detection. However, extremely thin graphene based membranes coupled with new generation electron energy analyzers are used for detecting photoelectrons from colloidal nanoparticles and aqueous salt solutions [85, 86]. Another promising method under development is the holey flow-cell [87] based technique, where a stable liquid−vacuum interface is formed with the use of a membrane (Si_3N_4 or SiC) with micrometer sized holes. A continuous liquid flow is maintained behind the holey membranes. The liquid-jet and the flow-cell methods allow for the continuous renewal of sample. For the photoemission studies presented in this thesis, i.e., aqueous $[Co(CN)_6]^{3-}$, spectra were obtained by employing the liquid-jet technique using the LiquidPES experimental station.

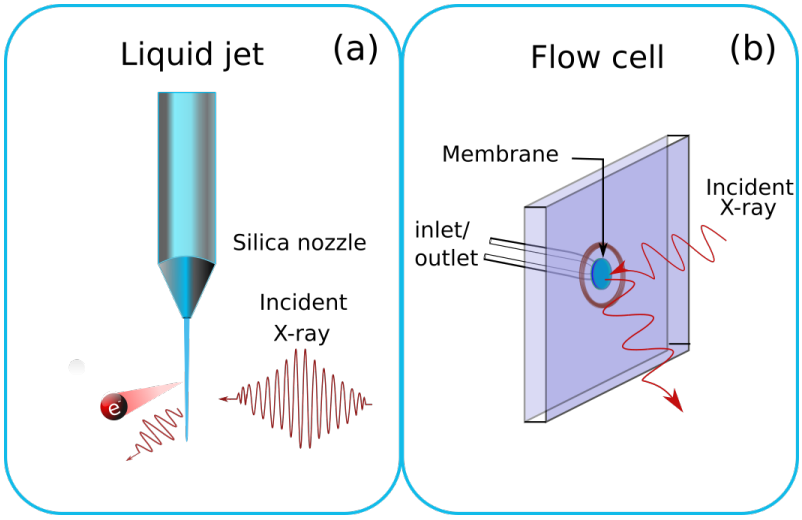

Figure 2.7: A schematic picture of the liquid jet (a), the soft X-ray–solution interaction takes place in vacuum. (b) Flow-cell, a membrane (silicon nitride or silicon carbide of thickness 100-150 nm) separates the liquid from vacuum.

2.3.1 The Liquid-Microjet

The liquid jet technique was pioneered by M. Faubel back in 1988 [88]. It was further developed over the decades and now became the quintessential method for accessing the electronic structure of matter in solution and colloidal phases [63, 89]. In order to produce a narrow cylindrical stream of liquid (jet), the solution under study is forced through a fused-silica nozzle. The size of the liquid jet depends on the nozzle orifice, which varies between 10–30 μm. A jet diameter of 15 μm and velocity of approximately 100 m/s with constant flow rate is desired while this is achieved by applying roughly a pressure of 5–20 bar using High Pressure Liquid Chromatography (HPLC, Techlab Model Economy 2/ED) pumps connected to a loop system. A narrow jet size ensures the detection of undisturbed photoelectrons from the solution by reducing the amount of vapor density around the liquid jet. The jet injected into vacuum has a laminar flow pattern over only several millimeters and then decomposes into droplets. Eventually the jet freezes approximately 50 cm away from the laminar region and collected as icicles in a liquid nitrogen cooling trap. Vacuum

of $\approx 10^{-4}$-10^{-5} mbar can be maintained during the operation of a liquid jet, achieved by the combination of cooling traps and turbomolecular pumps.

The essential components of a microjet injection system are shown in Figure 2.8. A stable flow with a laminar surface is necessary for the uninterrupted detection of photoelectrons for obtaining a fluctuation-free spectrum. This is achieved using an HPLC pump. Two reservoirs are part of the loop system as shown, which ensures back-to-back measurements of a sample or a reference sample without much time delay between measurements. The connected loop is filled with solution from the reservoir with the help of a syringe. Solution to the jet rod can be either from the reservoirs or from the filled loop achieved using the switch.

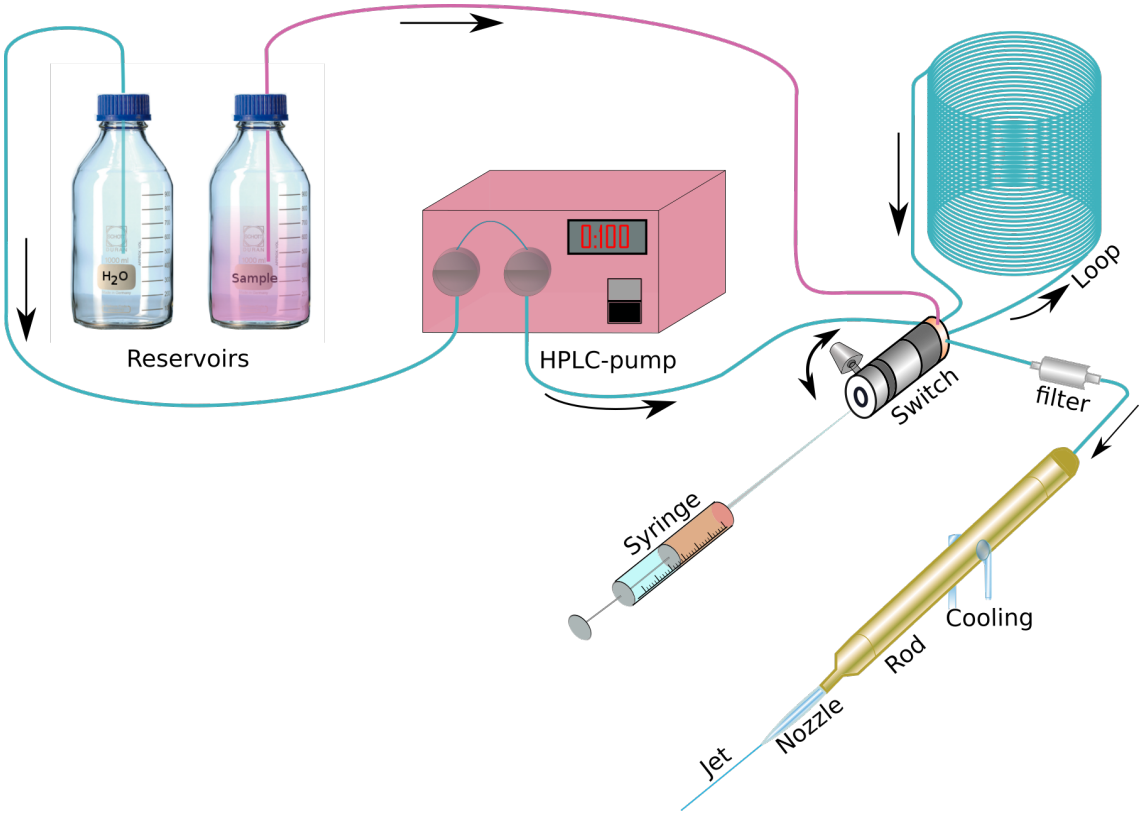

Figure 2.8: The loop system employed for injecting the liquid jet.

The tubes used for the loop and inter- connections are made from chemically inert materials like fluorinated ethylene propylene (FEP) or polyether ether ketone (PEEK) which is important when handling highly reactive chemical solutions like the ones used in this thesis presented. Before flowing to the jet rod the solution is filtered using an inline filter (pore size of 10 μm), which prevents clogging due to precipitated particles. The solution in the jet rod is cooled to 4–6°C to keep the vapor pressure low. It is then pushed out through the nozzle resulting in the jet. The size of the jet can be varied with an appropriate selection of the nozzle. The jet rod is mounted on an xyz manipulator for accurate positioning of the jet.

For the photoemission study of aqueous $[Co(CN)_6]^{3-}$, the liquid jet (24 µm diameter) was injected into the vacuum chamber from a fused-silica nozzle. The jet velocity and the sample reservoir temperature were approximately 40 ms^{-1} and 12°C, respectively. The actual jet temperature in the interaction region is lower than 12°C but an exact value cannot be provided; except the lower limit of 3°C, as estimated from evaporative cooling modeling [88, 90].

2.3.2 The Flow-Cell

All the RIXS studies presented in this thesis were measured using the flow-cell technique in the LiXEdrom experimental station [91]. In this technique the liquid sample is separated from the vacuum by a thin membrane. As shown in Figure 2.7(b), the flow-cell is mounted 45° to the incident X-ray direction. The inlet and outlet tubings are connected to a pump (peristaltic or syringe pump) and the sample reservoir. The flow rate can be controlled by the pump setting, typically operated between 0.5 ml/min to 3 ml/min. The membranes were made of silicon nitride (Si_3N_4) or silicon carbide (SiC). The dimensions of the Si_3N_4 and SiC membranes are 1.0 x 0.5 mm, with a thickness of 100 nm and 1.0 x 1.0 mm, with a thickness 150 nm respectively. They are grown on a silicon wafer with dimensions 10 x 10 mm^2 and thickness in the range 350–625 μm. Selection of a membrane depends on the sample system; for N K-edge studies presented in this thesis, I employed SiC membranes (*NTT Advanced Technology Corporation, Japan)*, which can withstand a pressure difference of over 1 bar and also exhibit high thermal stability under X-ray irradiation. Vacuum of $\approx 10^{-7}$ mbar can be maintained while measurements. A certain percentage of the incident

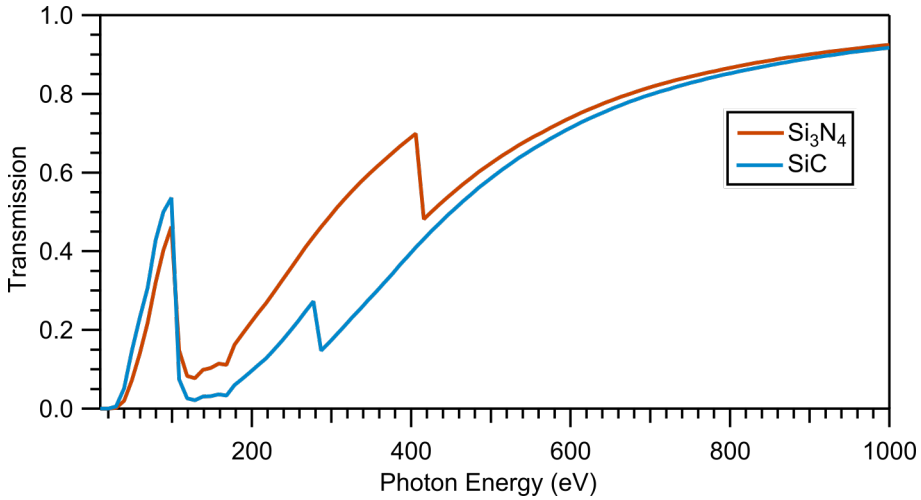

Figure 2.9: Transmittance of Si_3N_4 and SiC membranes with thickness 100 nm and 150 nm. Data obtained from `http://henke.lbl.gov/optical_constants/filter2.html`

and emitted X-rays are lost due to the membrane's transmittance. Figure 2.9 shows the experimental transmittance of Si_3N_4 and SiC membranes. Additionally, the 45° geometry of the flow-cell causes a reduction in X-ray signal intensity. Combining these two factors, a transmittance of approximately 10% for 400 eV photons and 65% for 800 eV photons is

available for detection.

2.4 Computational Details

A thorough understanding of an experimental spectrum will not be possible without the aid of computation. The last two decades witnessed the emergence of various theoretical approaches for generating the sophisticated experimental spectra. Among them, the density functional theory (DFT) became applicable to simple molecules and condensed matter phases, particularly accurate in ground state calculations. In this thesis I used DFT and post Hartree-Fock methodologies for the calculation of various L-edge and K-edge spectra.

All the calculations were carried out using ORCA quantum chemistry program package [92], which is particularly efficient in calculating spectroscopic properties of TM complexes. Modules used from the software package are illustrated in Figure 2.10. Every spectral calculation starts from the DFT enabled geometry optimization. The optimized geometry is further fed into various approaches for generating the relevant X-ray spectrum. As shown in Figure 2.10, for generating an L-edge XAS, L-edge RIXS and K-edge RIXS spectra, the efficient method is the DFT/ROCIS [93]. On the other hand for generating a K-edge XA spectra, the best approach is to use the time dependent-DFT (TD-DFT) method [94]. Ground-state single-point DFT calculations were used for interpreting valence PE spectra presented in Chapter 3. Aqueous environment was mimicked using conductor like polarizable continuum model (CPCM) in ORCA Ver.4 [95, 96] and conductor-like screening model (COSMO) in ORCA Ver.3 [97]. Inclusion of relativistic effects improve spectral results in the study of TM complex systems; this is achieved using zeroth order regular approximation (ZORA) [98]. A short description of DFT/ROCIS and (TD-DFT) methodologies are provided below.
The basic procedure for extracting electronic structure information is to solve the time-independent Schrödinger equation 2.10 for obtaining ground state energy [99, 100].

$$\hat{H}\Psi(r_1, r_2, \cdots, r_n) = E\Psi(r_1, r_2, \cdots, r_n) \tag{2.10}$$

where E is the total energy and $\hat{\mathrm{H}}$ is the Hamiltonian for the system and $\Psi(\mathrm{r_1},\mathrm{r_2},....,\mathrm{r_n})$ is the N-electron wave function which contains a wealth of information regarding the system. The Hamiltonian $\hat{\mathrm{H}}$ can be expanded (in Hartree atomic units, $e = \hbar = m = 1$) as

$$\hat{H} = -\frac{1}{2}\sum_{i=1}^{N}\nabla_i^2 + \sum_{i=1}^{N} v(r_i) + \frac{1}{2}\sum_{i}\sum_{i\neq j}\frac{1}{\mid r_i - r_j \mid}. \tag{2.11}$$

for an N electron system under a nuclear potential *v(r)*. Here, the first term in the summation is the kinetic energy of electrons, second term is the potential energy due to the nuclei and the third term arises due to the electron-electron interaction energy. Solution to the Schrödinger equation 2.10 is difficult due to the electron-electron interaction energy

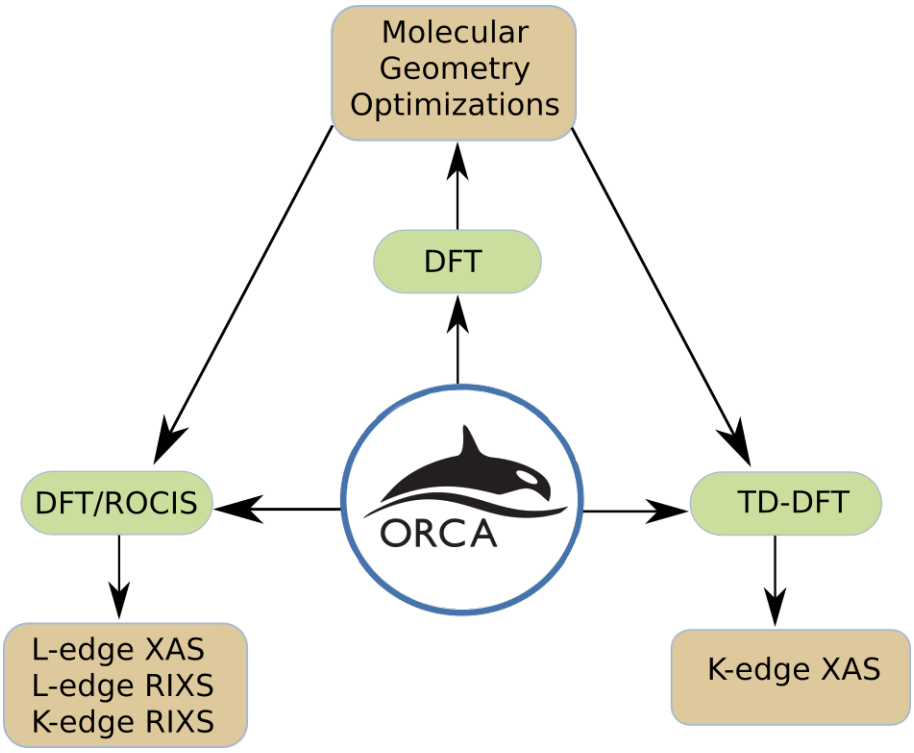

Figure 2.10: Summary of computational methods used for XA spectral and RIXS calculations using ORCA software package. For XE spectral calculations, orbital energy and transition dipole moments resulting from ground state DFT calculations were used.

term. This difficulty is overcome by applying certain approximation methods. One such approach is the wave function or Hartree-Fock method. Here, each electron is described by a wavefunction, also called spin-orbitals (ϕ) formulated by including the spin-up and spin-down nature of the electrons (*Pauli exclusion principle*). For an N electron system all the spin-orbitals can be expressed as a slater determinant equation 2.12. Hartree-Fock equations and energy are obtained by employing the variational principle, from the assumption that a trivial wavefunction is equivalent to a slater determinant.

$$\Phi_{SD} = \frac{1}{\sqrt{N!}} \begin{vmatrix} \phi_1(1) & \phi_2(1) & \cdots & \phi_N(1) \\ \phi_1(2) & \phi_2(2) & \cdots & \phi_N(2) \\ \vdots & \vdots & \ddots & \vdots \\ \phi_1(N) & \phi_2(N) & \cdots & \phi_N(N) \end{vmatrix}; \langle \phi_i | \phi_j \rangle = \delta_{ij} \tag{2.12}$$

This approach excludes the electron correlation and is applicable to only those molecules with small number of electrons (≈10) due to the so-called "exponential wall" problem [101]. These difficulties are addressed by post-Hartree-Fock methods [102] such as *configuration interaction* (CI), *multi-reference configuration interaction* (MRCI), *Many-Body Perturbation Theory* (MBPT) and *coupled cluster* (CC) [103], as these methods include electron correlation to various levels of accuracy. Detailed descriptions of these methods are beyond the scope of this thesis. Nevertheless, the CI is a simple method based on variational

principle which incorporates electron correlation. Here, the trial wavefunction is expressed as a linear combination of determinants with coefficients determined from Ritz variational approach [104]. The expanded wavefunction takes the form

$$\Psi_{CI} = a_0\Phi_{HF} + \sum_S a_S\Phi_S + \sum_D a_D\Phi_D + \sum_T a_T\Phi_T + \cdots = \sum_{i=0} a_i\Phi_i. \tag{2.13}$$

There is a computational challenge in calculating the complete CI wavefunction in equation 2.13. This challenge can be reduced by truncating equation 2.13 by reducing the number of slater determinants in the CI expansion. Truncation of equation 2.13 to the first summation term is known as *configuration interaction singles* (CIS). For open-shell systems with odd number of electrons, one way to construct CI wavefunction is by restricting two electrons spatially on an orbital, and this configuration leads to what is known as restricted open shell configuration interaction singles (restricted open shell configuration interaction singles). This ROCIS method is utilized for generating the excited state spectra (L-edge XAS, L-edge RIXS and K-edge RIXS) of TM complexes in the present work [105, 106].

One major limitation of truncating equation 2.13 to the first summation terms is that CIS become akin to Hartree-Fock method, hence the electron correlation (or dynamic correlation energy) is minimal. This in turn affects the quality of excited-state spectra. The ORCA software package addresses this problem by a hybrid method known as DFT/ROCIS. This method incorporates DFT based orbitals with scaled CIS resulting in a better electron correlation and improved excited-state spectra.

In DFT the ground state energy is obtained from an observable quantity known as electron density [107, 108]. For an N-electron system the electron density can be written as

$$\rho(r) = N_{el} \int \mid \Psi(r_1, r_2, \cdots, r_N) \mid^2 dr_2 \cdots dr_{N_{el}} \tag{2.14}$$

integrated over N−1 electron coordinates. The main advantage of expressing the N electron system in terms of its electron density is reducing the number of variables to three spatial coordinates. This is different from the wavefunction-based method described above, where a 4N variable is necessary (three for the spatial and one for the spin of each electron). DFT method is used for geometry optimization of all the molecules studied in this thesis. This method is also used for extracting information about the metal–ligand orbital mixing ratios using Löwdin [109] population analysis from the ground state calculations. However, the use of DFT for calculating transition energies is not accurate because of its inefficiency to calculate excited states. What is important for generating an excited-state spectrum, such as an XAS is obtaining the relative transition energy positions and relative intensities. For achieving this we use the more appropriate method of time dependant density functional theory (TD-DFT).

TD-DFT is an extension of DFT which gives better results for time-dependent processes

and calculation of excited states [110, 111]. Here, the external potential $v(r_i)$ in the Hamiltonian (Equation 2.11) is treated as time-dependent, and the electrons are under the influence of this potential. All the N K-edge XA spectra presented in this thesis are obtained from TD-DFT method implemented in ORCA. The core hole is localized in the ligand atom (N 1s). All the possible transitions to virtual orbitals (unoccupied valence orbitals) from the localized core (1s) are included in the TD-DFT equation. Then the dipole and quadrupole transition strengths are evaluated between the core and virtual orbitals. Sum of transition strengths are used for generating the final spectrum [112]. Details about basis sets and functionals are included in brief computational sections in Chapter 3.

3. Results and Discussions

3.1 Chemical Bonding in Aqueous Hexacyanocobaltate

3.1.1 Bonding in Transition-Metal Cyanide Complexes

Electronic structure of TM complexes has been an area of active research for nearly a century [36, 114]. In the case of TM complexes bond formation mainly involves the sharing of electron densities between valence $3d$ orbitals of the metal atom and the outer ligand orbitals. In TM–cyanide (CN^-) complexes, two types of covalent bonds are present, the σ- and π-bonds. Such interactions are common in organometallic chemistry involving TM ions with multi-atomic ligands. In σ-bonding (also called σ-donation), the electron density from the valence CN^- orbitals is transferred to the unoccupied metal orbitals. The π-bonding arises due to the transfer of electron density from the occupied metal orbitals to the unoccupied CN^- orbitals, commonly known as the π-backbonding. Section 1.3 provides a detailed background information of various bondings in TM systems. It is a result of the strong π-acceptor nature of the CN^- ligands, relieving the metal of excess negative charge, and leading to the stabilization of the complex. The chemical properties of TM complexes strongly depend on the type and extent of bonding, and hence on electronic structure. Therefore, the fundamental understanding of different types of bonding interactions is important in tailoring and tuning material properties for given applications such as catalytic water splitting [115]. The use of liquid-microjet [63] and flow-cell [24] methods (see Chapter 2, Section 2.3), combined with state-of-the-art synchrotron based X-ray spectroscopic techniques, enables to explore the electronic structure in aqueous environments [116]. This is even crucial in the case of multi-atomic ligands when the metal center is not in direct contact with the solvent.

This section studies the local electronic structure and bonding interactions of the $[Co(CN)_6]^{3-}$ complex in aqueous solutions using X-ray spectroscopic methods detecting both emitted photons and electrons. $[Co(CN)_6]^{3-}$ (aq), with low-spin $3d^6$ electronic ground-state configuration in an octahedral strong ligand field [36], is a particularly interesting case for exploring the strength of π-backbonding and σ-bonding because the t_{2g}

Large parts of the text in this chapter is taken from the published work '*Chemical Bonding in Aqueous Hexacyanocobaltate from Photon- and Electron-Detection Perspectives*' by *Lalithambika* et al. [113]. Edits and cuts have been made to match the flow of the thesis.

and e_g valence levels resulting from the splitting of the $3d$ levels by the ligand field are completely filled and completely empty, respectively. σ bonding in $[Co(CN)_6]^{3-}$ (aq) arises from the donation of electron density from the highest occupied molecular orbital (HOMO), 5σ, of CN^- to the metal $3d$ orbitals. π-bonding results from the filling of the vacant $2\pi^*$ orbitals, i.e., the lowest unoccupied molecular orbitals (LUMO) of the CN^- by metal $3d$ (t_{2g}) electrons [117, 118].

Several studies on the electronic structure of various TM cyanides, in aqueous and ethanol solutions, using UV/Vis spectroscopy [119, 120] have been previously reported. In addition, metal L-edge and nitrogen K-edge TEY-XA measurements have been performed from powder samples of TM–cyanide $[X(CN)_6]^{3-}$ complexes, where, X = Cr, Mn, Fe, and Co [38]. Other studies have explored the electronic structure of ferro- and ferricyanide complexes applying L-edge TEY-XA [121] and K-edge RIXS [122] spectroscopy, respectively, also using powders. Experimentally, this section describes the Co $L_{2,3}$ ($2p$) and N K ($1s$) edge PFY and PEY-XA spectra, and in addition RIXS, valence, and core-level PE spectra measurements. For an interpretation of the experimental PFY- and PEY-XA spectra I use DFT/ROCIS for the L-edge and TD-DFT calculations for the K-edge [93].

Regarding the photoelectron (PE) spectroscopy measurements performed here, I also report resonant (RPE spectra) Co L-edge and N K-edge spectra, as well as non-resonant valence photoelectron spectra from $[Co(CN)_6]^{3-}$ aqueous solution. The RPE spectra provide unique insight into mixing of metal and ligand orbitals, and furthermore integration of the signal intensities of RPE spectra measured across a given resonance yields the respective XA spectra. Here, one essentially tracks the intensity of the Auger electrons emitted in a given autoionization channel (valence to core hole), see Figure 2.1, which is to a first approximation proportional to the actual X-ray absorption [123]. An important aspect in the present work is the exploration of signal enhancements at resonant excitation (due to interfering Auger electrons and direct photoelectrons with the same kinetic energies) which identifies metal and ligand orbital overlap [124]. RIXS measurements are performed at the same edges, Co $2p$ and N $1s$. RIXS and PFY-XA spectroscopy, being element/site specific photon-in photon-out techniques, exploit core-level excitations to probe occupied and unoccupied electronic states of the investigated molecule respectively [49, 59]. Analogous to the RPE spectra, RIXS spectra shed light into metal–ligand orbital hybridization, and integration of the RIXS spectra yields the PFY-XA spectra. Analysis of all mentioned electron- and photon-out channels is crucial for an accurate understanding of the complex electronic-structure interactions of the $[Co(CN)_6]^{3-}$(aq) complex.

3.1.2 Sample Preparation and Experimental Details

Potassium hexa-cyanocobaltate(III) was purchased from Sigma Aldrich (purity > 97 %). A 200 mM aqueous solution, using Milli-Q water, was freshly prepared immediately prior to experiments. The PFY-XA and RIXS and non-resonant XE spectroscopy measurements at the Co $L_{2,3}$-edge and N K-edge were carried out with the LiXEdrom setup, and PEY-XA

spectroscopy and RPE spectroscopy measurements were carried out with the LiquidPES setup [125]. Details about the experimental stations are provided in Sections 2.2.2 and 2.2.3. For the photon-out detection the measurements were performed using a flow-cell, whereas for the electron emission a liquid microjet [125] was employed. These techniques are described in Section 2.3. A small distance of <0.5 mm between the liquid jet and the orifice of the spectrometer assures that detected electrons have not suffered from inelastic scattering with gas-phase water molecules near the jet surface which enables the aqueous-phase photoemission studies [88]. The energy resolution of the U41-PGM beamline was better than 40 meV for 200 eV photon energies used for the valence PE measurements, better than 240 meV for the N 1s absorption measurements near 400 eV, and 600 meV for the Co L-edge absorption measurements at photon energies above 780 eV; the same 240 meV resolution of the beamline applies also for the RIXS measurements. The energy resolution of the hemispherical analyzer was constant with kinetic energy, 100 meV at 10 eV pass energy (used for the valence PE spectroscopy measurements), and 200 meV at 20 eV pass energy (used for all other (resonant) PE spectroscopy measurements).

The flow-cell of the LiXEdrom [80] setup was equipped with a SiC membrane of 150 nm thickness. During measurements the pressure in the main chamber was in the mid 10^{-6} mbar range. The X-ray fluorescence spectrum has been recorded using a detector mounted perpendicular with respect to the direction of the incident X-rays. The emitted X-rays are diffracted using a grating (7.5 m radius, 1200 lines/mm), and the energy-dispersed light is detected using a MCP/fluorescence screen/CCD camera stack operated at 10^{-8} mbar. Sample, grating, and detector were arranged in Rowland-circle geometry.

3.1.3 Valence RPE Spectra at Co L-edge

Figure 3.1 shows the valence PE spectrum of a 200 mM $K_3[Co(CN)_6]$ aqueous solution (in red) measured at a photon energy of 200 eV. For reference, the spectrum of neat liquid water (in blue) is also shown, obtained under identical conditions. Energies are presented as electron binding energies (BE). The peaks at 11.3, 14.35, 17.50 eV BE in the water spectrum are due to the ionization of the three outer water valence orbitals, $1b_1$, $3a_1$, and $1b_2$ [40]. The strong narrow peak at 12.45 eV arises from the $1b_1$ orbital of gaseous water, and the small narrow peaks at 12.9 and 13.2 eV correspond to $1b_1$ vibrational states. The bottom tier is the difference spectrum, subtracting water from the solution spectrum, which reveals several solute contributions. Most clearly visible is the signal due to the Co^{3+} 3d states, centered near 8.5 eV BE, and spread over a 1 eV range. Since the cobalt e_g state is empty, the 8.5 eV peak is entirely assigned to the fully occupied t_{2g} level, and represents ionization of the highest occupied molecular orbital (HOMO) of $[Co(CN)_6]^{3-}$(aq). This value is approximately 2.5 eV lower than the ionization of the highest occupied orbital of neat liquid water. The peak at 22.2 eV is due to ionization of the $K^+(3p)$ state [125]. The solute-derived spectral contributions are more visible in the RPE spectra, which moreover reveal additional spectral features; more details are provided in the following sub-section.

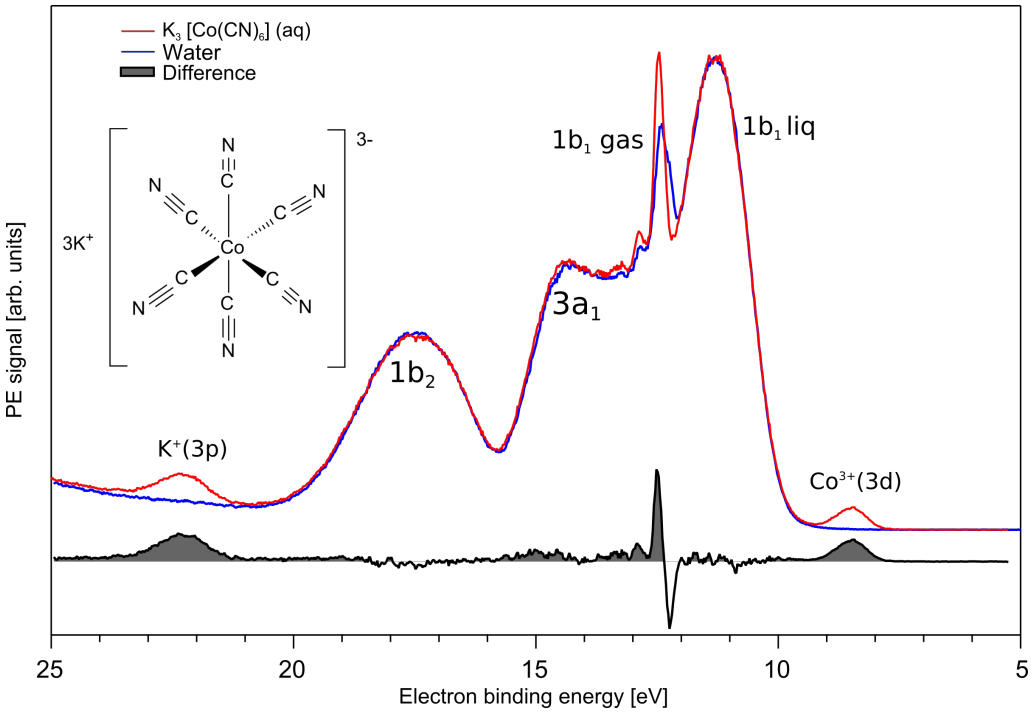

Figure 3.1: Valence photoelectron spectra of 200 mM $K_3[Co(CN)_6]$ aqueous solution (red) and pure water (blue). Both spectra are measured at 200 eV photon energy. The lower tier shows the difference spectrum of the former from the water spectrum. The structural formula of the complex is shown in the inset.

Co $L_{2,3}$-edge ($2p$ – $3d$ excitation) RPE spectra from the same 200 mM solution as in Figure 3.1 are shown in Figure 3.2. The 3-dimensional landscape plot of Figure 3.2(a) displays the electron-signal intensity as a function of both (resonant) photon energy and electron binding energy; with a 0.15 eV step width in excitation photon energy the map has been acquired within 35 minutes. Figure 3.2(b) presents the same data in two dimensions, but with the signal intensity expressed by color codes. Figure 3.2(c) shows several individual RPE spectra, each measured at the photon energy labeled E_1 – E_4 in Figure 3.2(b), marking the most noticeable resonant signal enhancements. This is the case at 13.2 eV BE (labels 2a, 2b) for excitation photon energies 782.0 (E_1) /796.5 eV (E_3), and at 20.5 eV BE (labels 1a, 1b), although the feature is much weaker, for 785.0 (E_2) /799.5 eV (E_4) excitation, respectively. I will use the notations E_1 – E_4 throughout this section when referring to the main maxima of cobalt X-ray absorption. E_1 and E_2 are then identified as the resonant energies, Co $2p_{3/2}$→unoccupied valence orbitals (L_3-edge transitions), whereas E_3 and E_4 correspond to Co $2p_{1/2}$→unoccupied valence orbitals (L_2-edge transitions). The spectrum at E_1 in Figure 3.2(c) is seen to also exhibit particularly strong enhancement, by a factor of 30, of the HOMO emission (at 8.5 eV BE, (3a)) as compared to the E_2 and the E_3 excitations; at E_4 the HOMO signal-intensity is the same as for non-resonant energies. A reference is also shown in the bottom tier of Figure 3.2(c), the off-resonant (measured at 778.0 eV photon energy) PE spectrum of the $K_3[Co(CN)_6](aq)$ solution which is largely the spectrum of neat liquid water.

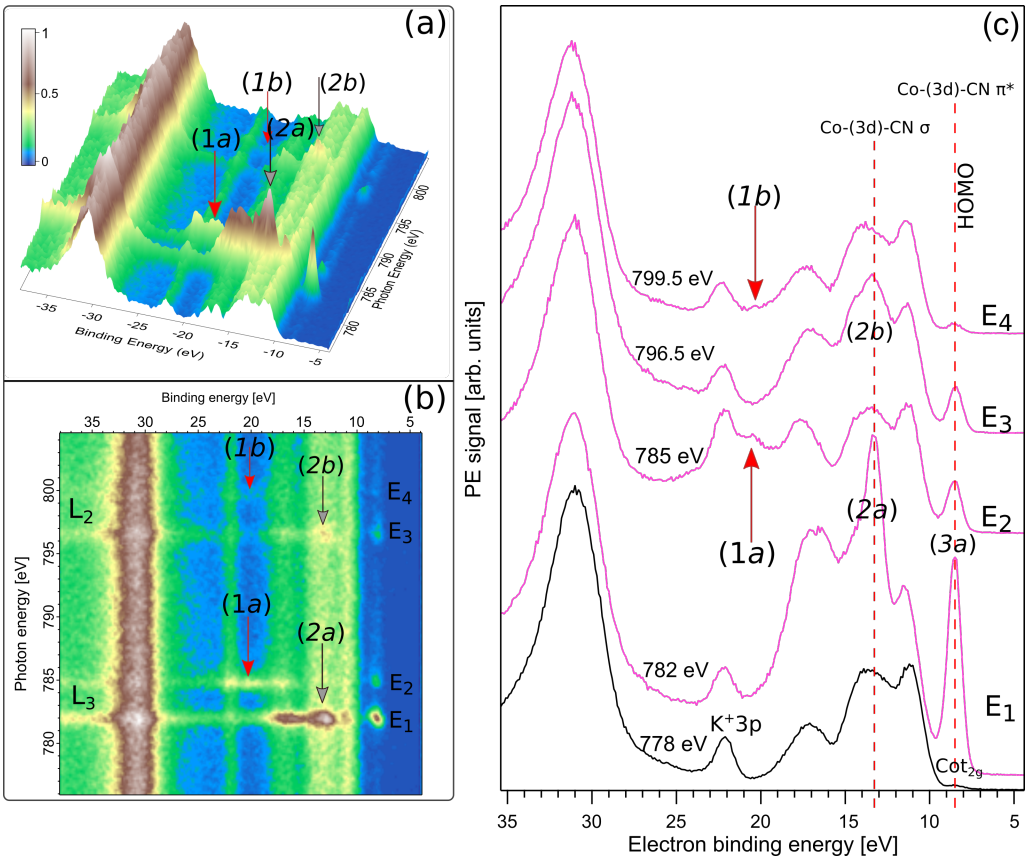

Figure 3.2: RPE spectra of 200 mM $K_3[Co(CN)_6]$ aqueous solution obtained upon tuning the photon energy across the Co L-edge. (a) shows the electron intensity in a 3D landscape on the binding energy scale; the important signal enhancements at resonance energies are marked with red (1a, 1b) and black (2a, 2b) arrows. (b) presents the respective 2D plot. E_1, E_2, E_3, and E_4 mark the resonant excitations at the L_3 and L_2 edges. (c) illustrates the off-resonant (in black) and all other resonant (in pink) excitations. The vertical dotted lines and arrows mark the different resonance-enhanced states of interest.

Signal increases in the >30 eV BE range (Figures 3.2(a), (b)) result from inelastic electron scattering, reflecting the large number of Auger electrons produced at resonance. As was briefly the mentioned signal enhancement at resonant excitation originates from the quantum mechanical interference of electron waves associated with two different photoemission pathways, but leading to the same final state. The situation is illustrated in Figure 3.3 for several relaxation processes relevant here.

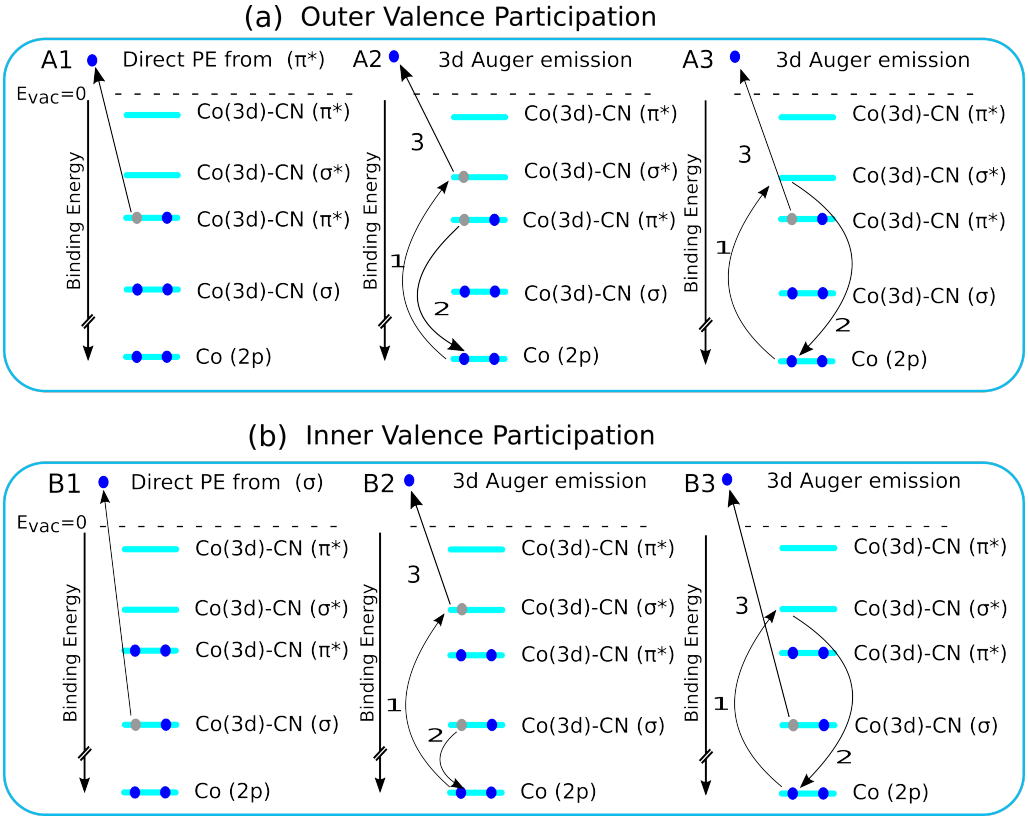

Figure 3.3: Illustration of the resonantly enhanced photoemission at Co L_3-edge excitations, (E_1 and E_2 in Figure 3.2). Outer valence participation (a) explains the peak intensities at 8.5 eV (Figure 3.2 (c), feature 3a), and inner-valence participation (b) explains the resonant enhancement at 13.2 eV (Figure 3.2(c), features 2a, 2b) binding energy. A1 and B1 represent the direct PE from the outer and inner valence orbitals. A2, A3, B2 and B3 depict the Auger contributions to the signal enhancements at E_1 and E_2 resonant excitations, respectively. The orbital mixing and bonding nature obtained from ground state DFT calculations are also shown. More details regarding the orbital mixing are explained in Section 3.1.9.

In the top tier (A), Figure 3.3-(A1) shows the direct ionization of the HOMO of the $[Co(CN)_6]^{3-}$ complex. At the lowest resonant excitation, Co $2p$→LUMO, the processes of Figures 3.3-(A2) and 3.3-(A3), representing participator Auger decay, will result in the emission of Auger electrons with the same kinetic energy as the direct photoelectron. Note that the processes depicted in Figures 3.3-(A2) and 3.3-(A3) differ in the energy levels involved in the relaxation but the net effect, i.e., the energy of the Auger electron, is the same. The analogous situation for deeper-valence ionization/relaxation is presented in the bottom tier (b) of Figure 3.3; details are described in the figure caption.

Next, I will assign all peaks that get enhanced upon resonant excitation (Figures 3.2(a), (b)) based on the well understood valence-photoionization spectrum of liquid water. An analysis based on ground-state DFT calculations is presented thereafter.

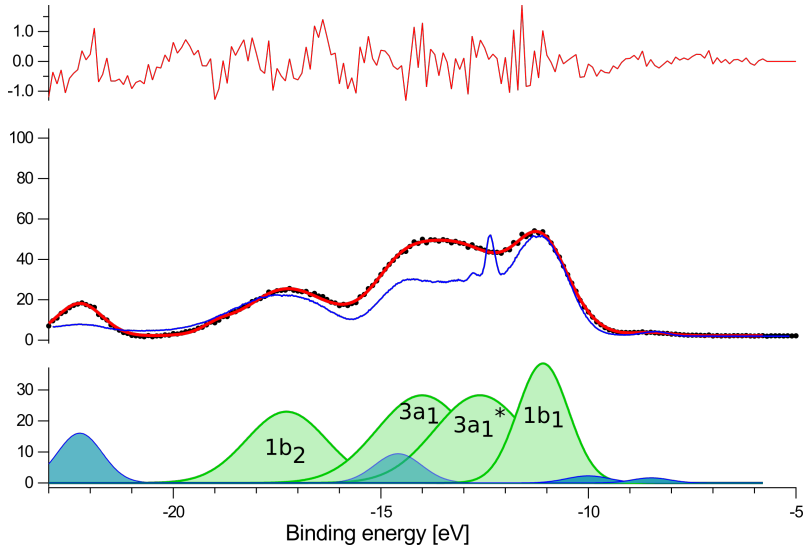

Figure 3.4: Valence off-resonant PE spectra from 200 mM $K_3[Co(CN)_6]$ aqueous solution measured at 778 eV photon energy (black dotted line) and valence PE of neat liquid water measured at 200 eV photon energy (blue). The green peaks are Gaussians representing the energy positions and widths of the PE peaks due to ionization of the water orbitals, $1b_1$, $3a_1$, and $1b_2$. Here, intensities of these Gaussians were allowed to vary in order to fit the 778 eV solution spectrum. A perfect fit is, however, only possible if four additional Gaussians, representing solute signal contributions are introduced. These peaks are shown in blue. Their positions are at 8.5, 10.0, 14.6, and 22.2 eV BE. The 8.5 eV peak is due to ionization of the HOMO of $[Co(CN)_6]^{3-}$ (aq), and 22.2 eV arises from ionization of K^+ $3p$ (aq). The peak at 14.6 eV must be attributed to some deeper-lying state of $[Co(CN)_6]^{3-}$(aq).

First, I compare the off-resonant PE spectrum (bottom tier) of Figure 3.2(c) with that of Figure 3.1, measured at much lower photon energy. Both spectra are reproduced in Figure 3.4. Differences in the relative intensities of peaks are due to the different cross sections for water ionization at 778.0 versus 200 eV. Important though, the 778.0 eV solution spectrum was accurately reproduced using the same Gaussian peak widths and BE positions of the 200 eV neat water spectrum. The small extra signal intensities from the solute are reproduced by four additional Gaussians. Their positions are at 8.5, 10.0, 14.6, and 22.2 eV. The 8.5 eV (HOMO) and the 22.2 eV (K^+ $3p$) peaks have been already identified in Figure 3.1. The 10.0 eV and 14.6 eV peaks can be attributed to ligand ionization, detailed in the following section. The signal enhancement at resonant excitation is the reason for observing the 20.5 eV peak (1a, 1b) in the Co $2p$ RPE spectra (Figure 3.2(c)) but not in the off-resonant spectra (Figure 3.4), in which case the ionization cross section is too small.

3.1.4 Co L-edge RIXS Map and Spectra

In figure 3.5(a) I present the Co $L_{3,2}$-edge RIXS plane, i.e., emitted X-ray intensities as a function of excitation and emitted photon energy.

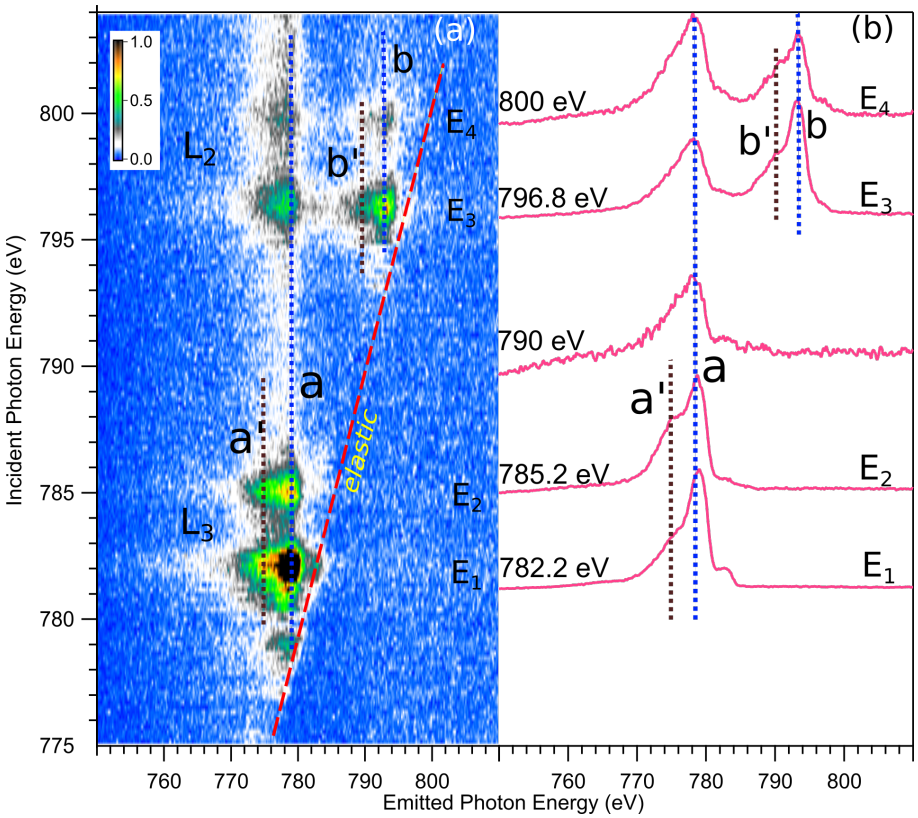

Figure 3.5: (a) Cobalt L-edge RIXS plane. The slanted red line shows the elastic spectral line, the vertical dotted blue (a) and black (a') lines show the constant-energy emission features. (b) Selected constant incident energy spectra obtained for a longer duration. E_1 and E_2 correspond to the resonant excitations at the L_3-edge, E_3 and E_4 correspond to the L_2-edge. The spectrum at 790.0 eV excitation presents the non-resonant XE. All spectra are normalized and shifted along incident photon energy axis. Spectral features at the L_2-edge excitations are shown by dotted lines b and b'.

Total acquisition time was approximately 175 min, and includes the measurement of 150 individual RIXS spectra in the 775–805 eV photon emission range of the $3d - 2p$ transitions. The strongest X-ray emission signal is observed at the same excitation energies E_1 through E_4 as for the electron channels (Figure 3.2). Corresponding individual RIXS spectra, which are horizontal cuts through Figure 3.5(a) at E_1, E_2, E_3, and E_4, respectively, are shown in Figure 3.5(b). Intensities are displayed to yield the same peak height at maximum emission. Positions of the respective elastic peaks, located along the tilted line (red) in the RIXS plane, are used for energy calibration of the emitted-photon-energy axis. The main feature in the L_3-edge RIXS spectra is an emission peak at 779.0 eV (label a) and a shoulder at 775.0 eV (a'). Very similar peak shapes are observed at the L_2-edge (E_3, E_4), but in addition, a smaller-intensity structure occurs at higher emission energies, peaking at 793 eV (label b) and 789 eV (b'). Feature a corresponds to the filling of the Co $2p_{3/2}$ core-hole by an electron of the occupied valence orbitals, whereas feature a', 4.0 eV below feature a, must be assigned to an electron transition from some inner-valence orbital of considerable metal character. Features b and b' correspond to the transitions from the outer and inner

valence orbitals to Co $2p_{1/2}$. Note that the energy spacing between b and b' is the same as for a and a'. The latter transitions are indicated in Figure 3.6, which is an energy-level diagram of all experimentally inferred cobalt-derived orbitals, but also computed energies as well as orbital characters, which are yet to be detailed, are included. The energy axis of Figure 3.6 is based on the experimental BEs from Figures 3.1 (valence PE spectrum is reproduced at the bottom) and Figure 3.2. In addition, I have also included the Co $2p_{3/2}$ PE spectrum (also presented at the bottom), revealing 786.0 eV BE. The energy values of a and a' are seen to match the energy differences between the occupied valence and the $2p$ core level; the same applies for the transitions into Co $2p_{1/2}$, which are not considered in Figure 3.6. From the value of the Co $2p_{3/2}$ BE combined with the resonance energies E_1 and E_2 (Figures 3.2 and 3.5) the binding energies of the relevant unoccupied valence orbitals read 4.5 eV and 1.5 eV. The two excitations are indicated by the vertical arrows in the Figure 3.6.

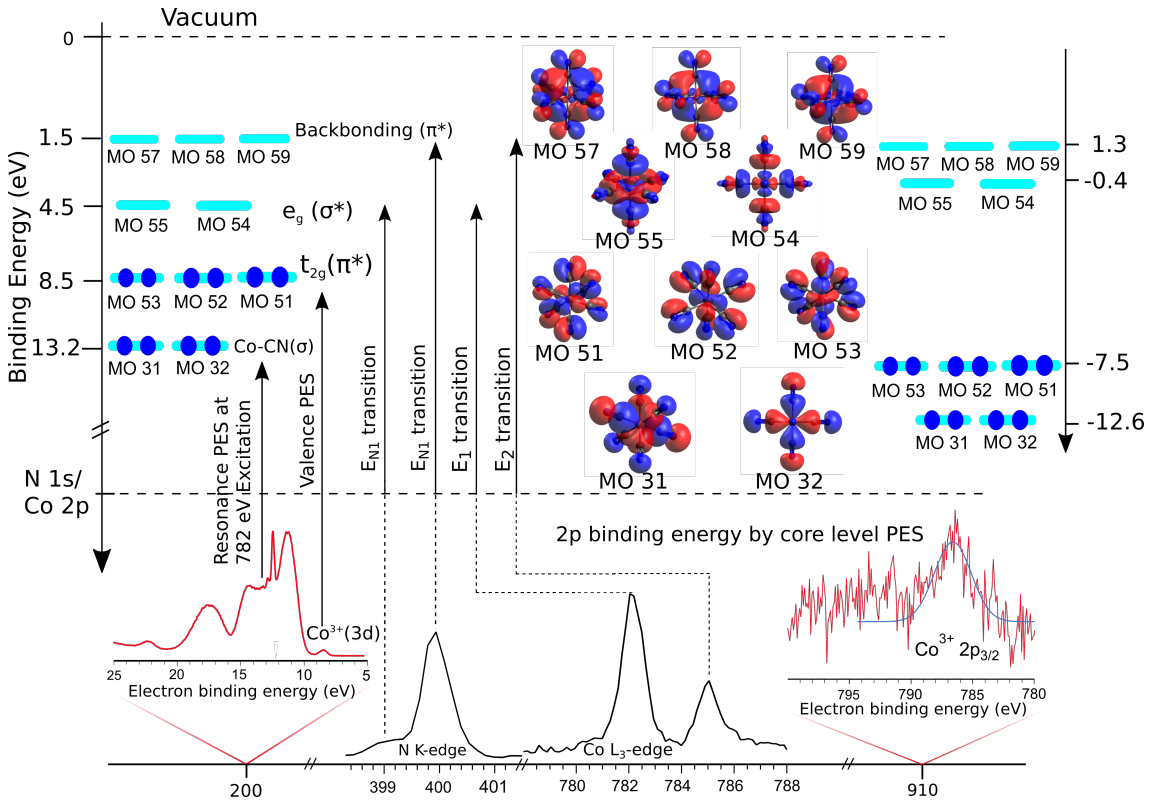

Figure 3.6: The important experimental and calculated binding energies of the $K_3[Co(CN)_6](aq)$ complex. The energy scale on the left side shows the experimentally obtained binding energies inferred from core-level and valence PE spectra, and from PEY-XA spectra. The horizontal axis in the bottom shows the energy ranges used for probing the system. The calculated important orbital shapes are illustrated in the middle [126]. On the right side a calculated energy scale is also presented (not to scale).

3.1.5 Co L-edge PEY- and PFY-XA Spectra

Calculation of RPE and RIXS spectra remains computationally challenging, whereas the resulting PEY and PFY-XA spectra can be simulated with very high accuracy. The experimental XA spectra are obtained by integration of the signal intensities of individual, subsequent RPE/RIXS spectra measured across the resonance. In the present case this corresponds to projecting the total intensity of a given horizontal cut through Figure 3.2(b) and 3.5(a), respectively, on the excitation photon energy axis; this however considerably reduces the available spectroscopic information. The resulting partial-yield XA spectra are shown in Figure 3.7, PEY-XA in green and PFY-XA in blue. The four prominent absorption bands (E_1 - E_4) correspond to the E_1 through E_4 excitations, respectively, also illustrated in Figure 3.7. The computed XA spectrum is shown in black (Figure 3.7), and a detailed discussion will be given along with the DFT/ROCIS calculations, in Section 3.1.9. The two experimental XA spectra are very similar, and because of the rather high noise level of the PFY-XA spectrum anticipated minor differences arising from detection of non-radiative versus radiative channels [123] are not resolved. For that reason we can attribute the broadening of the E_1 feature towards lower absorption energies in the PFY-XA spectrum (and absent in the PEY-XA spectrum) to the difference in final states [123] or to some experimental artifact.

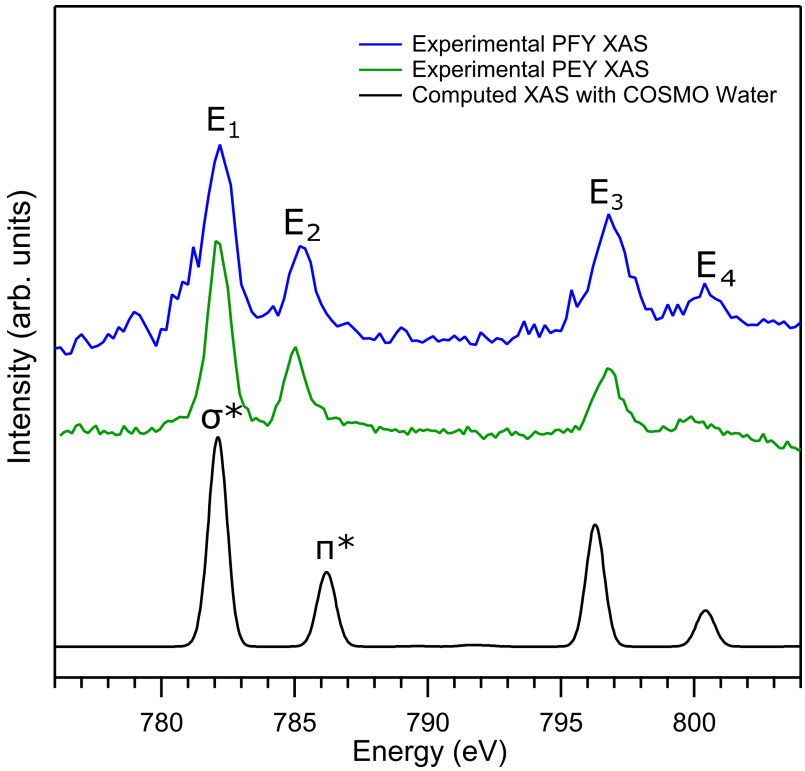

Figure 3.7: The RIXS and RPE signal integrated Cobalt L-edge (left panel) PFY and PEY XA spectra from 200 mM $K_3[Co(CN)_6]$ aqueous solution. The solvent-effect-included calculated XA spectrum is shown in the bottom tier. Important features are marked as E_1 to E_4.

3.1.6 Nitrogen K-edge RPE Map and Spectra

Figure 3.8 shows the 3-dimensional (in (a)) and 2-dimensional (in (b)) resonant valence PE map at the N K-edge from 200 mM $K_3[Co(CN)_6]$ (aq); these presentations are fully analogous to Figures 3.2(a) and 3.2(B) for the Co 2*p* edge. Most noticeable is the electron emission intensity in the 16–24 eV BE range and near 11 eV BE, for 399.8 eV excitation photon energy. The latter coincides with the neat water $1b_1$ BE. Signal around 22 eV BE is convoluted by K^+ (aq) emission, and signal at 17.5 eV arises from water $1b_2$. There is another signal enhancement near 20.5 eV BE (marked by the red arrow) which is however only revealed when subtracting the non-resonant spectrum from the resonant PE spectrum. Note that enhancement of the 20.5 eV BE peak intensity has been also observed at the Co 2*p* resonance (Figure 3.2(c)), implying that the respective orbital must be of ligand–metal mixed character. Figure 3.8 also reveals smaller electron signal, occurring at 8.5 eV BE (marked by black dotted line), and its intensity is also highest for 399.8 eV excitation energy. This peak at 8.5 eV arises from HOMO ionization of the metal complex as previously discussed. At the same excitation energy, a slightly enhanced electron emission near 11.0 eV BE is also observed (marked by the black arrow) which appears to coincide with the 10.0 eV peak identified in the off-resonant valence PE spectrum of Figure 3.4. Since this peak is not enhanced in the Co 2*p* RPE spectra of Figure 3.2(c), this feature must be of nitrogen character. Qualitatively, in accordance with the previous valence PE spectroscopy studies on $[Fe(CN)_6]^{4-}$(aq) [127], the 10.0 eV peak can be assigned to the CN^- π -orbitals. The following section will show that this is also in agreement with ground state DFT calculations.

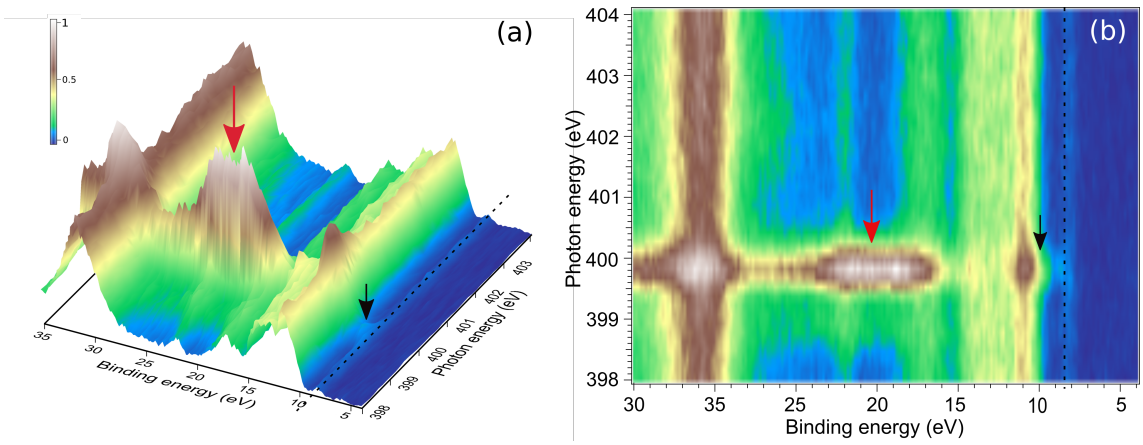

Figure 3.8: RPE spectra of 200 mM $K_3[Co(CN)_6]$(aq) obtained upon tuning the photon energy across the N K-edge. The important features are marked by arrows and dotted lines.

3.1.7 Nitrogen K-edge RIXS Map and Spectra

Figure 3.9(a) presents the N K-edge RIXS plane including 100 individual RIXS spectra; total acquisition time was 140 min. As for the Co 2*p* RIXS map (Figure 3.5(a)), the signal

along the slanted line corresponds to the elastic peak, and serves for energy calibration. Strongest emission intensities are observed in the approximately 385–395 eV range, at the resonant excitations 399.0 eV (denoted E_{N1}) and 399.8 eV (E_{N2}). Weaker emission intensity in the same energy range is observed for excitation photon energies larger than 402 eV. Increase of the elastic peak intensity at the E_{N2} resonance originates from a larger probability for filling the 1*s* core-hole by direct decay of the excited electron [128], which is accompanied by the enhancement of Auger decay, as seen in Figure 3.8. The most noticeable emission features in Figure 3.9(a) are collected for longer duration for obtaining RIXS spectra, measured at E_{N1}, E_{N2}, and at two energies, 402.2 and 404.4 eV; the latter correspond to electron excitation into the continuum. The spectra are shown in Figure 3.9(b). Signal intensities are displayed to yield the same peak height at maximum emission. All spectra are seen to exhibit a similar 385–395 eV broad-band emission, with the main difference being the distribution of relative intensities within the band. One can use the latter to divide the band into four spectral regions, 1-4, as indicated in Figure 3.9(b).

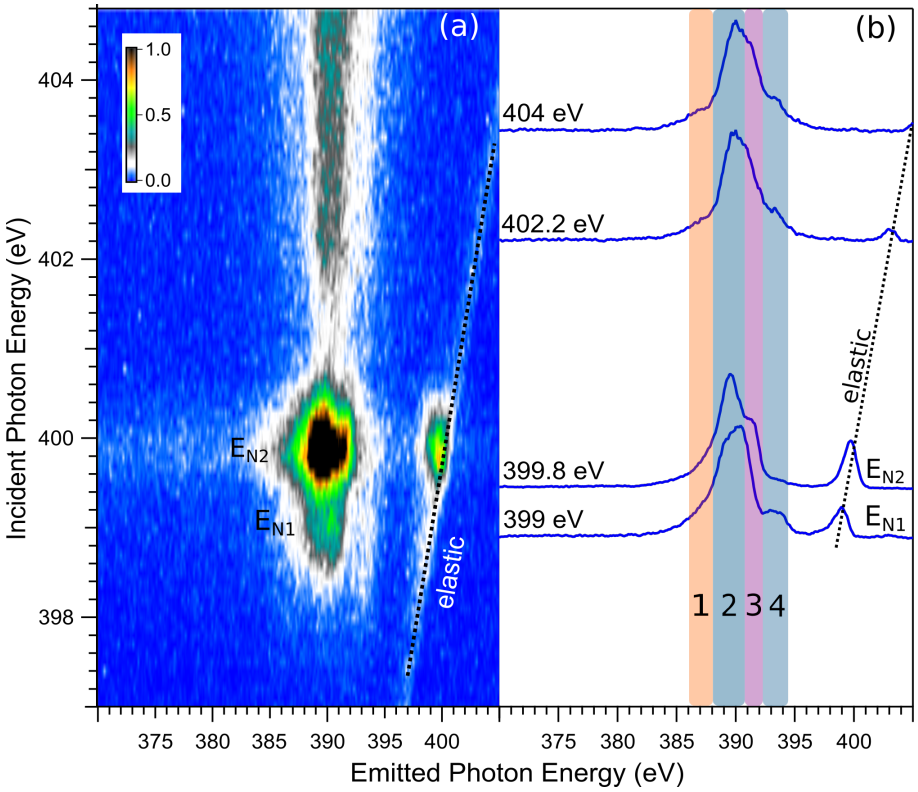

Figure 3.9: (a) Nitrogen K-edge RIXS plane. The slanted black dotted line corresponds to the elastic emission. (b) 1D spectra excitation energies E_{N1} and E_{N2}; acquisition time was 20 times longer than for the respective traces of the RIXS plane.

Lowest-energy feature 1 has a small intensity; it yet becomes stronger and more pronounced when going from 399.0/399.8 eV to 402.2/404 eV resonant excitation. Feature 2 has the largest intensity in all spectra, and spectral shape stays largely unchanged at all excitation energies. Feature 3 is a shoulder (overlapping with 2) of varying intensity, and only at 399.8

eV (E_{N2}) it forms a rather distinct peak; intensity is lowest at 399.0 eV (E_{N1}). Feature 4 is an only slightly larger peak than feature 1. It nearly vanishes at E_{N2}. The spectral division into 1–4 features is indeed meaningful and correlates with the non-resonant XE-spectra calculations shown in (Figure 3.14) detailed below in Section 3.1.9.

3.1.8 Nitrogen K-edge PEY- and PFY-XA Spectra

The experimental PFY- and PEY-XA spectra for the N K-edge are shown in Figure 3.10 along with a calculated spectrum (bottom tier) where solvent effects have been included. XA spectra are generated from Figures 3.8 and 3.9, analogous to the procedure explained for the Co 2*p* partial yield XA spectra. The two experimental spectra exhibit the very similar broad single absorption band at 399.8 eV (E_{N2}) and a wide shoulder near 399.0 eV (E_{N1}); possible spectral differences arising from photon versus electron detection [30] cannot be quantified here as improved signal-to-noise level (particularly of the data shown in Figure 3.9(A)) would be needed.

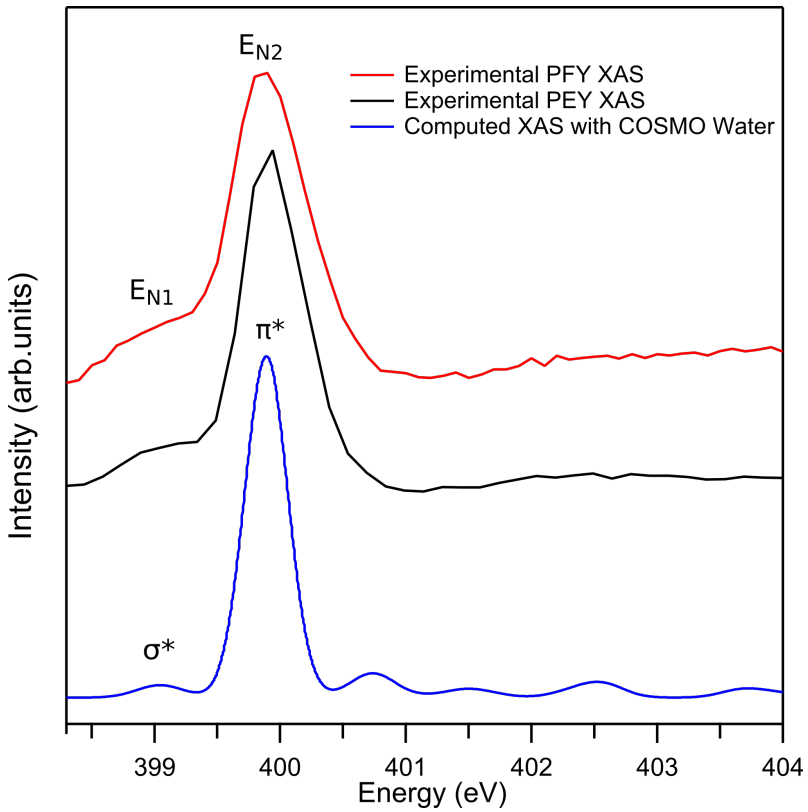

Figure 3.10: The RIXS and RPE signal integrated N K-edge PFY- and PEY-XA spectra (red and black tiers, respectively). The blue spectrum at the bottom is obtained from TD-DFT calculation. E_{N1} and E_{N2} mark the resonance energies; same as in Figure 3.9.

Qualitatively, the absorption at E_{N1} and E_{N2} corresponds to the promotion of an N 1*s* electron to unoccupied valence orbitals as indicated in Figure 3.6.

3.1.9 Results from Electronic-Structure Calculations

The calculations were carried out with the ORCA software package [92], described in Section 2.4. Molecular geometry optimizations were performed using the M06 [129] density functional method with the def2-TZVP(-f) basis set [130]. Transition energies and moments for the Co L-edge were calculated with DFT/ROCIS using the same basis set and B3LYP [131, 132] functional. For the N K-edge, TD-DFT method was employed, again using the same functional and basis set. For DFT/ROCIS calculations, the B3LYP functional with the parameters c_1=0.18, c_2=0.20, and c_3=0.40 [93] was used. During the calculations, the resolution of identity [133–137] approximation was used employing the def2-TZV/J auxiliary basis set [138]. Numerical integrations during the DFT calculations were performed on a dense grid (ORCA grid 5). L-edge and K-edge absorption spectra were obtained by applying a 0.8 eV and 0.4 eV Gaussian-type broadening on each transition moment respectively. The geometry calculations had no symmetry constraint. For XES calculations, the B3LYP functional along with the def2-TZVP(-f) basis set was used and the integrations were carried out on a dense grid (ORCA grid 5). In all calculations, the relativistic effects were taken into account using ZORA [98] method. The solvent effects were accounted for using the COSMO (water) method in ORCA [139].

Energy and Character of Metal-Derived Occupied Valence Orbitals

For a theoretical interpretation of the peaks at 8.5 eV (peak 3a) and 13.2 eV (peaks 2a, 2b,) BE in the Co 2*p* RPE spectra of Figure 3.2(c) (see also Figure 3.6), ground-state single-point DFT calculations were performed to reveal the nature of the corresponding occupied MOs. Computed orbital energies as well as the relative atomic characters, i.e., percentages of Co, N, and C from Löwdin population analysis, are presented in Figure 3.11(a).

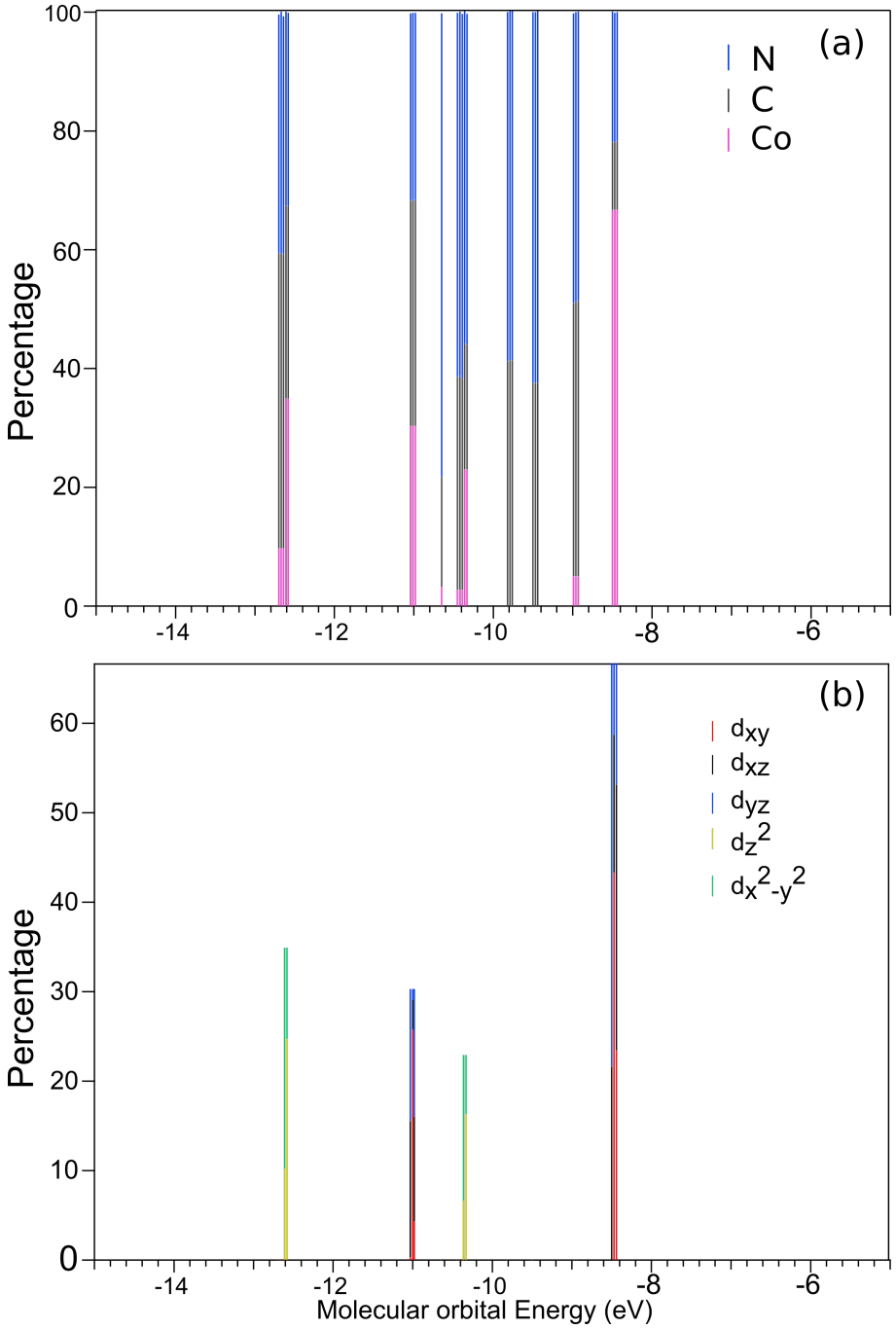

Figure 3.11: Computed valence Löwdin population analysis in molecular orbital energy scale. (a) Presents the contributions from Co (Pink), C (grey) and N (blue). (b) Gives the molecular orbital participation from Co d orbitals alone. An energy offset of 0.03 eV is introduced to make the degeneracies more comprehensible.

Further analysis was carried out for identifying the particular nature of the metal 3d orbitals, and relative contributions from d_{xy}, d_{xz}, d_{yz}, d_{z^2}, and $d_{x^2-y^2}$ are depicted in Figure 3.11(b). The calculated orbital energies were shifted by +1.08 eV to match the experimental BE values. Figure 3.11(b) reveals the expected dominant Co 3d character of the HOMO originating from the hybridized Co–C π^* orbitals. This is inferred from the

fact that only contributions are from d_{xy}, d_{xz}, and d_{yz} which are the antibonding (π^*) t_{2g} symmetry orbitals. These are the MOs #51, 52, 53 in DFT calculations; their respective orbital shapes are shown at the right side in Figure 3.6. The photoemission occurring at 13.2 eV in the experiment is argued to correspond to the orbitals calculated at 12.6 eV. As seen in Figure 3.11(a) these molecular orbitals (MOs), #31, 32, have mainly cyanide character (≈65%) and smaller Co 3*d* character, with the latter being comprised of d_{z^2} and $d_{x^2-y^2}$ orbitals, these are the hybridized Co–CN σ-type bonding orbitals.

Co L-edge: Interpretation of RIXS Spectra Assisted by XE-Spectra Calculation

Non-resonant XE-spectra calculations have been performed based on transition-dipole-moment calculations between the MOs. The calculated spectrum shown in Figure 3.12 is found to reasonably well reproduce the experimental 790 eV XE spectrum of Figure 3.5(b).

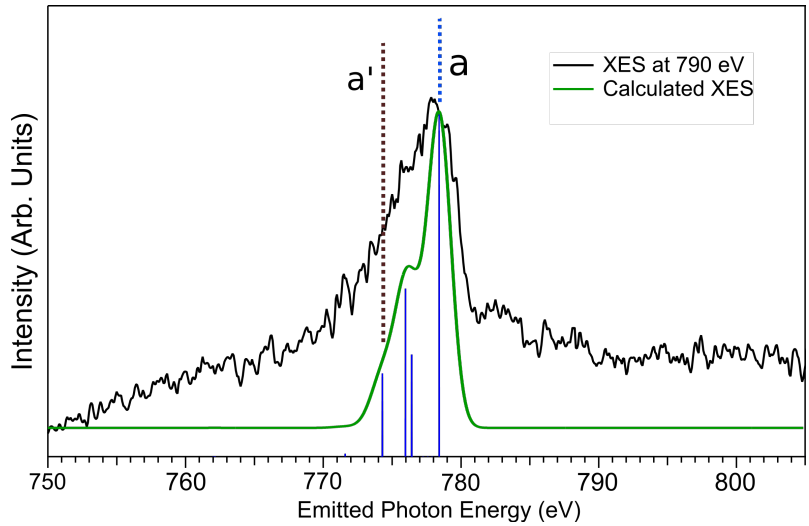

Figure 3.12: The off resonant experimental cobalt XE spectra from 200 mM $K_3[Co(CN)_6]$(aq) at 790 eV compared with the calculated spectrum. A Gaussian broadening of 2 eV was used for the calculated spectrum.

Four sets of transitions centered at 774.2, 776.0, 776.2, and 778.2 eV are found to contribute with different weights. Energy positions are given by the sticks in Figure 3.12, and probabilities are indicated by the heights of the sticks. Representing each stick by a Gaussian with 2 eV width then yields the computed XE spectrum in Figure 3.12. Calculations reveal that the strongest emission in the experimental spectra, at 779 eV (transition a in Figure 3.5(b)), results from HOMO-2, HOMO-1, and HOMO (MOs #51–53) to Co $2p_{3/2}$. The respective orbitals and their energies are indicated in Figure 3.6. The transitions at the calculated energies 776.0 / 776.2 eV can be connected with the two sets of Co–C π (#33, #34, #35) and Co–C σ^* (#37, #38) orbitals. The orbitals responsible for transition a' (calculated at 774.2 eV) can be traced to orbitals #31, 32 which had already identified as Co-CN σ-type bonding orbitals. According to Figure 3.6 the experimental energy difference between a and a‘ is approximately 4.7 eV which is close to the 5.1 eV value

obtained in the ground-state energy calculation. The calculated energy difference based on the excited-state XE spectral calculations is only 4 eV (not shown in Figure 3.6) which can be attributed to an overestimation of correlation between valence-to-core electrons in the presence of a core hole.

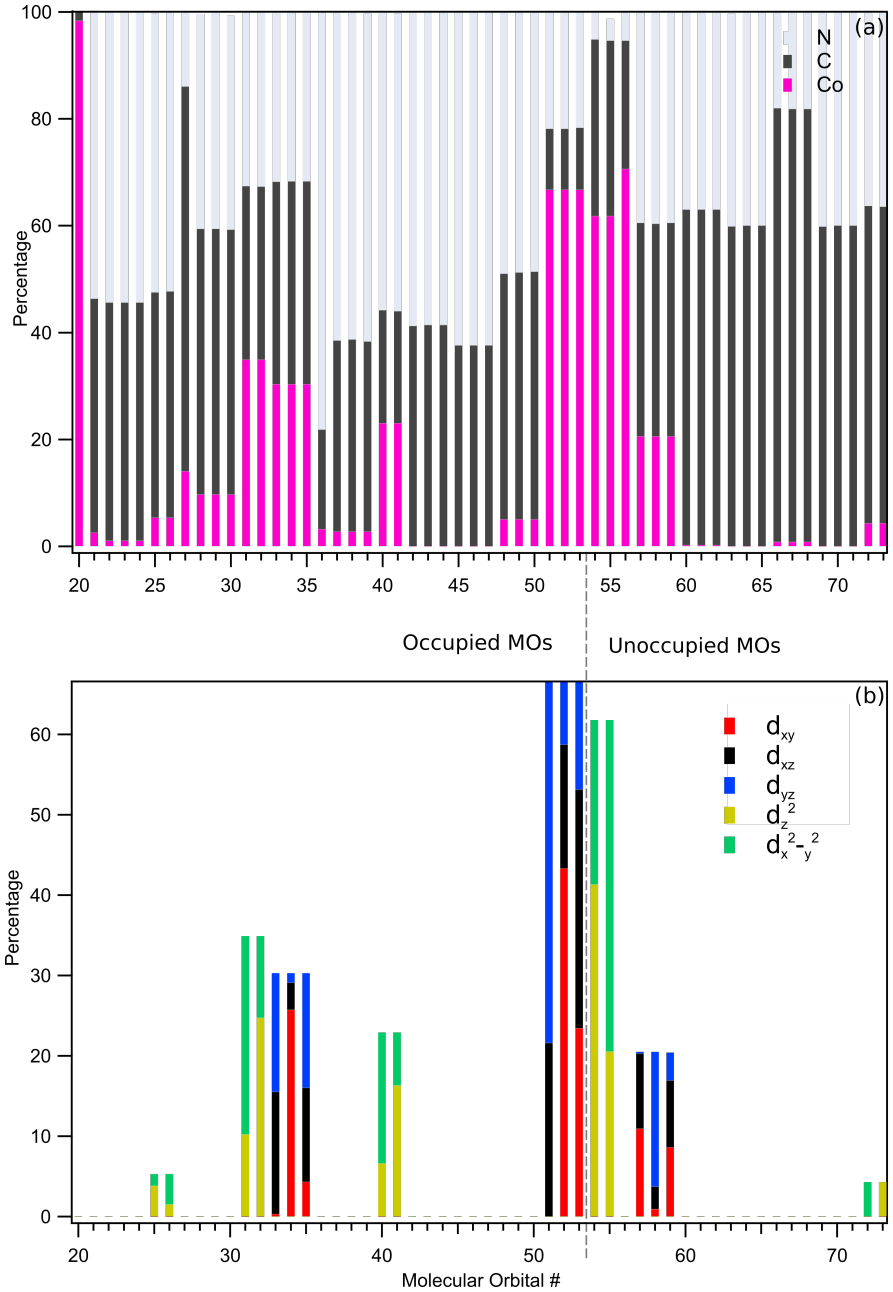

Figure 3.13: Löwdin population analysis for $[Co(CN)_6]^{3-}$ obtained from single point DFT calculations. The top tier (a) presents different atomic contributions, and the bottom tier (b) shows the Co 3*d* contribution to the various MOs. The unoccupied and occupied MOs are separated by the black dotted line between MOs #53 and #54.

Next, it is important to understand the actual character of the orbitals relevant for the interpretation of the main features of the experimental XE spectra (Figure 3.5(B))

in more detail. Figure 3.13(a)) presents the relative element-specific contributions to a given MO, and Figure 3.13(b) details the contributing Co 3*d* character in terms of d_{xy}, d_{xz}, d_{yz}, d_{z^2}, and $d_{x^2-y^2}$ orbitals, both obtained from Löwdin population analysis [109]. The small shoulder at 775.0 eV emission in the experimental XE spectrum (feature a' in Figure 3.5(b)) can be associated with orbitals which are of Co–CN σ bonding character, according to Figure 3.13(a), this involves MOs #31 and #32 with approximately 35% Co (3d-e_g) character. The two close-lying calculated transitions at 776.0 and 776.2 eV (Figure 3.12) originate from MOs #33 to #39, all of which have dominant CN^- ligand character, approximately 70% in MOs #33–35 and 95% in MOs #36–39. Analogously, HOMO, HOMO-1, and HOMO-2 are attributed to the strongest feature a at 779.0 eV, these are of Co-CN π^* anti-bonding character. These MOs are #53, #52 and #51 and have approximately 65% Co (3d-t_{2g}) character, consistent with their intense contribution in the Co RIXS spectra.

Nitrogen K-edge: Interpretation of RIXS Spectra Assisted by XE-Spectra Calculations

The calculated N XE spectrum along with the experimental spectrum measured at 404 eV excitation energy, is shown in Figure 3.14. The calculations reveal four groups of transitions, near 387.8, 390, 391, and 392 eV, very well matching our division into spectral regions 1-4 which was introduced in Figure 3.9. In Figure 3.14 computed energy positions

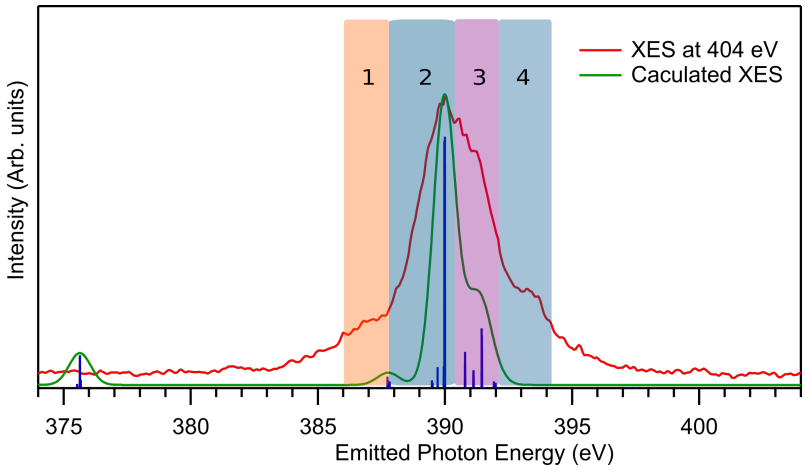

Figure 3.14: Comparison between the experimental XES (red) from 200 mM $K_3[Co(CN)_6]$(aq) at 404 eV excitation with the calculated XES (green). A Gaussian broadening of 1 eV was used for the calculated spectrum and has been shifted by 12 eV to match the experimental spectrum. The calculated spectrum shows a feature around 375.8 eV, but experimental spectrum does not show this feature.

are presented by sticks, and the respective transition probabilities are given by the stick heights. Representing the individual sticks by Gaussians, and applying 1 eV broadening, the theoretical (green) spectrum is obtained which is in fairly good agreement with the experimental 404 eV XE spectrum of Figure 3.9(b). Based on the calculations X-ray

emission feature 1 is attributed to the refill of the N 1s core-hole by electrons from the mixed Co (3d-e_g) and CN^- orbitals which have σ-character (#31, #32). The low intensity of feature 1 is attributed to the considerable Co (3d-e_g) contributions to these valence orbitals which is supported by Figure 3.13 (see orbitals #31 and #32). The main emission-feature 2 is attributed to the relaxation of electrons (nearly 100%) from CN^- orbitals to the N 1s core-hole. The orbitals responsible for emission in this energy are MOs #36-39 as can be seen from Figure 3.13. For feature 3, three transitions are observed (see the blue sticks near 391 eV in Figure 3.14). The orbitals emitting in this range have mainly CN^- character, and Co 3d contributions are very minor (Figure 3.13, orbitals #42-50). The reason for the intensity enhancement of feature 3 at E_{N2} resonant excitation (Figure 3.9) is not understood. Finally, emission feature 4 which is strongly enhanced at E_{N1} excitation is found to originate from the Co–CN outer-valence orbitals, HOMO-2, HOMO-1, and HOMO (MOs #51-53) which have more than 65 % Co (3d-t_{2g}) contributions (see Figure 3.13(a)).

Computed Co L-edge PEY and PFY-XA Spectra

With the aid of DFT/ROCIS calculations, which well reproduce the experimental XA spectra (see black curve in Figure 3.7, also shown in Figure 3.16 with orbital characters marked), the absorption features can be accurately assigned to their respective transitions. The first intense peak E_1 (782 eV) is thus attributed to the $2p \rightarrow \sigma^*(e_g)$ transitions; these MOs are the two lowest unoccupied molecular orbitals (LUMO, LUMO+1) of the molecule. This transition is indicated in the energy-level diagram of Figure 3.6. Here the energy of the 786.5 eV BE of Co $2p_{3/2}$ has been taken from the respective core-level PE spectrum shown in Figure 3.15, and the spectrum is also reproduced at the bottom of Figure 3.6.

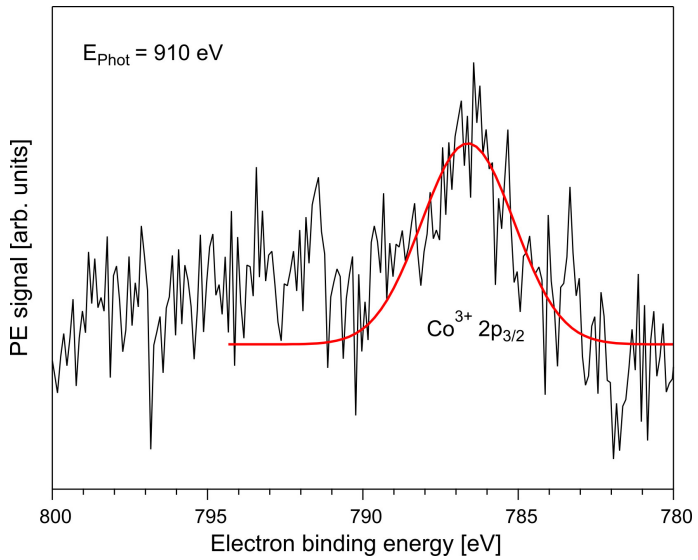

Figure 3.15: Co $2p_{3/2}$ binding energy of 200 mM $[Co(CN)_6]^{3-}$(aq), obtained from core PE spectra measured at 910 eV photon energy.

The second peak E_2 (785.0 eV) in Figure 3.7 can be assigned to $2p \rightarrow \pi^*$ transitions, which corresponds to π-backbonding, characteristic of transition-metal complexes with strong field ligands. The origin of this feature is the mixing of Co $3d$ t_{2g} orbitals with the empty $2\pi^*$ orbitals of CN^- forming an occupied deeper valence bonding orbital and an unoccupied anti-bonding valence orbital of the same symmetry. The computed orbital shapes of the π^* orbitals (57-59) as well as the respective experimental and theoretical binding energies are also shown in Figure 3.6. Note that the σ^* and π^* band positions (peaks E_1 and E_2; see also the assignments made in Figure 3.16) are in reasonable agreement with aforementioned total-electron yield (TEY) XA spectra from powdered samples [38]. However, the L_2 peak in the present work is shifted to 1.2 eV lower energy compared to the powder study [38], which may be indicative of a solvent effect.

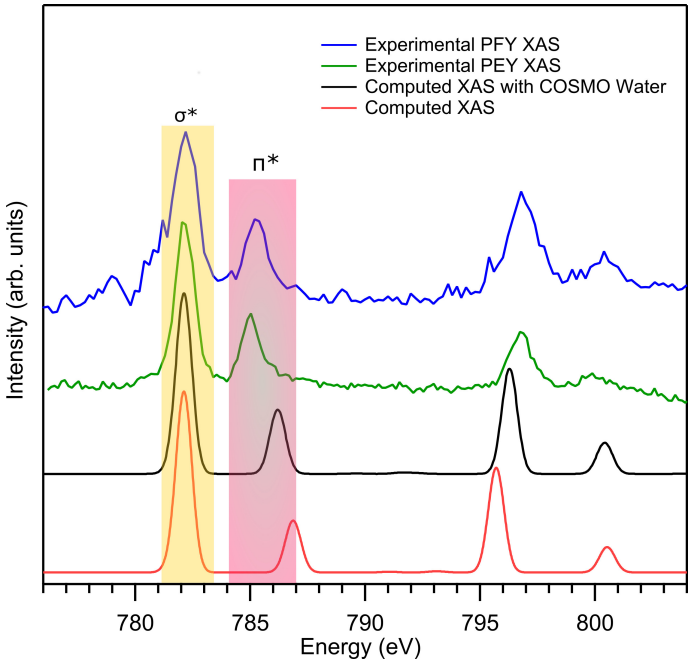

Figure 3.16: Experimental cobalt L-edge XA spectrum from PFY and PEY measurements from 200 mM $K_3[Co(CN)_6](aq)$, along with computed XA spectrum with spin orbit coupling included DFT/ROCIS calculations. The spectrum on the lower tier (red) shows the calculated spectrum without the solvent effect, the notable difference is the position of the transition to the π^* MOs.

Qualitative Probing of Bonding Strength – N K-edge PEY and PFY-XA Spectra and Theory

The strength of the π-backbonding is determined by the extent of orbital mixing, and this should be reflected in the intensity of the respective absorption bands. Probing π-backbonding will hence depend on the particular excitation. For instance, if the (unoccupied) orbitals responsible for the π-backbonding have dominant metal character we expect that the respective spectral contributions are larger for the metal $\rightarrow \pi^*$ than for ligand

$\rightarrow \pi^*$ transitions. This provides a spectroscopic means for the qualitative analysis of the strength of bonding and will be discussed next.

In order to evaluate the effect of metal versus ligand excitation on the σ^*-to-π^* band intensity ratio, it is important to assign the experimental nitrogen K-edge PFY-XA and PEY-XA spectra of shown in Figure 3.10 (also shown in Figure 3.17 with σ^* and π^* bands marked) with the help of the TD-DFT calculations.

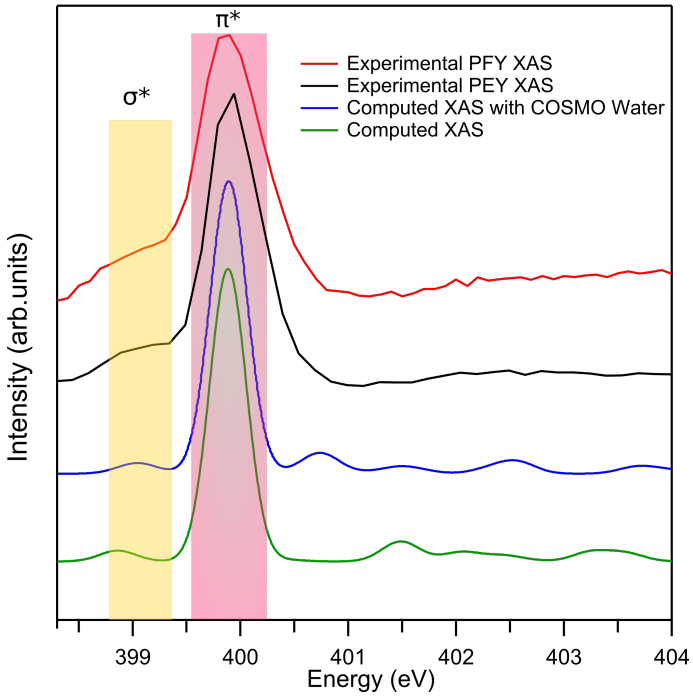

Figure 3.17: Experimental N K-edge XA spectra from PFY and PEY measurements from 200 mM $K_3[Co(CN)_6](aq)$, along with computed XA spectra using TD-DFT calculations. The blue and green spectra illustrate the computed XA with and without solvent effect respectively. The solvent effects were included using the COSMO water function.

The computed XA spectrum, with solvent effect included, which has already been included in Figure 3.10, is seen to be in good agreement with the two experimental spectra. Based on the calculations the first absorption E_{N1} can be assigned to the N $1s \rightarrow \sigma^*(e_g)$ transition, involving the MOs #54 and #55. The main peak E_{N2} corresponds to the N $1s \rightarrow \pi^*$ transitions, and involves the MOs #57-59; both N $1s$ transitions are indicated in the energy-level diagram of Figure 3.6. Comparing the nitrogen K-edge XA spectra (Figure 3.10) and the Co L-edge XA spectra (Figure 3.7), one finds that the σ^*-to-π^* band intensity ratio is considerably different for the two cases. The larger ratio in Figure 3.7 immediately suggests that the σ^* orbitals have dominant metal character, whereas the π^* orbitals have dominant ligand character indicated by the intensity ratio in Figure 3.10. This is confirmed by the orbital analysis presented in Figure 3.13(a). As can be seen, MOs #54 and #55 have 60% Co contribution but MOs #57-59 have only 20% metal character.

An important aspect related to the comparison between experimental and computed

XA spectra is whether there is any evidence for (water) solvent-specific effects. One experimental indication might be the aforementioned shift in the L_2 peak position when comparing XA spectra from aqueous solution with powder samples. Another observation is that the experimental XA spectra, both for the Co L-edge and the N K-edge, are best reproduced by calculations with the solvent effect included. As shown in Figure 3.16 for the Co XA spectra, the π^* band is shifted to a considerably lower excitation energy, in better agreement with experiment, when the solvent is taken into account. This is similarly true for the nitrogen spectra, where also better agreement between experiment and computation is obtained when the solvent effect is included; results are presented in Figure 3.17.

This section so far explored how the metal versus ligand (local) excitation reflects in the respective XA spectra. Experimentally, this information can be inferred in a straightforward manner, as described above, and on the theory side XA spectra calculations can be performed rather accurately.

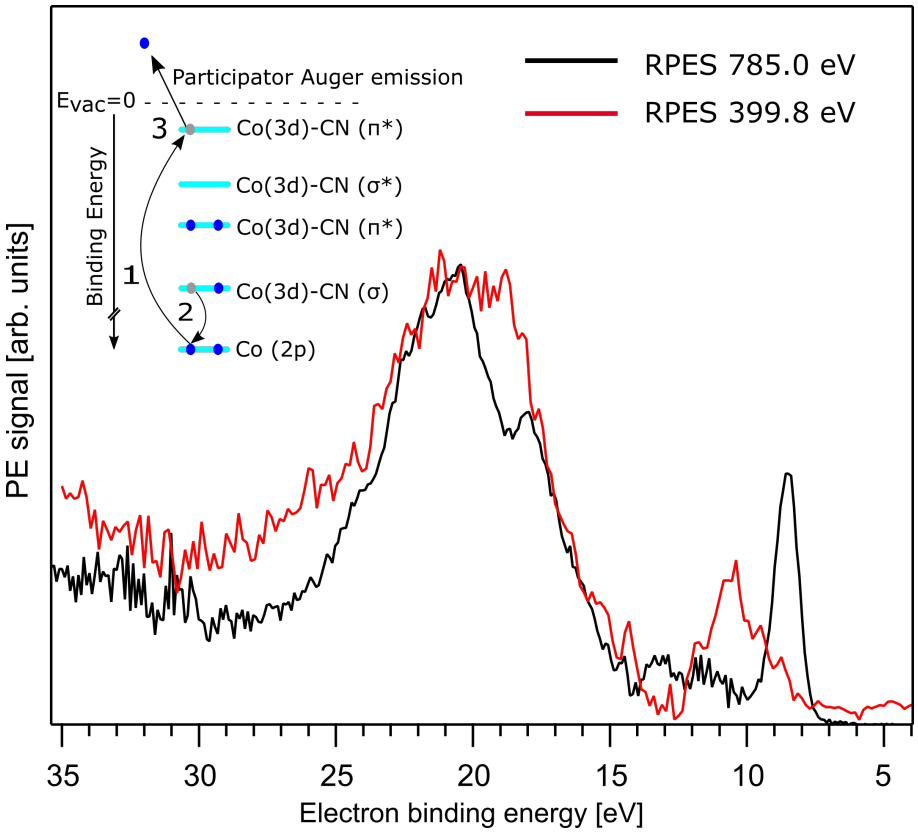

Figure 3.18: Resonant photoelectron spectra of aqueous $[Co(CN)_6]^{3-}$ at 785.0 eV (Co L-edge) and 399.8 eV, obtained by subtracting the off-resonant spectrum at 778 eV for Co and 398 eV for N (see text for details). The intensity of the Co RPE spectrum has been increased by a factor of 10 to match with the intensity of the N 1*s* K-edge) photon energy after subtraction of an off-resonant PE spectrum measured several RPE spectrum. The inset in the figure shows the Auger-emission channel responsible for the signal enhancement around 20.5 eV BE.

More detailed information is however contained in the RPE spectra which reveal the actual energies of overlapping ligand and metal orbitals through measured signal enhancements due to interfering electron emission channels. This has been recently demonstrated for $Fe^{3+/2+}$ and Ti^{3+} aqueous solutions [19, 30, 140]. For understanding the different local-excitation probes in this study, I compare the valence RPE spectra measured at the Co L-edge (already shown in Figure 3.2(c)) and at the nitrogen K-edge, this is presented in Figure 3.18.

Both spectra are presented in Figure 3.18, and from each an off-resonant (at few eV below the respective resonance; 785.0 eV for Co (E_2) and 399.8 eV for N (E_{N2})) PE spectrum has been subtracted in order to single out the signal enhancements at resonance. Both difference spectra are displayed to have the same peak heights at maximum signal, near 20 eV BE. Note that the absolute signal intensity for the N-edge-resonance spectrum is approximately ten times higher which is due to the larger cross section for N 1s absorption, and the six times larger number of nitrogen atoms compared to Co. Both spectra exhibit a rather similar broad electron emission in the approximately 13–25 eV BE range, with one noticeable difference being an intensity dip near 19.0 eV BE in the Co spectrum. Spectral differences are very pronounced however in the <15 eV BE region, where large relative intensity variations of the various peaks discussed in the previous sections are observed. Specifically, we detect larger (relative) intensities for peaks 8.5 eV (MOs #51-53) and 13.2 eV (MOs #31, #32) BE for the Co resonance, and indeed these emissions correspond to orbitals with mainly metal character (compare Figure 3.2(c)). On the other hand, larger signal near 10.0 eV BE is found for the N 1s excitation, and this is consistent with the above assignment, and the respective orbitals (MOs #42-44) have mainly ligand character. The large 15 – 25 eV electron emission band can be assigned to spectator Auger processes which involve 2-hole 1-particle final states. This can explain why one cannot assign specific orbitals derived from ground-state calculations for the transitions in this energy range, as spectator Auger transitions constitute a large departure from the electronic ground state. The situation is depicted for the deeper valence Co-CN(σ) to Co 2p spectator Auger refill in the inset of Figure 3.18. On the other hand, large signal intensity of the HOMO at 8.5 eV BE is attributed to participator Auger decay, in which case the kinetic energy of the Auger electron is the same as for the photoelectron at this resonant photon energy. An analogous explanation holds for the 10.0 eV peak, for the N 1s participator Auger decay. Note that the latter process is not depicted because the N 1s BE of $[Co(CN)_6]^{3-}$(aq) has not been detected in this study. The differences in spectral shape at energies above 25.0 eV in Figure 3.18 are attributed mainly to the different kinetic-energy dependent cross sections for the inelastically scattered photoelectrons in the solution.

3.1.10 Summary

RPE and RIXS spectra unambiguously reveal orbital mixing between metal center and CN ligands in the aqueous $[Co(CN)_6]^{3-}$ complex. Strong π-backbonding, i.e., back-donation

of the metal t_{2g} electrons into the empty π^* orbitals of the CN^- is observed from the σ^*-to-π^* and signal intensity ratios in the respective partial-yield XA spectra which vary dramatically for nitrogen versus cobalt core-level excitation. The assignment of these bands foots on electronic structure calculations based on DFT/ROCIS and TD-DFT. A major finding of the present study is that orbital mixing, and even the dominant orbital character, as well as the absolute energy of these orbitals can be accessed from the RPE spectra. This is due to the signal enhancements of peaks in the valence spectra, and these effects depend sensitively on whether the excitation is localized rather on the metal or on the ligand. This section not only shows that PEY and PFY XA spectra reveal important differences due to the particular electron relaxations but it also shows the need to invoke the respective RPE and RIXS spectra to interpret the derived XA spectra.

3.2 Electronic Structure of $[Co(bpy)_3]^{2+/3+}$ in Aqueous Solution

This section examines the electronic structure of $[Co(bpy)_3]^{2+}$ and $[Co(bpy)_3]^{3+}$ redox couples in aqueous solution using RIXS studies. As mentioned in the introduction Chapter, these molecules are of particular interest because they can assume two oxidation states, $[Co(bpy)_3]^{2+}$ and $[Co(bpy)_3]^{3+}$, serving as electron mediators in water splitting and in dye-sensitized solar cell systems [14, 18, 141]. First I describe the ground-state spin configurations of $[Co(bpy)_3]^{2+}$ and $[Co(bpy)_3]^{3+}$ molecules. The experimental approach is similar to the recent RIXS studies from Co (III) protoporphyrin IX chloride [142] and hemin [24] in solution, where a comprehensive interpretation of PFY-XA and RIXS spectra with the assistance of electronic structure calculations has been provided. It is followed by a detailed discussion on the PFY-XA spectra and RIXS spectra measured at the metal centers (Co^{2+} and Co^{3+}) and also at the ligand side (N K-edges). Furthermore, also analogous to the previous section, I have simulated the XA, XE/RIXS spectra for different spin configurations at the Co L-edge and N K-edge using TD-DFT and DFT/ROCIS methods provided by ORCA [92] software package. This allows for an assignment of the PFY-XA spectra. The presence of mixed spin character is further validated with the help of XA spectra calculations; more details are presented in the Section 3.2.5.

3.2.1 Ground State Spin Configurations of $[Co(bpy)_3]^{2+/3+}$

I have already introduced the concept of HS and LS octahedral complexes in Chapter 1. The CN^- ligand studied in the previous section is classified as a strong-field ligand leading to LS complexes. This is indeed reflected on the simple two peak structure observed at the metal L-edge XA spectrum. On the other hand, the ligands in the 'pyridine' group (bipyridine, phenanthroline and various polypyridyl ligands) compounds are well-known for exhibiting mixed spin configurations. This will be reflected on the metal L-edge XA spectrum, and is explored further in this section.

Co metal centers (Co^{2+} and Co^{3+}) studied in this section are octahedrally surrounded by chelating 2,2'-bipyridine ligands which can act as pi-acceptor and sigma-donor, thus forming a stable bond with the metal center [15]. Due to the large ligand size, steric constraints [36] will lead to some deviation from perfect octahedral symmetry, and this can affect the overall stability of the complex. Upon an external stimulus such as temperature, magnetic field or light the complexes can switch spin, commonly referred as spin cross-over [143–145]. This spin effect is due to the details of the valence electronic structure. The metal centers in the $[Co(bpy)_3]^{2+}$ and $[Co(bpy)_3]^{3+}$ complexes have d^7 and d^6 ground-state

Large parts of the text in this section is taken from the work *'Electronic Structure of Aqueous $[Co(bpy)_3]^{2+/3+}$ Electron Mediators'* by *Lalithambika* et al., which is published in the journal *Inorganic Chemistry*.

configurations with spin adjustability ΔS=±1 and ΔS=±2, respectively. It has been found that structural changes are stronger in the case of ΔS=±1 spin change resulting from the strong Jahn-Teller distortions, particularly for d^7 low-spin configuration [146].

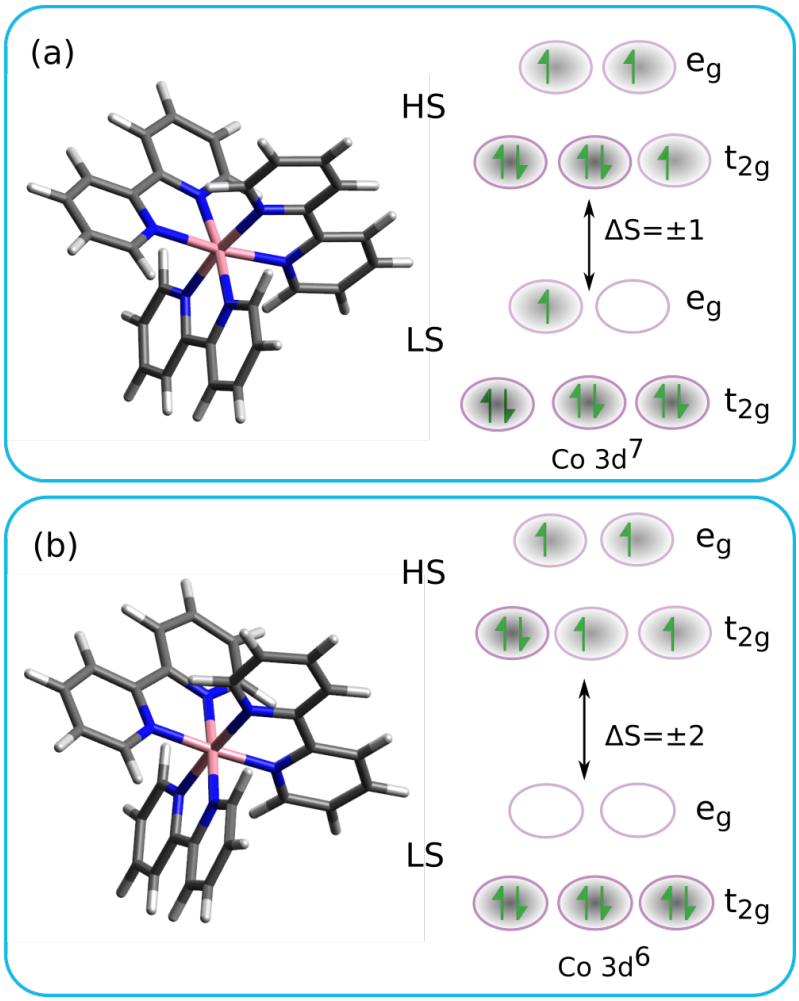

Figure 3.19: DFT (def2-TZVP(-f)/M06/CPCM water) optimized geometries of (a) $[Co(bpy)_3]^{2+}$ and $[Co(bpy)_3]^{3+}$. Pink, blue and light grey colors represents Co, N and H atoms respectively. Possible spin configurations in the valence 3d orbitals, both high spin (HS) and low spin (LS) are also shown.

Geometry optimized molecular structures for both complexes are presented exemplarily for the low spin (LS) case in Figure 3.19. For molecular geometry optimizations M06 [129] density functional along with def2-TZVP(-f) basis set [130] was used. The solvent effects were accounted for using the CPCM water model in ORCA [139]. The small deviations from octahedral symmetry are quantified by the bond angles and bond lengths shown in Table 3.1. Figure 3.19 also presents the electronic levels of $3d^6$ and $3d^7$ valence configurations for high spin (HS) and LS states. Judged from the Co–N distances and the respective bond angles (Table 3.1), we observe that LS (S=0) case of the $[Co(bpy)_3]^{3+}$ has the highest degree of local octahedral symmetry. Largest deviations from octahedral symmetry are observed for the LS (S=1/2) case of $[Co(bpy)_3]^{2+}$ and for the intermediate spin-state (IS,

S=1) case of the $[Co(bpy)_3]^{3+}$, not included in Figure 3.19. LS case of $[Co(bpy)_3]^{2+}$ has the valence occupation ${t_{2g}}^6\ {e_g}^1$, i.e., with an uneven occupation in the e_g level, causing strong Jahn-teller distortion. In the IS case of the $[Co(bpy)_3]^{3+}$ the ground-state configuration is ${t_{2g}}^5\ {e_g}^1$ with uneven occupations in both t_{2g} and e_g levels which also causes a significant distortion.

Bond length (Å)	$[Co(bpy)_3]^{2+}$		$[Co(bpy)_3]^{3+}$		
	LS	HS	LS	IS	HS
Co-N1	2.22	2.13	1.94	1.93	2.08
Co-N2	1.98	2.14	1.93	2.12	2.08
Co-N3	1.97	2.16	1.94	2.04	2.04
Co-N4	2.20	2.16	1.94	1.93	2.08
Co-N5	1.96	2.11	1.94	2.05	2.06
Co-N6	1.96	2.15	1.93	2.00	2.04
Bond angles					
N1-Co-N4	173.4°	167.4°	176.5°	175.0°	174.2°
N2-Co-N3	172.6°	172.4°	177.0°	176.0°	171.9°
N5-Co-N6	171.7°	168.5°	175.6°	168.9°	168.8°

Table 3.1: Bond lengths and bond angles of $[Co(bpy)_3]^{2+}$ and $[Co(bpy)_3]^{3+}$ complexes calculated for various possible spin configurations, low spin (LS), high spin (HS) and intermediate spin (IS), as obtained from DFT (def2-TZVP(-f)/M06/CPCM water) geometry optimizations.

3.2.2 Preparation of Sample Solutions and Experimental Details

In order to achieve a sufficiently high concentration of the hydrophobic Co tris-bipyridine complexes [147], salts of $[Co(II)(bpy)_3]Cl_2$ and $[Co(III)(bpy)_3]Cl_3$ were dissolved in water to achieve 100 mM and 200 mM concentrations, respectively. Salts were purchased from Dyenamo Chemicals (purity $> 95\%$). Aqueous solutions were prepared immediately prior to the RIXS measurements by dissolving the salts in Milli Q water [148], the prepared solutions were covered using aluminium foil for minimizing stray light induced chemical changes. The RIXS measurements at the Co L-edge and N K-edge for both samples were conducted using the LiXEdrom experimental station at the U49-2 PGM1 beamline. Liquid samples were contained in a flow-cell equipped with a 150 nm thick SiC membrane separating liquid from vacuum. A continuous circulation of the liquid inside the flow-cell is maintained using a syringe pump which minimizes sample damage upon X-ray irradiation. Detailed description of the experimental setup and the beamline can be found in Chapter 2.

3.2.3 Results from Partial Fluorescence Yield X-ray Absorption

Figure 3.20 presents the experimental Co L-edge (Figures 3.20(a), 3.20c) and N K-edge (Figures 3.20(b), 3.20(d)) PFY-XA spectra of 100 mM $[Co(bpy)_3]^{2+}$ and 200 mM $[Co(bpy)_3]^{3+}$ aqueous solutions. All spectra are obtained by integrating the individual RIXS spectra signal intensities as a function of excitation photon energy; the actual RIXS spectra will be discussed separately. First, I consider the Co XA spectra. In the $[Co(bpy)_3]^{2+}$ case (Figure 3.20(a)) the spectrum exhibits five noticeable features: a small pre-peak at 776.4 eV (label A_1), a split main peak at 778.4 eV (A_2) and 779.4 eV (A_3), a shoulder near 781.2 eV (A_4), and a broad featureless peak at 793.6 eV (A_5).

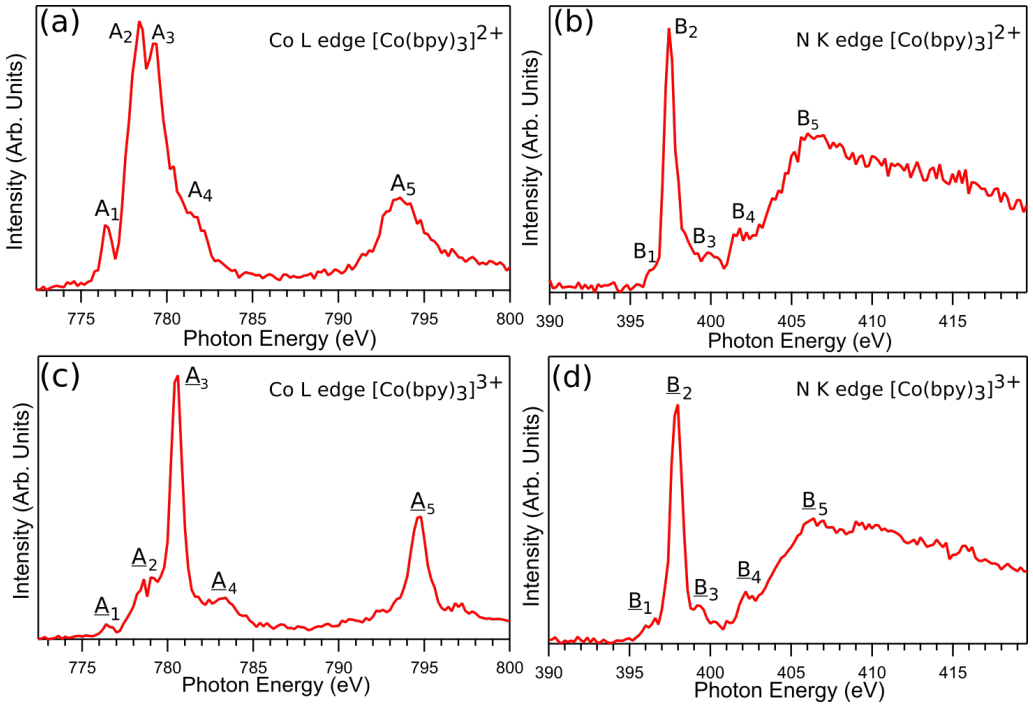

Figure 3.20: Experimental Co L-edge and N K-edge PFY-XA spectrum of 100 mM $[Co(bpy)_3]^{2+}$ (a), (b) and 200 mM $[Co(bpy)_3]^{3+}$ (c), (d), both dissolved in water. The prominent spectral features are marked A_1 to A_5, $\underline{A}_1$ to $\underline{A}_5$, B_1 to B_5, and $\underline{B}_1$ to $\underline{B}_5$.

In contrast, the Co XA spectrum from $[Co(bpy)_3]^{3+}$ (aq) (Figure 3.20(c)) exhibits a strong single main absorption peak at 780.6 eV (labeled $\underline{A}_3$). Two small absorption pre-peaks occur at 776.6 eV ($\underline{A}_1$) and 779.2 eV ($\underline{A}_2$), a small post-edge peak is seen at 783.4 eV ($\underline{A}_4$), and a stronger band is found at 794.8 eV (A_5). The latter is at slightly higher energy than A_5, but peak width being much smaller. A_5 and $\underline{A}_5$ correspond to the L_2-edge of the XA spectra. The striking differences between the Co $2p$ PFY-XA spectra from $[Co(bpy)_3]^{2+}$ (aq) and $[Co(bpy)_3]^{3+}$ (aq) can be assigned to spin mixing as well as to the various degrees of valence $3d$ splitting. In the $[Co(bpy)_3]^{2+}$ case, the possible spin states are S = 0.5, for LS, and 1.5 for HS. For the $[Co(bpy)_3]^{3+}$, S = 0 (LS), 1 (IS), 2 (HS), and yet S = 1 is the less probable intermediate spin state. For S = 1 to occur, the e_g level has to split strongly enough to overcome exchange interactions which requires a considerably large deviation

from the octahedral symmetry, but this is rarely encountered for the ground state [149]. A detailed quantitative interpretation of the spectra based on electronic-structure calculations will be provided in Section 3.2.5.

The measured N 1*s* PFY-XA spectra from $[Co(bpy)_3]^{2+}$ (aq) and $[Co(bpy)_3]^{3+}$ (aq) which again provide insight into the metal–ligand interaction, but now directly probing the ligand. Results are shown in Figures 3.20(b), 3.20(d). Unlike the Co 2*p* XA spectra, the N 1*s* XA spectra are very similar for the two oxidation states and hence there is negligibly small sensitivity to above-observed Co spin behavior; a very similar finding is also observed in the electronic structure calculations discussed in the following sections. In both cases, a strong narrow absorption band appears near ≈400 eV excitation energy, accompanied by two smaller post-peaks and a broad absorption band with maximum near 406 eV. For $[Co(bpy)_3]^{2+}$ (aq) (Figure 3.20(c)) the specific positions are: 396.5 eV (B_1), 397.4 eV (B_2), 400.0 eV (B_3), 401.8 eV (B_4), and 406.2 (B_5). Absorption bands for $[Co(bpy)_3]^{3+}$ (aq) (Figure 3.20(d)) are: 396.4 eV ($\underline{B}_1$), 398.0 eV ($\underline{B}_2$), 399.4 eV ($\underline{B}_3$), 402.2 eV ($\underline{B}_4$), and 406.2 eV ($\underline{B}_5$). B_2 and $\underline{B}_2$ bands are the N $1s \rightarrow \pi^*$ transitions characteristic for the bipyridine ring, specifically of the C=N π^* unoccupied orbitals [150]. The broad B_5 and $\underline{B}_5$ bands are attributed to the σ^* resonance [49]. Bands B_3, B_4, $\underline{B}_3$, $\underline{B}_4$ correspond to the $1s \rightarrow \pi^*$ higher-order orbital transitions, possibly exhibiting some metal character. In contrast, the small B_1, $\underline{B}_1$ bands are argued to exhibit considerable metal character as we show in Section 3.2.5. Notably, a similar feature has been reported for lanthanide quinoline molecule [151], in a case where cobalt is not the central metal, where this feature was argued to be due to Co-N bonding states. A full spectral analysis based on computations will be presented in Section 3.2.5.

3.2.4 Results from RIXS and XE Experiments

Although the XA spectra presented in Figure 3.20 can be considered characteristic fingerprints of each molecule, it is equally instructive to analyze the underlying RIXS spectra from which the XA spectra are obtained. First, I describe the Co 2*p* data from the two solutions. The full RIXS maps - presenting signal intensities on the excitation photon energy versus emitted photon energy grid - are shown in Figure 3.21(a) for $[Co(bpy)_3]^{2+}$ (aq), and in Figure 3.21(c) for $[Co(bpy)_3]^{3+}$ (aq). Few selected RIXS spectra, which are horizontal cuts through Figures 3.21(a), 3.21(c), from both solutions are presented in Figures 3.21(b), 3.21(d), respectively.

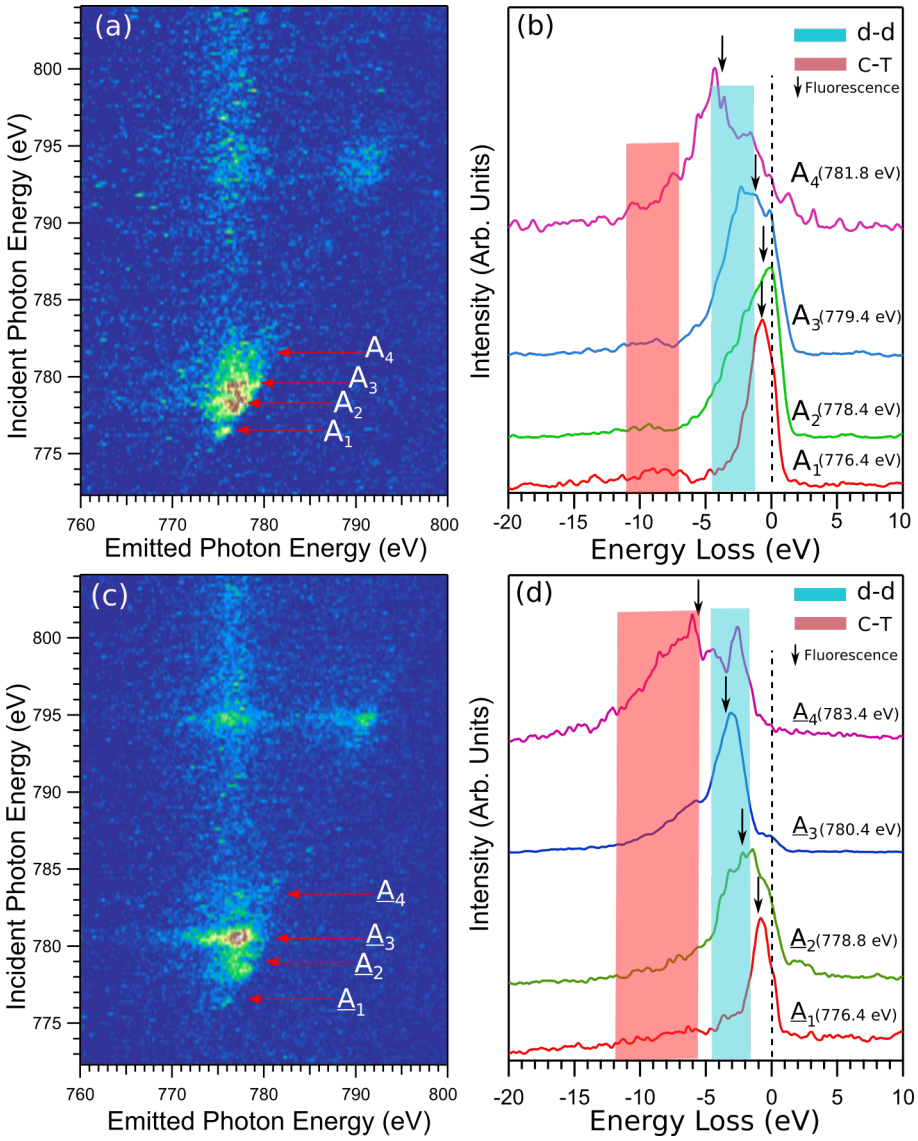

Figure 3.21: (a) Co L-edge RIXS map and (b) selected RIXS spectra from 100 mM $[Co(bpy)_3]^{2+}$ aqueous solution. (c) RIXS map and (d) RIXS spectra from 200 mM aqueous $[Co(bpy)_3]^{3+}$ solution. Individual RIXS spectra in (b) and (d) have been collected for longer time. RIXS spectra, (b) and (d), are presented on the energy-loss axis; in this presentation the fluorescence features do not appear as exhibiting constant energy (marked by arrows). Intensities are shown such that the respective maxima have the same peak heights for each tier.

In order to obtain reasonably good signal statistics, the individual RIXS spectra were separately measured for longer acquisition times (approximately 30 min) as compared to the fast sweeps (approximately 1 min) that leads to the maps presented in Figures 3.21(a) and 3.21(c). Note that intensities of the RIXS spectra (Figures 3.21(b), 3.21(d)) are normalized to maximum intensity for better visualization of spectral features. The RIXS maps (Figures 3.21(a), 3.21(c)) are found to be fairly similar for the two species but few important differences should be pointed out. In both cases a constant-energy emission in the 765–

785 eV region is observed for excitation energies from 775–782 eV. This is the $3d \rightarrow 2p$ fluorescence channel. The band maxima correspond to the absorption bands A_1 to A_4 and $\underline{A}_1$ to $\underline{A}_4$ (of Figure 3.20(a) and 3.20(b)), respectively. Several weaker photon signals, although barely noticeable in the RIXS-map presentation, identify the resonating energy-loss features, known as Raman emission channels or local excitations [59, 152]. These include the *d-d* excitations and CT excitations of the Raman scattering. Main differences between the two RIXS maps is the larger signal from the Raman channels, responsible for the low-energy tail, most clearly seen at the $\underline{A}_3$ excitation in Figure 3.21(c). For a more quantitative analysis of the actual RIXS features, which also includes assignment of the elastic peak (the recombination due to elastic transitions to the ground state), one needs to consider the actual RIXS spectra (Figures 3.21(b), 3.21(d)) in order quantify these contributions. These RIXS spectra are presented on the energy-loss scale where zero energy corresponds to the elastic peak (black dashed line). Such representation permits an effortless way of displaying final state effects (Raman features). The Raman features occur at constant energy losses with respect to the elastic peak. Hence, aforementioned *d-d* and CT excitations occur at the same loss energy, respectively. The former emissions appear within the blue-shaded energy region (at approximately ∼1–4 eV energy loss), and the latter contribute within the red-shaded region (between ∼7–11 eV in Co^{2+} and ∼5.5–12 eV in Co^{3+} systems) marked in Figure 3.21(b), 3.21(d). The larger width of the CT band in Co^{3+} (Figure 3.21(d)) results from a larger number of probable transitions compared to the Co^{2+} case. This is due to the higher charge state of the Co^{3+} complex causing a stronger Coulomb attraction between the metal center and the ligands than for the Co^{2+} case. Hence, larger orbital overlap will lead to stronger metal–ligand bond which manifests in more intense CT transitions. This interpretation would be in agreement with theoretical UV-Vis studies on $[Co(bpy)_3]^{2+/3+}$ in acetonitrile and in the gas phase [153], where the larger width has been attributed to ligand-to-metal electron transfer. Arrows in Figures 3.21(b), 3.21(d) mark the positions of the fluorescence ($3d \rightarrow 2p$ channel) which are the features that move with the excitation energy (compare Figures 3.21(a), 3.21(c)).

The RIXS spectrum from the Co^{2+} complex measured at the A_1 (776.4 eV; red spectrum) resonance, Figure 3.21(b), shows the main emission at ∼1 eV. This band exhibits a weak shoulder at ∼2 eV which is the *d-d* excitation (within blue shade). In addition, a small band is seen at ∼8.4 eV loss energy (red shade) which is due to CT excitations. Upon increasing the excitation energy to A_2 (778.4 eV; green spectrum) the spectrum exhibits a broad structured asymmetric tail between ∼0.9 and 3.4 eV, again identifying the *d-d* transitions. As for A_1 excitation, a small CT band occurs although at the slightly larger loss energy of ∼9 eV. Excitation at A_3 (779.4 eV; blue spectrum) results in a similarly asymmetric peak. However, the elastic peak (dashed line) is now more separated from the *d-d* emission occurring between ∼1 and 4 eV. The small CT peak is seen to appear at ∼9.4 eV. Excitation A_4 (781.8 eV; magenta spectrum), i.e., above the main resonances, exhibits the same principle energy-loss behavior although the overall spectral shape appears to be

quite different, characterized by an increased fluorescence emission near 4 eV relative to the *d-d* emission at ∼2.5 eV, and by a tail structure which is due to CT excitations, at ∼9 eV.

For the Co^{3+} system (Figure 3.21(d)), resonant excitation at $\underline{A}_1$ (776.4 eV; red spectrum) results in a spectrum with maximum intensity centered at ∼1 eV, resembling the one at A_1 excitation of Co^{2+}, except for the CT band (red shade) now extending to higher loss energies. Also, the *d-d* feature at ∼2 eV (blue shade) is less prominent compared to the Co^{2+} system. The spectrum measured at $\underline{A}_2$ (778.8 eV) excitation exhibits pronounced *d-d* loss signal between ∼1.5 and 4.5 eV. CT bands are responsible for the long low-intensity tail (within the red shade). At excitation $\underline{A}_3$ (780.4 eV; blue spectrum) the *d-d* signal intensity, centered at ∼3 eV, is seen to increase relatively to the other bands. Also, the CT signal contribution, now observed between ∼6 and 9 eV, is found to increase in intensity. Finally, the RIXS spectrum measured at excitation $\underline{A}_4$ (783.4 eV; magenta trace) exhibits a *d-d* double peak, at 2.8 and 4.5 eV. A strong CT feature is observed in the 5 – 12 eV loss region. Figure 3.21 can be summarized with the following conclusions and comments:
(i) The experimental assignment of spectral regions to *d-d* and CT transitions is rather tentative (based on previous results from similar systems [142]), and there is no clear-cut boundary between these contributions. This requires theoretical calculations, discussion is given below.
(ii) One expects that both cobalt complexes studied here adopt two different spin states which correspond to different valence electron occupations (compare Figure 3.19). This will be indeed corroborated by the following computations.
(iii) The lower-energy tails of the individual RIXS spectra gain in intensity as the excitation energy increases which can be associated with the opening of favorable electron delocalization channels (especially intramolecular electron transfer to the ligands) when populating higher-lying *d* states.
(iv) Larger signal intensities of the CT tails observed for Co^{3+} species as compared to their Co^{2+} counterparts would be in accordance with the higher charge on Co^{3+}, and aforementioned resulting stronger metal-ligand orbital mixing.
(v) The *d-d* band double-peak structure observed at $\underline{A}_4$ excitation can be attributed to contributions from emerging fluorescence features with the energy-loss features (see Figure 3.21(c)).

Before examining the respective N 1*s* RIXS spectra a short comparison of the above Co L-edge RIXS spectra with previous studies on Co (III) protoporphyrin IX chloride (Co L-edge) and hemin (Fe L-edge) in solution is beneficial [24, 142]. In both earlier studies, the RIXS spectra are dominated by constant-energy emission (fluorescence) features, and contributions from Raman-type emission are minor. Possibly, this difference is due to the closed-shell valence-structure character. It would thus appear that in the case of open-shell structure systems (where the unpaired electrons are localized on the metal center) in the present study, at least for $[Co(bpy)_3]^{2+}$ where both possible spin states are expected to

be open-shell, the energy-dispersive channel becomes quite favorable. Arguably, for the $[Co(bpy)_3]^{3+}$ case, this may imply that the spin state is not purely LS (zero spin) but rather mixed with a HS component. This is indeed in accordance with the spin-state analysis to be presented below. It is not clear what exactly causes the increased probability of the Raman channel, an effect that seems to not have been explicitly addressed in the literature. Note that for the same open-shell system N 1*s* (ligand) core-excitation exhibit only minor Raman-type features. Another noteworthy observation is the relatively strong CT spectral contribution for the cobalt bipyridines as compared to cobalt protoporphyrin IX. This is indicative of strong metal–ligand orbital mixing.

The N K-edge RIXS planes and selected RIXS spectra are shown in Figure 3.22. The former data are presented in Figures 3.22(a) and 3.22(c) for the two Co complexes, respectively, and the individual spectra are shown in Figures 3.22(b) and 3.22(d). Unlike in the case of the Co L-edge RIXS spectra, the RIXS spectra in Figures 3.22(b), 3.22(d) are displayed on the same energy scale as the RIXS maps, i.e., as a function of the actual emission energy. The RIXS maps from $[Co(bpy)_3]^{2+}$ and $[Co(bpy)_3]^{3+}$ are seen to be very similar in agreement with the expectation that the ligand is rather insensitive to the metal spin state. Both maps exhibit two main emissions (fluorescence) at the constant energies 390 and 393 eV for excitation photon energies larger than 400 eV. In addition, there is a single sharp absorption at 397 eV excitation energy, and the emission is slightly red-shifted as indicated by the red-dashed lines in Figure 3.22(a) and 3.22(c); this is seen between excitation energies B_2 (397.4 eV) and B_4 (401.8 eV). Unlike the Co 2*p* spectra the N 1*s* RIXS spectra exhibit minor Raman-type features; this is the reason why Figures 3.22(b) and 3.22(d) are not presented as energy losses. Analogous to the analysis of the Co L-edge RIXS data, here also several selected RIXS spectra are considered at the resonance energies B_2 (397.4 eV), B_4 (401.8 eV), B_5 (406.4 eV) in Figure 3.22(b), and $\underline{B}_2$ (398.0 eV), $\underline{B}_4$ (402.4 eV), $\underline{B}_5$ (406.2 eV) in Figure 3.22(d), this is more suitable to detail spectral differences. Each spectrum has been acquired over longer time, as explained before, and intensities are displayed to yield same heights at maximum. Note that the resonance energies considered in Figure 3.22 are the same ones already mentioned in Figure 3.20. In addition, two non-resonant XE spectra obtained at 420.0 eV for Co^{2+} (Figure 3.22b) and 410.0 eV for Co^{3+} are presented. Arrows in Figures 3.22(b), 3.22(d) mark the position of the elastic peaks (corresponding to direct filling of the N 1s core hole) [154]. As already expected from the RIXS map of $[Co(bpy)_3]^{2+}$ the RIXS spectra are almost the same for the energies B_4 to B_5, exhibiting the two emissions at 390.0 and 393.0 eV, and the spectral energy shift of the emission band (at 389.0 and 391.4 eV) for B_2 excitation is now clearly visible. A peak at 393.3 eV energy for B_2 excitation is also observed, which moves to 394.5 eV for subsequent excitations from B_4, B_5 and at 420.0 eV (blue dotted line in Figure 3.22(b)), a similar pattern can be observed in Co^{3+} case, but is less distinct and only appears as a weak shoulder (blue dotted line in Figure 3.22(d)). RIXS spectra of $[Co(bpy)_3]^{3+}$ in Figure 3.22(d) exhibit broader spectral features compared to $[Co(bpy)_3]^{2+}$.

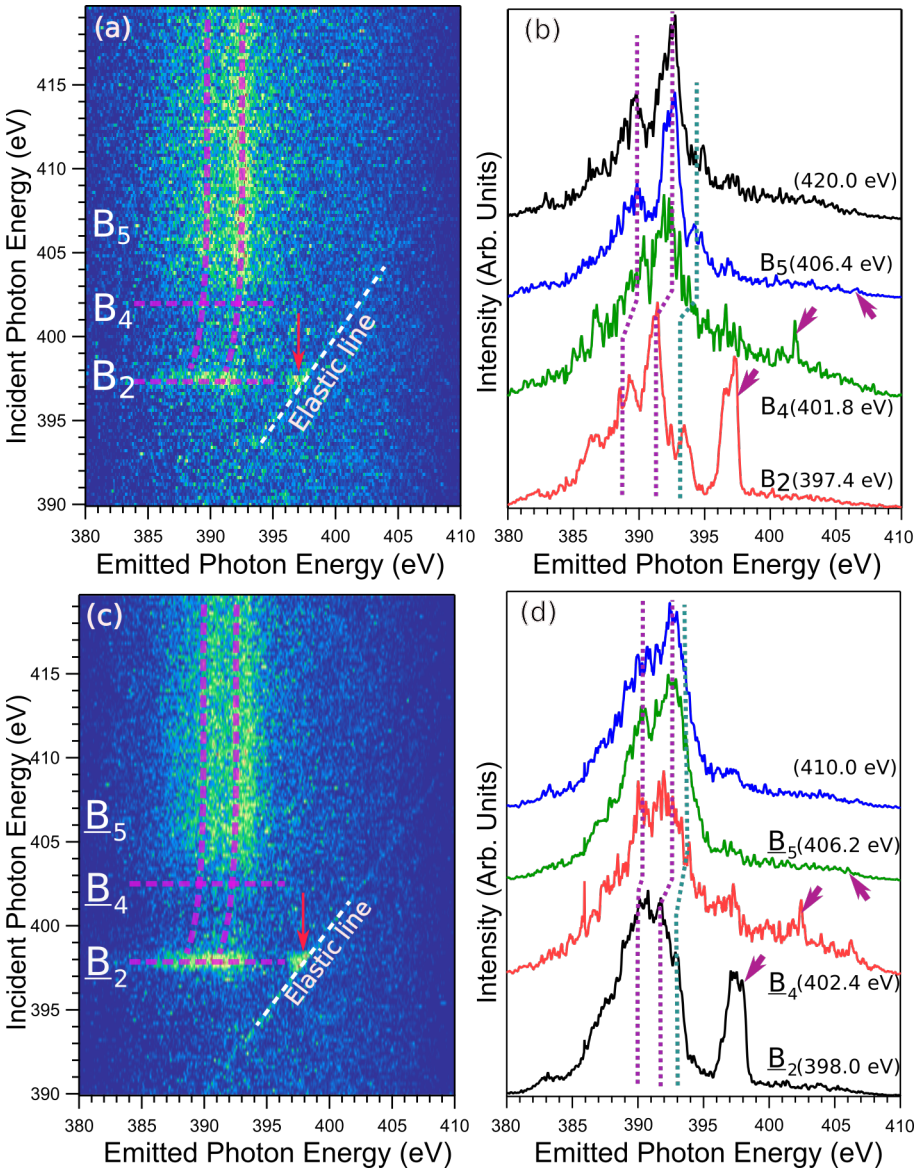

Figure 3.22: (a) and (b) present the N K-edge RIXS map and RIXS spectra from 100 mM $[Co(bpy)_3]^{2+}$ aqueous solution. (c) and (d) show the RIXS map and RIXS spectra from 200 mM aqueous $[Co(bpy)_3]^{3+}$ solution. As in Figure 3.21, RIXS spectra were collected for longer times, and intensities are displayed to yield same heights at maximum. The slanted dotted lines in the RIXS maps highlight the position of the elastic peaks; they are marked with arrows in line spectra.

Most notable is the double-peak structure occurring at emission energies 390.0 eV and 391.7 eV for the resonant excitation at $\underline{B}_2$ (398.0 eV). Excitation at $\underline{B}_4$ (402.4 eV) shifts the peak to 390.2 eV and 393.0 eV, exhibiting the similar resonance behavior as B_4 excitation in $[Co(bpy)_3]^{2+}$. Excitation at $\underline{B}_5$ (406.2 eV) results in a spectrum which is very similar to the off-resonant XE spectra measured at 410.0 eV. To both the high and the low-energy side all RIXS spectra exhibit long tails. The small signal at slightly lower energies of the elastic peaks (red arrows in RIXS maps) are due to vibronic excitations [128, 155], which are however not resolved here. The two intense emission channels (pink lines) can

be attributed to emissions from ligand $2p \rightarrow$N $1s$ transitions. Low-energy tail signal, below 388.0 eV, can be assigned to ligand p→N $1s$ transitions and s→N 1s transitions [156]; these assignments are supported by XE spectra calculations. The experimental XE spectra for both the complexes were well reproduced in XE calculations, see Figure 3.23.

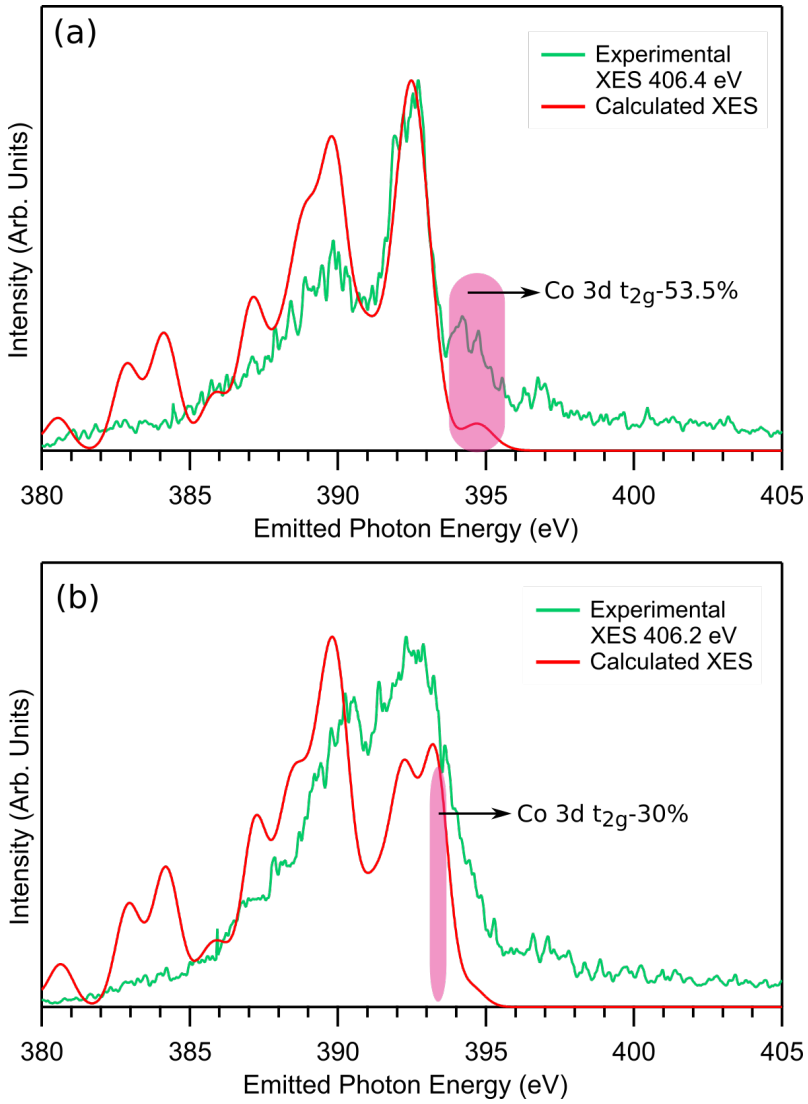

Figure 3.23: Comparison of N K-edge non-resonant XE spectra of $[Co(bpy)_3]^{2+}$ panel (a) and $[Co(bpy)_3]^{3+}$ panel (b) with their calculated counterparts. The calculated XE spectra are shifted by 9.6 eV and 9.8 eV in panel (a) and (b) for matching with experimental spectra. Shaded areas in pink mark transitions originating with significant Co $3d$ character.

These calculations also help in identifying the high-energy peaks marked by blue dotted lines in Figure 3.22. computations suggest that the high-energy section of the emission originates from hybridized Co 3d (t_{2g})-ligand $2p$ orbitals, with ∼53% metal character for Co^{2+} and ∼30% for Co^{3+} as shown in Figure 3.23(a) and 3.23(b).

3.2.5 Results from Electronic Structure Calculations

I used DFT/ROCIS and TD-DFT level of theories to generate the Co L-edge and N K-edge XA spectra using first principles calculations for a detailed interpretation experimental PFY-XA spectra. Transition energies and moments for the Co L-edge were calculated with DFT/ROCIS using the same basis set and B3LYP [131, 132] functional. For the N K-edge, TD-DFT method was employed, again using the same functional and basis set. For DFT/ROCIS calculations the B3LYP functional with the parameters c_1=0.18, c_2=0.20, and c_3=0.40 [93]. Numerical integrations during the DFT calculations were performed on a dense grid (ORCA grid 4). L-edge and K-edge absorption spectra were obtained by applying a 0.8 eV Gaussian-type broadening on each transition moment respectively. In all calculations, the relativistic effects were taken into account using ZORA [98]. Main intent is to trace the origin of peaks observed in Figure 3.20. This approach also enables to calculate XA spectra with varying constraints such as calculation for different spin states, inclusion of spin orbit coupling and solvent effect. Note that DFT/ROCIS is capable to account for $2p$–$3d$ and $3d$–$3d$ multiplet structure and incorporation of spin orbit coupling by configuration interaction. Both Co L-edge and N K-edge XA spectra for different oxidation states were calculated with different spin configurations (LS and HS, also an intermediate spin (IS) for oxidation state +3), shown in Figures 3.24 and 3.25.

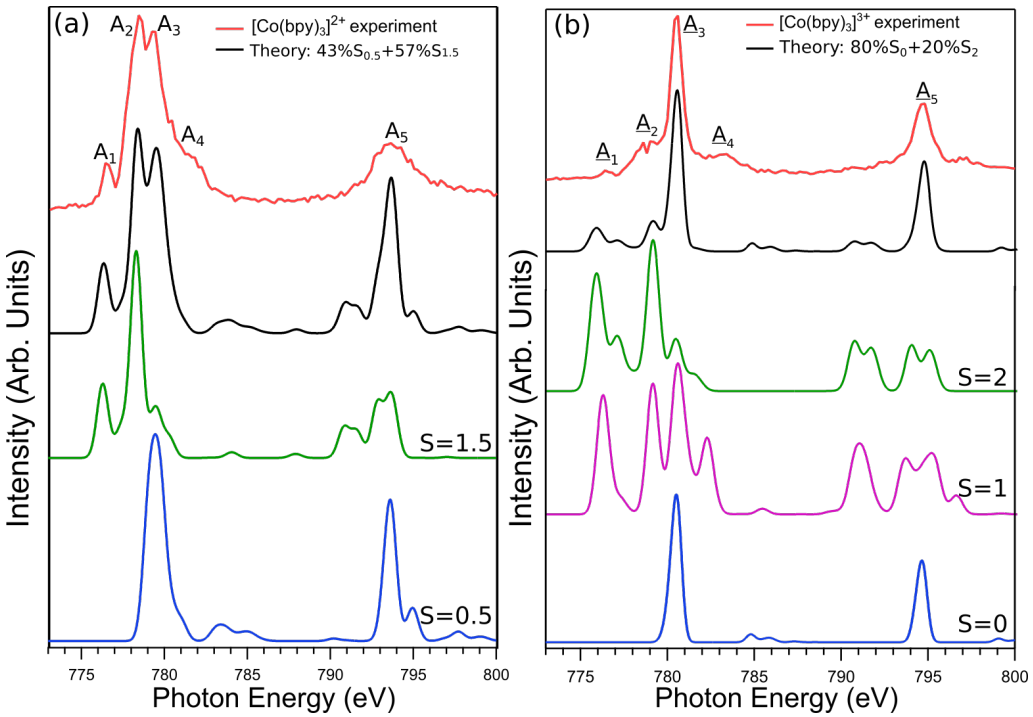

Figure 3.24: Computed Co L-edge spectra of $[Co(bpy)_3]^{2+}$ and $[Co(bpy)_3]^{3+}$ complexes with different possible spin configurations. Aqueous environment is implemented by enabling CPCM keyword. Experimental spectra are shown in red.

In Figure 3.26, the doubly occupied molecular orbital (DOMO) and singly occupied molecular orbital (SOMO) type candidate orbitals obtained from single point DFT calcu-

lations for resonant/non-resonant emissions are presented. These orbitals exhibit Co 3*d* character with varying degrees, resulting with crucial metal–ligand orbital mixing. The valence SOMO/unoccupied orbitals are also generated following the same method, shown in Figure 3.27; these visual representations help in easily identifying the character of valence orbitals involved in the absorption processes. Note that the orbitals displayed in Figures 3.26 and 3.27, selected using Löwdin population analysis according to their cobalt content, correspond to the highest absorption/emission probabilities.

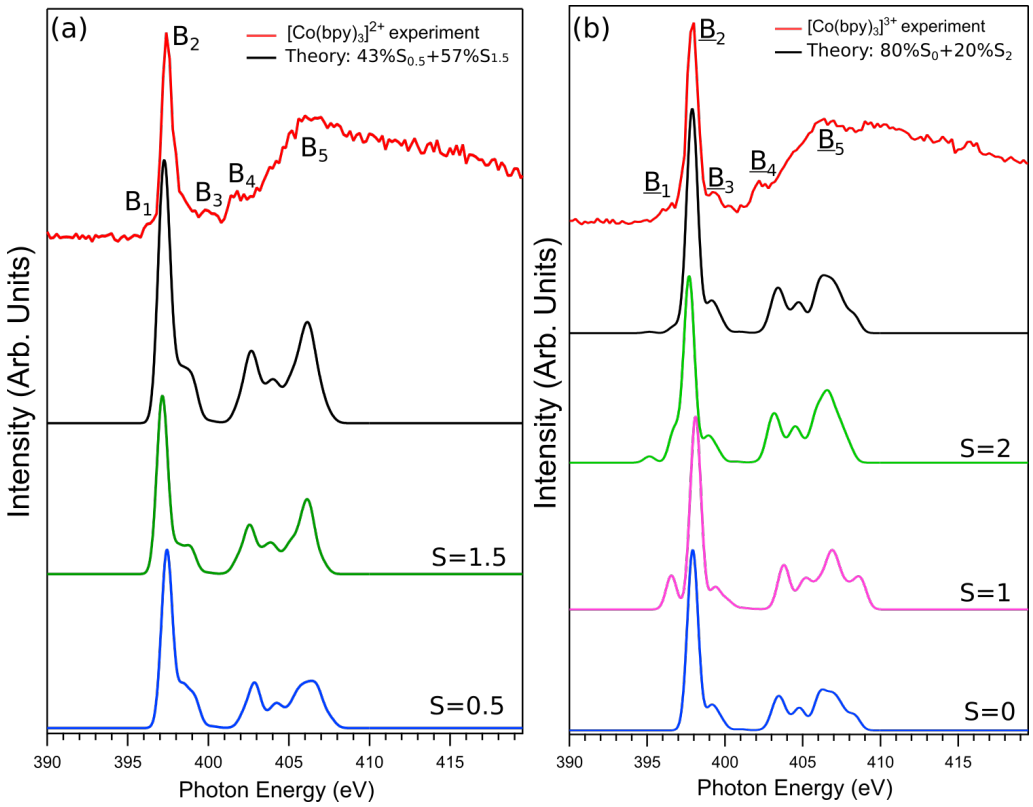

Figure 3.25: Computed N K-edge spectra from $[Co(bpy)_3]^{2+}$ and $[Co(bpy)_3]^{3+}$ complexes with different spin configurations. The summed spectra are shown in black. Labels and color codes are analogous to Figure 3.24. Also, the mixed-state spectrum (in black) has been obtained with the same spectral ratios as in Figure 3.24.

An attempt is made to calculate the RIXS planes of LS configurations of $[Co(bpy)_3]^{2+}$ and $[Co(bpy)_3]^{3+}$ using the DFT/ROCIS method. Although the results, presented in Figure 3.28 in the appendix 3.2.7, do reasonably well reproduce a pre-peak in Co^{2+} and an extended Raman features in Co^{3+} across the resonance, note that due to the high computational demand, all the MOs which would play a role in the core-hole deexcitation could not be included, consequently, the complete range of RIXS spectra including both *d*-*d* and CT transitions cannot be obtained.

Figure 3.24 presents the comparison of different computed Co L-edge XA spectra of $[Co(bpy)_3]^{2+}$ (Figure 3.24(a)) and $[Co(bpy)_3]^{3+}$ (Figure 3.24(b)). In each figure the top tier shows the experimental spectra (red). Then, in the left panel, from top to bottom,

computed XA spectra are presented; for mixed spin-state (black), S = 1.5 (green), and S = 0.5 (blue). For the Co^{3+} case computed XA spectra for S = 2 (green), S = 1 (purple), and S = 0 (blue) are shown. Note that all the calculated XA spectra are normalized according to their highest intensity peaks, and shifted equally to higher energies (12.17 eV for $[Co(bpy)_3]^{2+}$ and 10.7 eV for $[Co(bpy)_3]^{3+}$) in order to match the energies of the experimental spectrum; this is a common procedure to bypass DFT issues with absolute transition energies [93]. It is immediately seen that none of the pure-spin-state calculations matches the experimental spectra. However, rather good agreement is obtained for mixed spin states. For $[Co(bpy)_3]^{2+}$ case a close match to the experimental spectrum (except for the L_2-edge) is obtained when summing up 43% of low spin (S = 0.5) and 57% of high spin (S = 1.5) computed spectra (the relative intensities of the computed spectra are preserved during the summation). The situation is similar for $[Co(bpy)_3]^{3+}$ where the experimental spectrum is reasonably well reproduced by summing up 80% of low-spin (S = 0) and 20% of high-spin (S = 2) computed spectra. It is noted that in the case of $[Co(bpy)_3]^{3+}$ the highly improbable state S=1 has not been considered in the analysis. Based on the analysis it can be concluded that the electronic ground state is in a single quantum chemical state consisting of mixed spin configurations [44].

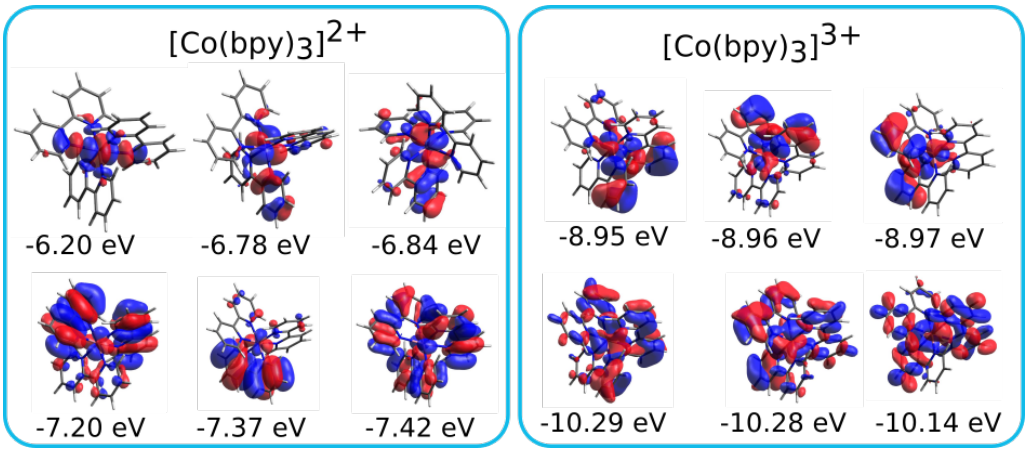

Figure 3.26: Candidate orbitals for RIXS/XES with significant Co 3*d* and ligand 2*p* contributions obtained from DFT calculations employing B3LYP functional with def2-TZVP(-f) basis set for $[Co(bpy)_3]^{2+}$ and $[Co(bpy)_3]^{3+}$ in LS configuration.

Analogous results are shown for the experimental and computed N 1*s* XA spectra for the two cobalt complexes in Figure 3.25. Reasonable matches with experimental spectra for both $[Co(bpy)_3]^{2+}$ and $[Co(bpy)_3]^{3+}$ are found for the computed spectra when the same spin components are being summed according to the above scheme. As pointed out in the experimental PFY-XAS section of nitrogen K-edge, the experimental spectra for both species are nearly the same. The following observations are arrived for the computed spectra: neither the oxidation nor the spin states create significant differences. This insensitivity of the ligand nitrogen atoms towards the oxidation and the spin-state can be interpreted by considering that the molecular charge and spin governed by the Co-3*d*

originated orbitals are significantly localized on the central metal atom.

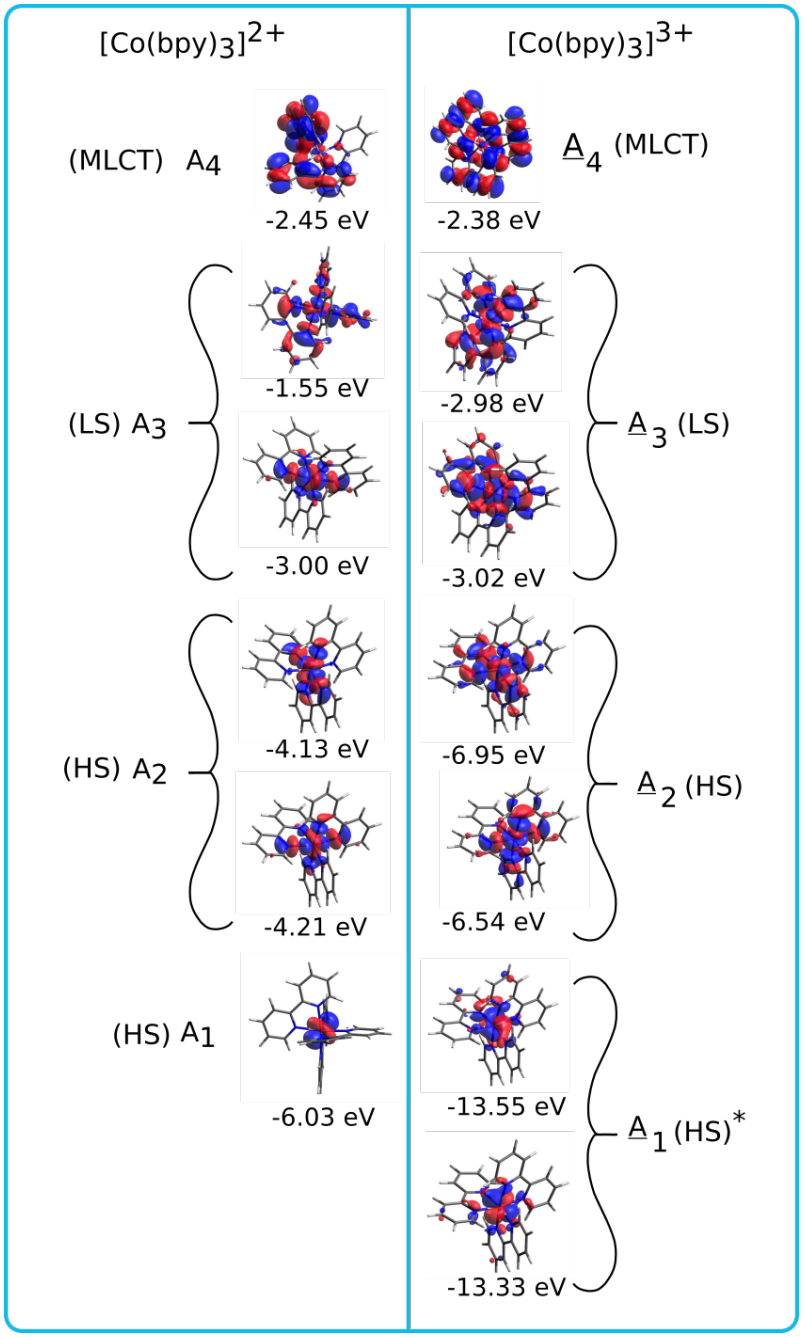

Figure 3.27: Unoccupied/singly occupied molecular orbital diagrams obtained for DFT calculations using B3LYP functional with def2-TZVP(-f) basis set for $[Co(bpy)_3]^{2+}$ and $[Co(bpy)_3]^{3+}$. MOs marked A_1-A_4 and $\underline{A}_1$-$\underline{A}_4$ can be associated to the transitions corresponding to the Figure 3.24. *MOs obtained from ROKS calculations where an unusual jump in energy is observed. This particular violation of the Aufbau principle is detailed in a previous study on open-shell hemin [24, 157, 158].

The assignments of XA features in Figures 3.24 and 3.25 are arrived with the help of calculations. These assignments are restricted to the most important transitions relevant

for HS and LS configurations.

Co L-edges of $[Co(bpy)_3]^{2+}$ and $[Co(bpy)_3]^{3+}$

According to the computational model absorption bands A_1 and A_2 originate from the HS state, and A_3 from the LS state. The pre-edge feature A_1 is associated with the $2p \rightarrow 3d$ (t_{2g}) transition (see Figure 3.27 for a visual representation of the associated orbitals). This is the transition to the SOMO of the molecule in HS configuration. The most intense peak A_2 is associated with the $2p \rightarrow 3d$ (e_g) transitions; the $3d$ (e_g) orbitals are singly occupied in the HS ground state. Absorption A_3 arises mainly from the LS state of the Co^{2+} (blue spectrum in Figure 3.24(a)). In LS configuration this transition is associated with the $2p \rightarrow 3d$ (e_g). The small band A_4, also reproduced in the same computed LS spectrum, can be assigned to the metal-to-ligand charge transfer (MLCT) transitions . This is consistent with the delocalized character of the respective associated orbital in Figure 3.27 (top), where we also show e_g and t_{2g} character for the other unoccupied and singly occupied MOs.

For $[Co(bpy)_3]^{3+}$ the strong $\underline{A}_3$ band originates mainly from the LS configuration, corresponding to $2p \rightarrow 3d$ (e_g) transitions. The small low-energy features $\underline{A}_1$ and $\underline{A}_2$ are absent in the calculated LS spectrum, and are suggested to only occur for the HS state of the complex. Indeed, the calculated spectrum for the HS configuration (green spectrum in Figure 3.24(b)) reproduces absorption peaks $\underline{A}_1$ and $\underline{A}_2$. They can be attributed to $2p \rightarrow 3d$ t_{2g}, e_g transitions. The HS calculation also reproduces the main feature $\underline{A}_3$ with a weak intensity. $\underline{A}_4$ is the MLCT transition, already mentioned for the Co^{2+} complex.

N K-edges of $[Co(bpy)_3]^{2+}$ and $[Co(bpy)_3]^{3+}$

Nitrogen $1s$ absorptions B_1 to B_4 and $\underline{B}_1$ to $\underline{B}_4$ are dominated by the π-electron system of 2,2'-bipyridine, leading to $1s \rightarrow \pi^*$ transitions. The broad features B_5 and $\underline{B}_5$ are assigned to transitions into σ^* (anti-bonding) types MOs [49].

Calculations for LS (S = 0.5) show that the characteristic π^* resonance at B_2 is due to the promotion of the N $1s$ electron to the SOMO of the molecule; this orbital is depicted as LS-A_3 in Figure 3.27. In molecules with a pyridine ring structure, the intense π^* peak arises from C=N atoms [150]. The Löwdin analysis for both spin states suggests that the absorbing orbital is formed from the hybridized Co (e_g) and N $2p$ orbitals with a Co $3d$ type orbital contribution of approximately 3%.

The small absorption feature $\underline{B}_1$ (396.4 eV) arises from the HS component only; the LS XA calculation (blue) does not reproduce the pre-edge feature. This feature is a result of N $1s$ to the lowest SOMO, with main contribution from Co $3d$ e_g ($\approx 60\%$)orbitals. Both LS and HS XA calculations reproduce the intense peak $\underline{B}_2$. Both LS and HS XAS calculations identify the B_2 feature as occurring from the N 1s to ligand dominated orbitals with $\approx$ 95% contributions by N and C atoms.

3.2.6 Summary

The combined experimental and computational (soft-X-ray) RIXS study at the Co 2*p* and the N 1*s* edges from the cobalt electron-mediator complexes, $[Co(bpy)_3]^{2+}$ and $[Co(bpy)_3]^{3+}$, enables a good quantification of the mixed metal–ligand valence orbitals that are crucial for electron delocalization and thus intramolecular charge transfer. The DFT/ROCIS calculations of Co 2*p* XA spectra for different spin states are capable to well reproduce experimental spectra; the latter are obtained from the signal integration of the RIXS spectra. In particular, one can quantify the relative metal-to-ligand character of the most relevant orbitals in the RIXS process by linear combinations of calculated XA spectra for different pure-spin states. The observed stronger low-spin character (80% versus 20% high spin) for the $[Co(bpy)_3]^{3+}$ complex, compared to $[Co(bpy)_3]^{2+}$ (43% low-spin, 57% high-spin), can be understood in terms of the relative stability of a low spin $3d^6$ configuration. An important aspect of the present study is that analyzing the electronic structure explicitly involves the detailed interpretation of the actual RIXS spectra. This provides additional information on the specific molecular states involved, fully based on experiment. The larger signal intensities of the CT tails observed for Co^{3+} species as compared to their Co^{2+} counterparts are in accordance with the higher charge on Co^{3+}, which results with a stronger metal-ligand orbital mixing. I also quantitatively interpreted the measured N K-edge XA spectra assisted by theoretical calculations. As expected for the large bipyridine ligands, the differences in metal charge and spin state are not reflected in the respective ligand-based excitations. Both experimental and computed spectra (for the various spin states) are almost the same for the two Co complexes.

In summary, this section described the significant potential of RIXS, specifically of RIXS-inferred XA spectra and actual RIXS spectra, for the investigation of TM complexes (metal center) with acute sensitivity to spin states. This section also discussed challenges in the computations, exemplified here by the limitations of TD-DFT calculations to reproduce all prominent details of the RIXS maps. The DFT/ROCIS based XA calculations successfully explained the experimental PFY-XA spectra in this section as well as in the previous section. The RIXS maps or spectra, on the other hand, needs to be tackled with proper computational tools. The following Appendix section presents some basic RIXS calculations on $[Co(bpy)_3]^{2+}$ and $[Co(bpy)_3]^{3+}$ using the newly released RIXS DFT/ROCIS code.

3.2.7 Appendix

The RIXS maps of Co L-edge and N K-edge for the LS configurations of $[Co(bpy)_3]^{2+}$ and $[Co(bpy)_3]^{3+}$ are shown in Figures 3.28 and 3.29. Fo the Co calculations, the active space consists of $2p$ of Co, Co $3d$ originated MOs and unoccupied MOs ≈5 eV above LUMO. Due to the lack of deeper valence orbitals, CT type relaxations are not observed on the calculated RIXS planes, rather, only d-d type transitions are observed.

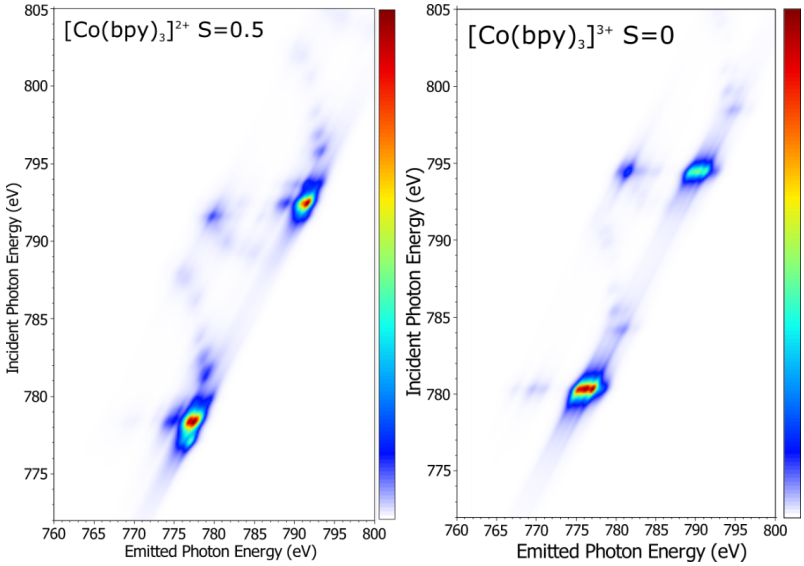

Figure 3.28: Calculated Co L-edge RIXS planes of $[Co(bpy)_3]^{2+}$ and $[Co(bpy)_3]^{3+}$ for LS configurations. RIXS planes of HS configurations could not be computed with sufficient parameters due to high computational needs. All the maps are shifted to match the energetic positions of the first intense feature of the experimental spectrum.

RIXS planes of HS configurations could not be computed with sufficient parameters due to high computational needs.

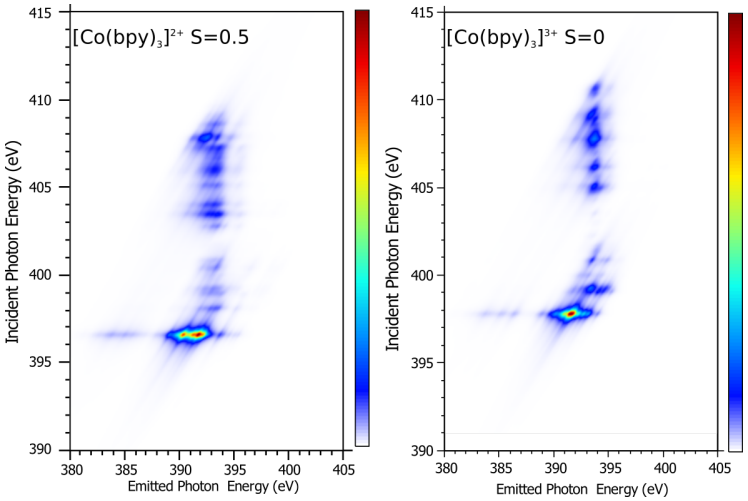

Figure 3.29: Calculated N K-edge RIXS planes of $[Co(bpy)_3]^{2+}$ and $[Co(bpy)_3]^{3+}$ for LS configurations. All the maps are shifted to match the energetic positions of the first intense feature of the experimental spectrum.

3.3 Electronic Structure of Aqueous Hexacyanochromate

In the previous Sections (3.1 and 3.2) good agreement between the experimental PFY-XA spectra and calculated Co L-edge and N K-edge XA spectra was demonstrated. This section is a preliminary attempt to study the electronic structure of aqueous hexacyanochromate using RIXS spectroscopy. The TM complexes with Cr metal center play an essential role in catalysis [159] and various industrial applications [160]. Unlike the Co centric complexes, hexacyanochromate exhibits an open shell d^3 configuration [36] under the octahedral CN^- ligand field. The octahedral ligand splits the valence $3d$ levels into three singly occupied t_{2g} levels and two completely empty e_g levels. This section discusses the preliminary experimental and theoretical results to understand the electronic structure of aqueous hexacyanochromate. The octahedral coordination of the Cr metal center and the six CN^- ligands is shown in Figure 3.30(a). As a starting point, I present the experimental PFY-XA spectrum along with the calculated transmission ("true") XA spectrum, which I labeled as trans XAS in Figure 3.30(b). The calculated XA spectrum exhibits strong deviation from the experimental spectrum in red, which is probably due to the implementation of open-shell electronic configuration d^3 in DFT/ROCIS code, especially in the presence of a strong ligand field. On the other hand, the calculated RIXS plane does exhibit distinct similarity with the corresponding experimental RIXS plane (see Figure 3.31 and 3.32; these figures will be introduced in detail in the following sections), and these differing behaviours will be discussed in the following sections. The RIXS maps presented in this section are calculated using the latest DFT/ROCIS module. This updated module allows for selection of orbitals, and this enables the calculation of different RIXS maps using chosen valence orbitals. The orbitals are selected based on their metal or ligand character using Löwdin distribution analysis. Thus, in principle, the complex experimental RIXS plane can be disentangled with the orbital-selective RIXS calculations. These calculated RIXS planes can then be

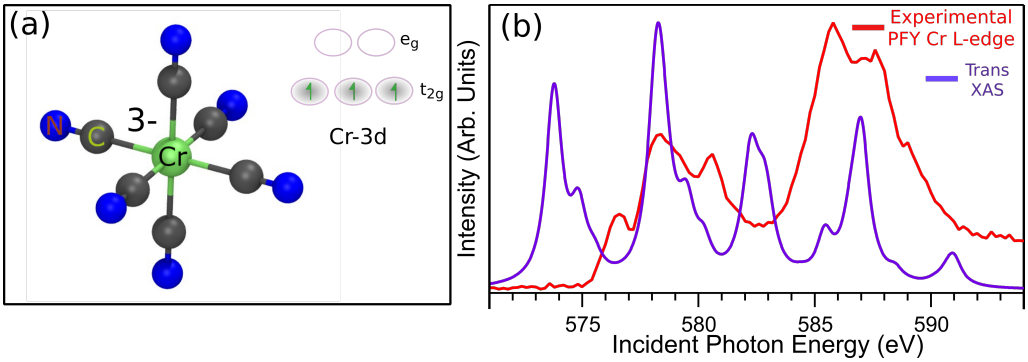

Figure 3.30: (a) The octahedral structure of $[Cr(CN)_6]^{3-}$ and Cr valence $3d$ electron levels (inset). (b) A comparison of experimental PFY-XA spectrum with DFT/ROCIS calculated XA spectrum (labeled as Trans XAS). Note, the calculated spectrum is shifted by 11.0 eV to 578.0 eV photon energy.

used for generating PFY-XA spectra with desired orbital contributions; these calculated PFY-XA spectra are compared with their experimental PFY-XA spectra counterparts at

the Cr L-edge and N K-edge.

3.3.1 Cr L-edge Experimental and Theoretical RIXS Study

A 100 mM aqueous solution was freshly prepared prior to experiments by dissolving Potassium hexa-cyanochromate(III) (purchased from Sigma Aldrich (purity >97%)) in Milli-Q water. The PFY-XA and RIXS and XE spectroscopy measurements at the Cr $L_{2,3}$-edge and N K-edge were carried out with the LiXEdrom setup employing the flow-cell technique at the U41-PGM undulator beamline; see Chapter 2 for more details. The energy resolution of the U41-PGM beamline was again better than 240 meV for the N 1s absorption measurements near 400 eV, and 600 meV for the Cr L-edge absorption measurements at photon energies above 550 eV.

The experimental RIXS map for the Cr L-edge obtained from 100 mM aqueous solution of potassium hexacyanochromate (III) is shown in Figure 3.31. The total acquisition time was approximately 175 min, and includes measurement of 150 individual RIXS spectra in the 560–590 eV photon emission range of the $3d \rightarrow 2p$ transitions. Across the L_3 resonance, the first emission signal is observed at an incident photon energy of 576.5 eV, consisting of a main peak at 574.0 eV (labeled C_1), a less intense and broad feature centered at 567.0 eV (labeled C_4), and an elastic (relaxation) peak at 576.5 eV. At the incident photon energy of 578.0 eV, the emission signal increases, giving a broad intense peak structure at 576.0 eV (labeled C_2), neighboring the vibrational progression of the elastic emission at 578.0 eV. The spectrum further features a broad weak signal between 565.0 and 571.0 eV (labeled C_6), bridging into the main peak between their mid-emission energies (labeled C_5). The next significant change in the emission signal is observed when tuning the incident photon energy to 581.0 eV. A new feature, centered at 572.0 eV (labeled C_7), is observed in the mid-energy region just mentioned. The main energy dispersive feature (marked by the pink line adjacent to the elastic lines) loses significant intensity for the emission energy around 579.0 eV (labeled C_3). For incident photon energies between 582.0 eV and 584.0 eV, fluorescence decreases significantly. In this dark zone only the Raman progression of the main emission intensity feature is visible, gradually shifting to higher energies upon increasing the incident photon energy.

Due to the shorter core-hole lifetime, the L_2 resonance exhibits broader emission features. In the 583.5–588.5 eV incident photon energy range, the main peak exhibits intensity in the 581.0–587.0 eV emission range as a double-lobe structure, labeled as C_8 and C_9. The pre-peak feature cannot be resolved as a separate entity unlike its L_3 counterpart. The second-most prominent feature is a wide emission roughly in the 584.0–589.0 eV incoming and 573.0–579.0 eV emission energy ranges. This feature is a convolution of two distinct types of emissions. First, it is the L_2 counterpart of the C_6 region observed in the L_3 resonance. Second, it covers roughly the same emission region as the main peak C_2, at the L_3 resonance, which makes it appearing as the non-resonant L_2 version of the L_3 main peak. Finally, at 589.0 eV incident photon energy, a feature appears (labeled C_{10}) which

is the counterpart of the L_3 feature C_7.

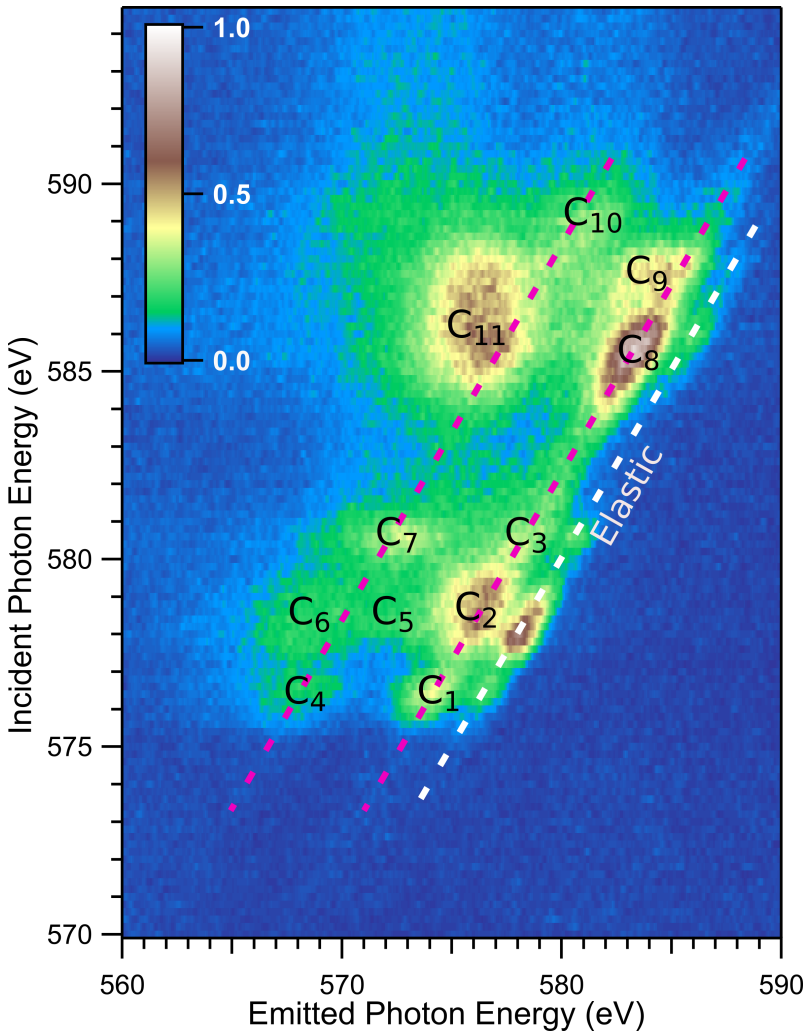

Figure 3.31: The Cr L-edge RIXS plane obtained from 100 mM $[Cr(CN)_6]^{3-}$ aqueous solution. The occurrence of the elastic line is marked with white dotted line. The Raman features appear along the red dotted lines. The important features are marked C_1–C_{11}.

To gain a better understanding about the observed spectral features and the explicit orbital characters of the $[Cr(CN)_6]^{3-}$ complex in aqueous solution, Cr L-edge RIXS planes were calculated using the newly released DFT/ROCIS method with ORCA Version 4. See Chapter 2 for more details. Molecular geometry optimizations were performed without symmetry constraints using the B3LYP [131, 132] density functional with the TZVP basis set. Transition energies and moments for the Cr L-edge were calculated with DFT/ROCIS using the same basis set and B3LYP [131, 132] functional. L-edge and K-edge absorption spectra were obtained by applying a 0.8 eV and 0.4 eV Lorentzian-type broadening on each transition moment, respectively. The calculated RIXS maps are shown in Figure 3.32 (a) to (d). This figure also marks the orbitals considered for the RIXS plane calculations (top left). The notations C_1 to C_{11} follow from Figure 3.31.

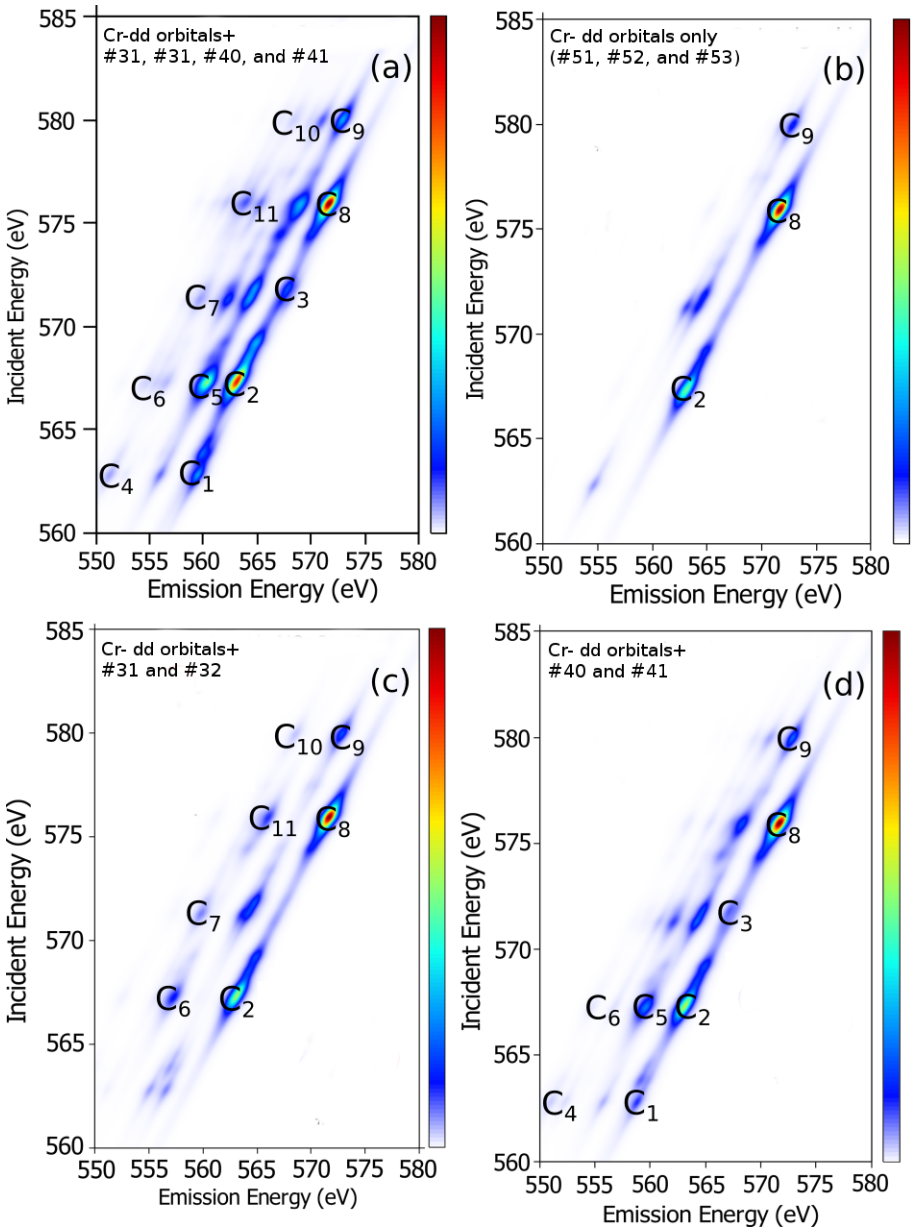

Figure 3.32: Calculated RIXS planes of $[Cr(CN)_6]^{3-}$ using DFT/ROCIS calculations as obtained by selective inclusion of certain occupied MOs with significant chromium contribution. (a) RIXS calculation including valence Cr *dd* orbitals (MOs #51–53) and deeper-lying MOs (MOs #31, #32, #40, and #41) with significant Cr 3*d* contributions. (b) RIXS plane calculated with only valence 3*d* orbitals (MOs #51–53). (c) RIXS plane calculated with Cr 3*d* (MOs #51–53) and MOs #31 and #32. (d) RIXS plane calculated with Cr 3*d* (MOs #51–53) and MOs #40 and #31.

The obtained incident and emission energy scales are presented without any energy shift applied. The nature of possible ground, intermediate and final states described within a DFT/ROCIS calculation is determined by choosing the appropriate donor and acceptor spaces. Here, the core (or first) donor space is given by the three Cr 2*p* orbitals as we are interested in the Cr- L-edge. All unoccupied restricted open-shell Kohn-Sham (ROKS)

orbitals with energies below 8.0 eV comprise the virtual space. The energy threshold was chosen to be close to the first ionization energy, which was estimated using the energy of the HOMO (-7.3 eV), as one is only interested in near-edge features. For the chosen combination of exchange-correlation-functional (XC) and basis set the employed virtual space then has a size of 27 orbitals.

One key factor in the calculation of TM L-edge RIXS planes is the necessity to restrict the valence (or second) donor space to TM and ligand orbitals that give rise to those intermediate and final states most relevant for the observed peak structure. An ideal RIXS plane calculation in the case of Cr can be achieved by including all the valence orbitals of the complex $[Cr(CN)_6]^{3-}$. Based on Löwdin analysis, this requires the inclusion of 32 valence orbitals; such a RIXS calculation is highly impractical. This difficulty can

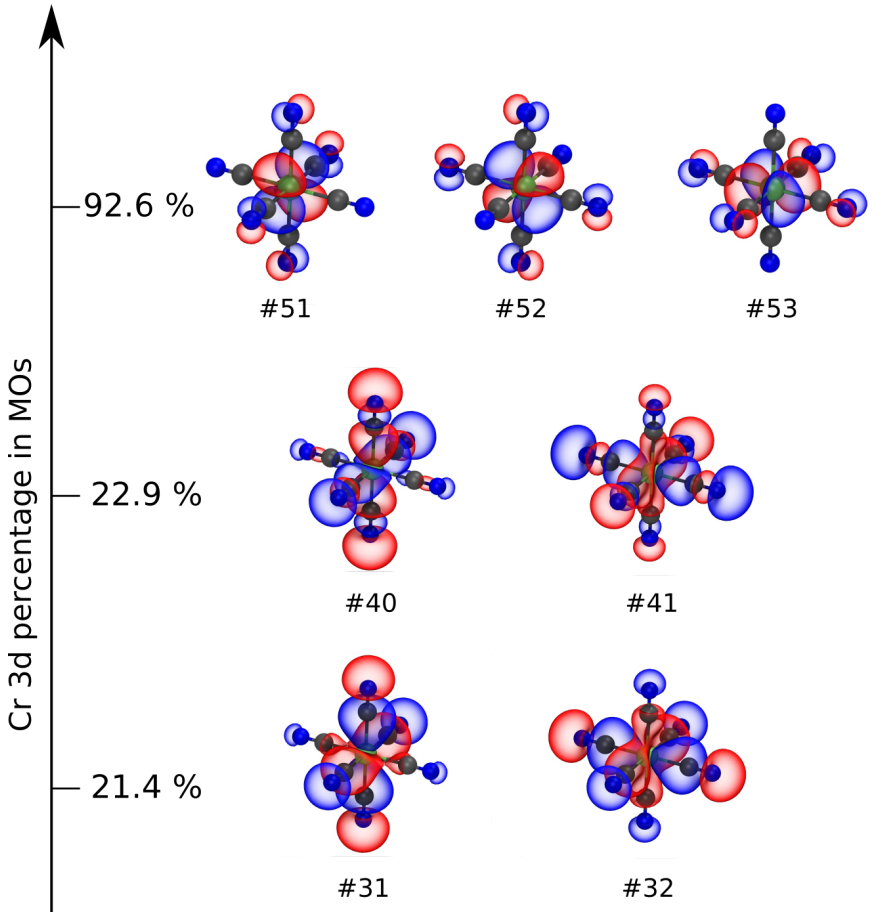

Figure 3.33: Selected MOs of $[Cr(CN)_6]^{3-}$ with varying Cr 3*d* participation. The deeper valence orbitals #31, #32, #40, and #41 have Cr 3*d* contributions exceeding 20%. Visualizations of molecules and orbitals were created using Orbkit [161] and VMD [162, 163] software packages.

be bypassed by including only valence orbitals with dominant Cr 3*d* contributions which are of major importance for L-edge structure. Figure 3.33 introduces valence and deeper valence orbitals with significant Cr 3*d* contributions. The valence MOs #51, #52, and #53 have metal 3*d* t_{2g} character, whereas the deeper valence MOs #31, #32, #40, and

#41 have 3d e_g character as illustrated in Figure 3.33. The deeper-lying valence orbitals with a significant Cr Löwdin population (above 20 %), namely the MOs #31, #32, #40 and #41, which are involved in transition metal–ligand bonding and the Cr 3*d* orbitals (MOs #50, #51 and #53 above 90%) in the valence donor space results in a RIXS plane, which reproduces the relative positions of all observed features C_1–C_{11}; see Figure 3.32(a). Restriction of the valence donor space to the Cr 3*d* orbitals, which have a marginal ligand contribution (Cr Lödwin populations of 93 %), gives rise to a much simpler RIXS plane, from which the experimentally observed features C_2, C_8 and C_9 can be assigned to 2*p* - 3*d* transitions as shown in Figure 3.32(a). Addition of the lower-lying MOs #31 and #32 to the Cr 3*d* orbitals in the valence donor space, gives rise to the features C_6, C_7, C_{11}, as shown in Figure 3.32(c). The inclusion of the MOs #40 and #41, on the other hand, gives signals associated with the features C_4, C_5 and C_3 as shown in Figure 3.32(d). The present comparison of RIXS planes from experiment and DFT/ROCIS calculations thus shows strong evidence for the sensitivity of Cr L-edge RIXS towards transitions involving transition from metal–ligand bonding orbitals.

3.3.2 Preliminary Analysis of Cr L-edge Experimental PFY-XA Using Calculated XA Spectra

The calculated Cr L-edge PFY-XA spectra were obtained by integrating the RIXS spectra (Figure 3.32(a)–(d)) and projection on the incident photon energy axis. Figure 3.34, top panel (c), shows the Cr L-edge experimental PFY-XA spectrum, bottom tiers (b) show PFY-XA spectra obtained by integrating the calculated RIXS maps, and it also presents the transmission XA spectrum (violet) at the bottom. To facilitate the comparison of relative peak positions, the L_3-edges of the calculated spectra have been aligned with those of the measured one, applying a shift of 11 eV. The contributions from different fluorescence features marked in Figure 3.31 and 3.32 are indicated in the experimental PFY-XA spectrum.

The first experimental peak at 576.5 eV is associated to features C_1 and C_4 from Figure 3.31, where the former gives the major fluorescence contribution. The increased intensity of the next peak at 578.7 eV stems from the significant contribution from broad fluorescence feature C_2. Further small contributions from the broad and weak emission features C_5 and C_6, respectively, also account for the PFY signal intensity at this energy. A shoulder at 580.0 eV observed in the calculated PFY-XA spectra is marked by dotted lines. The third observed peak of the L_3 resonance at 580.6 eV is associated to the C_7 and C_3 emission signals. A strikingly intense L_2 resonance near 587.0 eV yields the most intense and broad PFY-XA signal. This large intensity is attributed to two factors: the intense near resonant L_2 signal fluorescence at C_8, and the the very broad C_{11} corresponding to non-resonant L_3 emission signal. A similar broad emission feature is also observed in Cr-hexaaqua studies [164]. The broad width of the L_2 resonance can be due to the side features observed at

585.5 eV and 588.5 eV, indicated by the dotted lines in the calculated PFY-XA spectra. The broad width at L_2 resonance can also associated with the Coster–Kronig transition [165] and resulting fluorescence. Lastly, the RIXS signals C_9 and C_{10} give rise to the peak structure at 589.5 eV on the high energy shoulder of the L_3 PFY-XA signal.

The Cr L-edge PFY spectra from RIXS DFT/ROCIS calculations with increasing valence donor spaces including Cr *d* orbitals and mixed Cr-CN orbitals (see Figure 3.33) compare well with the experimentally observed PFY spectrum (Figure 3.34(a)). The relative intensity difference between the L_3 and L_2 edges is qualitatively reproduced in RIXS DFT/ROCIS level (see the blue and cyan spectra in Figure 3.34(b)). From Figure 3.32, the major contribution to the observed intensity variation can be associated with features C_2 and C_8. Addition of the metal–ligand orbitals to the valence donor space results mainly in an increase of the intensity of the C_2 feature with respect to C_8; see the intensity variation of C_2 feature in Figure 3.32. The calculated pre-edge L_3 features C_1, C_4 are shifted to lower incident photon energies, while the post-edge features C_3 and C_7 are shifted to higher energies relative to the C_2 peak. Hence, the calculated PFY spectra of the L_3 edge is stretched over an energy interval about twice as large as the experimentally measured one.

Vinogradov et al. reported the TEY-XA spectrum of powder $[Cr(CN)_6]^{3-}$ [38], where the first two intense peaks are energetically separated by 2.8 eV; the separation between the second and third intense peak is 1.8 eV. The PFY-XA spectra shown in Figure 3.34(a), the first two intense peaks are separated by 2.2 eV, and the second and third intense peaks are energetically separated by 1.9 eV. The peaks at 575.5 and 578.7 eV correspond to the transitions to unoccupied *d* t_{2g} and *d* e_g MOs, whereas the second peak at 580.6 eV corresponds to the backbonding π^* orbitals [38].

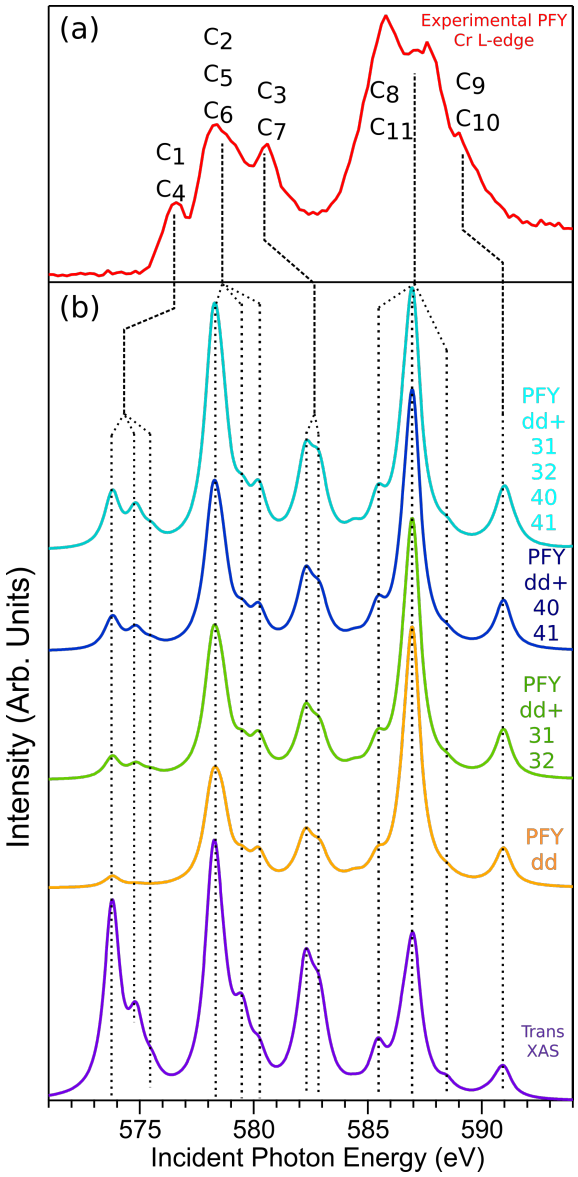

Figure 3.34: Comparison of various calculated Cr L-edge absorption spectra (b) with the experimental PFY-XA spectrum (a). The transmission XA spectrum is shown in violet. The calculated PFY spectra are obtained by integrating the calculated RIXS maps (see Figure 3.32 (a)-(d)) with orbital selectivity. Orbital numbers responsible for the intensities are also shown.

Figure 3.34 also shows the transmission XA spectrum (Trans XAS) calculated at the DFT/ROCIS level of theory. Naturally, the XA transitions occur at the same energies as in the case of RIXS-PFY with the valence donor space including Cr 3*d* and Cr-CN orbitals. A significant difference however arises for the relative peak intensities. In the absorption spectrum, the intensities of the L_2 resonance peaks are significantly enhanced which leads to an inverted intensity pattern compared to the calculated and measured PFY-XA spectrum. It is to be noted that the present alignment of the calculated XA spectrum to match the experimental PFY spectrum is guided by the comparison of calculated and

measured RIXS planes.

3.3.3 N K-edge Experimental and Theoretical RIXS Study

Next, I discuss the ligand excitation by sweeping the photon energy across the N K-edge. The obtained RIXS map is presented in Figure 3.35. Inspection of the measured nitrogen K-edge RIXS plane reveals a much simpler structure in comparison to the Cr L-edge. The singular main feature is an emission band at 392.0 eV, with a width of about 3.0 eV, occurring within the 398.0 eV to 401.0 eV window of incident photon energies. The maximum emission intensity of this feature is observed at an incident photon energy of 399.6 eV. Progressing towards incident photon energies larger than 401.0 eV results in an increasing emission signal centered at 394.0 eV due to the fluorescence emission from the ionized complex.

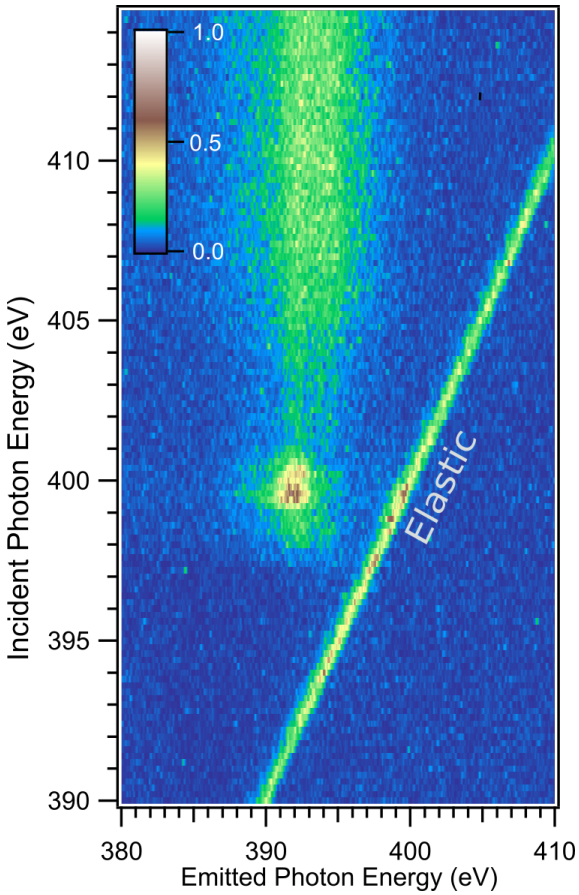

Figure 3.35: The N K-edge RIXS plane obtained from 100 mM aqueous $[Cr(CN)_6]^{3-}$.

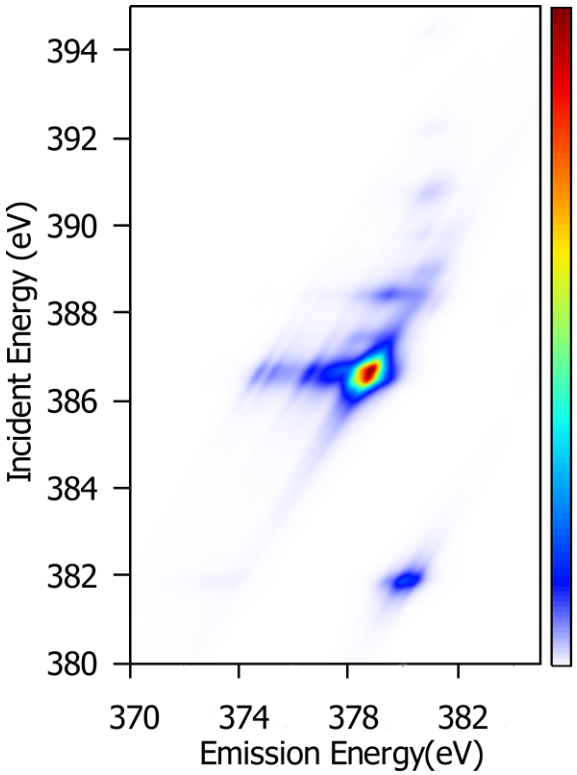

Figure 3.36: Calculated N K-edge RIXS plane of $[Cr(CN)_6]^{3-}$ using DFT/ROCIS method. Unlike for the Cr L-edge, this calculation includes all the MOs which can relax to the core-hole are included. The calculated RIXS map is presented without any shift on the energy axes.

The nitrogen K-edge RIXS plane calculated using the DFT/ROCIS method is shown in Figure 3.36. Its peak structure, with one strong emission signal is, besides the typical shift in energy inherent to the DFT methods, in agreement with the experimental result. The pre-edge peak, which appears at about 4.0 eV lower incident photon energy as the main peak could not be observed in the experiment.

Compared to Cr L-edge the RIXS plane of N K-edge exhibits simpler features. Specifically, the nitrogen K-edge PFY-XA spectrum consists of a single peak near 400.0 eV with a small shoulder at 399.0 and 401.0 eV; see Figure 3.37. All the calculated XA spectra were aligned at the most intense peak near 400.0 eV of the experimental PFY-XA spectrum. The shoulders at 399.0 eV and 401.0 eV are also in agreement with the experimentally observed shoulders. The satellite peaks at 395.0 (green and violet), 396.5 (yellow), and 401.5 eV are absent in the experimental spectrum. Compared to the case of the Cr L-edge, the calculated PFY-XA spectrum matches the calculated XA spectrum exactly (see the violet and green spectra in Figure 3.37).

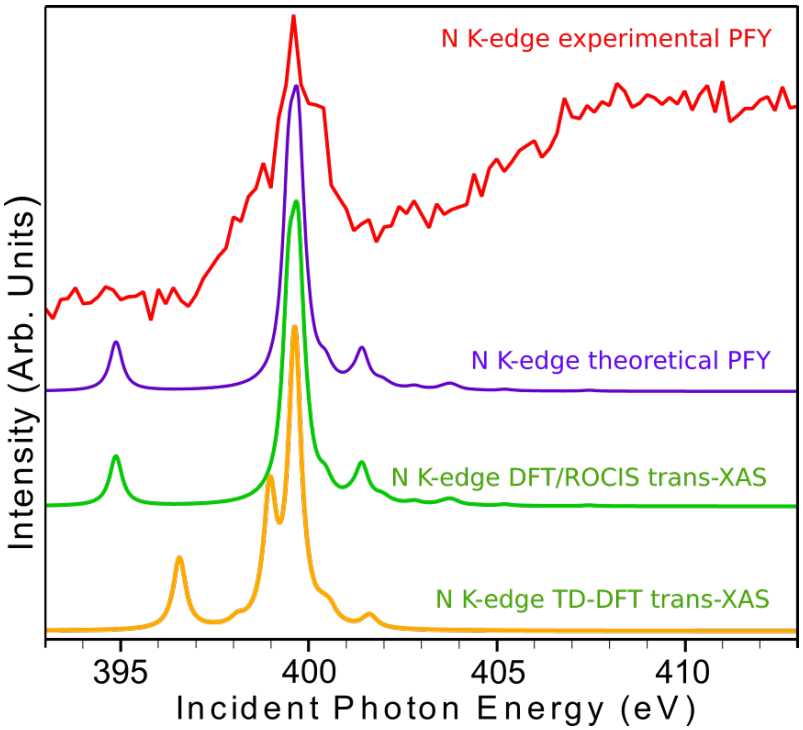

Figure 3.37: Nitrogen K-edge experimental PFY-XA spectrum is compared to various computed XA spectra. The computed transmission XA spectrum is calculated using both TD-DFT and DFT/ROCIS theory.

Further comparison of the transmission XA spectrum obtained from DFT/ROCIS and TD-DFT reveals only minor differences, such as the splitting of the main peak, and a blue shift of the pre-edge peak in the TD-DFT XA spectra. However, both results compare well with the experimental PFY-XA spectrum and an increased experimental resolution would be necessary to resolve those differences. In summary, the case of the nitrogen K-edge shows that under certain circumstances the calculated PFY-XA spectrum indeed reasonably well reproduces a transmission XA spectrum, and calculated XA spectra can be directly compared to the experimentally measured PFY-XA spectrum.

3.3.4 Summary

This section analyzed an experimental L-edge PFY-XA spectrum using a calculated XA spectrum (or trans-XA spectrum from the normal DFT/ROCIS code) and also an XA spectrum generated from the RIXS map calculation. Generation of an accurate L-edge XA spectrum is complicated in the case of $[Cr(CN)_6]^{3-}$. To a certain extent, this difficulty can be surpassed though by generating the PFY-XA spectrum at the Cr L-edge through the integration of Cr L-edge RIXS planes. The experimental RIXS plane at the Cr L-edge exhibits fluorescence and energy dispersive (Raman) features. The Cr L-edge RIXS planes were generated using selected orbitals with significant metal and ligand contributions; Löwdin population analysis was the selection criteria for orbitals. The calculated RIXS planes obtained using hand-picked orbitals qualitatively describes the experimental

RIXS map. However, for a complete description of the RIXS process, information about intermediate RIXS states are necessary.

Regarding the experimental PFY-XA spectrum, a preliminary qualitative description of intensity and energetic positions of the peaks were detailed, facilitated through the various calculated PFY-XA spectra. On the other hand, the experimental ligand N K-edge RIXS plane was calculated using the same RIXS DFT/ROCIS code with reasonable accuracy. The calculated PFY-XA spectrum is also in agreement with the experimental counterparts; an analogous calculated XA spectrum is also obtained from TD-DFT and DFT/ROCIS methods.

4. Summary and Outlook

Electronic structure of aqueous transition metal complexes, with focus on hexacyano cobaltate, cobalt(II) tris-bipyridine and cobalt(III) tris-bipyridine, was investigated using resonant inelastic X-ray scattering and resonant photoemission spectroscopies across the Co L-edges and N K-edges. The partial fluorescence yield and partial electron yield (only for hexacyanocobaltate) X-ray absorption spectra were obtained by integrating the resonant inelastic X-ray spectra (RIXS) and the resonant photoemission (RPE) spectra, respectively. Co L-edge and N K-edge X-ray absorption and emission spectra were calculated using DFT/ROCIS and TD-DFT methodologies for assisting the analysis of the experimental spectra.

A thorough investigation of the electronic structure of the aqueous $[Co(CN)_6]^{3-}$ complex is achieved combining RIXS and RPE methodologies. The valence photoemission studies were performed using non-resonant (200 eV) and resonant photons, respectively. Signal enhancements by orders of magnitude were found for resonant excitations. Both Co and N edges of $[Co(CN)_6]^{3-}$ exhibit resonant enhancements, even at similar binding energy (one at 20.5 eV) positions, suggesting strong metal–ligand orbital mixing. Also, the binding energies of highly mixed-character Co and N orbitals were also obtained from the valence RPE spectra. The assignments of the RPE spectra are based on the ground-state DFT calculations. Bonding strength is the other important property investigated for this particular molecule, revealed from the signal-integrated PFY- and PEY-XA spectra at the Co L-edge and N K-edge. The ratios of σ^*-to-π^* peak intensity were compared in the Co L-edge and N K-edge XA spectra. The amount of metal–ligand orbital mixing is directly linked to the intensity of the π^* peak. Differential metal $3d$ and ligand contributions to these σ^* and π^* orbitals were obtained using ground-state DFT calculations.

A very close agreement between experimental and calculated XA spectra found for the aqueous $[Co(CN)_6]^{3-}$ complex can be attributed to the $3d^6$ low-spin configuration and the near-octahedral symmetry of the molecule.

As a next step I studied the electronic structure of aqueous electron mediators $[Co(bpy)_3]^{2+}$ and $[Co(bpy)_3]^{3+}$complexes. The PFY-XA spectra at the Co L-edge from these two complexes are drastically different from the Co L-edge XA spectrum from the aqueous hexacyanocobaltate molecule, even though all of these molecules have octahedral symmetry. A ground-state optimization calculation for different spin configurations suggests a distorted

octahedral symmetry, especially for the high-spin configurations. Unlike $[Co(CN)_6]^{3-}$, the RIXS maps of $[Co(bpy)_3]^{2+}$ and $[Co(bpy)_3]^{3+}$ molecules exhibit dispersive features due to *d-d* and charge transfer (CT) excitations. Generally speaking, these dispersive features are indications of an open-shell valence *3d* electron distribution. Strong evidence of metal–ligand orbital mixing was elucidated by comparing N K-edge X-ray emission spectra with their respective calculated counterparts. The complex nature of PFY-XA spectra was analyzed by calculating XA spectra for low-spin and high-spin configurations for the two molecules. A linear combination of the calculated low-spin and high-spin Co L-edge spectra resembles their experimental counterparts. For $[Co(bpy)_3]^{2+}$ molecule, the experimental Co L-edge PFY-XA spectrum was obtained by ≈43% low-spin and ≈57% high-spin state components. For $[Co(bpy)_3]^{3+}$, much stronger low spin favors the experimental Co L-edge PFY-XA spectrum, with ≈80% low-spin and ≈20% high-spin state components. Thus, when analyzing the experimental L-edge XA spectrum of TM complexes like $[Co(bpy)_3]^{2+}$ and $[Co(bpy)_3]^{3+}$, a possibility of their occurrence with different spin states must be considered. Interestingly, the N K-edge PFY-XA spectra from both molecules exhibit similar peak structures, unlike the respective Co spectra. This similarity shows that the ligand N K-edge PFY-XA spectra are rather insensitive to the changes in spin configurations of the central metal atom.

The electronic structure RIXS study of $[Co(bpy)_3]^{2+}$ and $[Co(bpy)_3]^{3+}$ molecules was restricted to flow-cell measurements due to the small available quantity of these rather expensive chemicals. The RPE measurement, however needs to be conducted using a liquid-jet technique. Future RPE measurements of these samples and a comparative study with RIXS measurements are possible, similar to the $[Co(CN)_6]^{3-}$ case presented in Section 3.1 of this thesis . Furthermore, it would be interesting to extend to similar molecules like $[Co(Phen)_3]^{2+}$ and $[Co(Phen)_3]^{3+}$, which are also used as electron mediators. Another important variable to explore is the nature of the solvent, such as changing from water to dimethyl sulfoxide (DMSO) or to acetonitrile with suitable counter anions such as SO^{4-} and $PF_6{}^{-}$. The reduction and oxidation study of redox mediators are also of importance. Such study can be conducted using an electrochemical flow-cell. An external voltage applied with the help of electrodes can cause oxidation/reduction of the sample inside the electrochemical flow-cell. Evolution of absorption edge can be monitored using X-ray methods as a function of applied potential.

There is also a need for improving the RIXS spectrum/map calculations. The outlook Section 3.3, describing the electronic structure of $[Cr(CN)_6]^{3-}$ presents some progress in this direction. The enhanced DFT/ROCIS code released with the ORCA version 4 is now capable of generating the RIXS map and spectrum. But a successful calculation including all the relevant orbitals still eludes due to the limited computational resources; this limitation applies especially for larger molecules like $[Co(bpy)_3]^{2+}$ and $[Co(bpy)_3]^{3+}$. The calculated RIXS maps presented in Section 3.3 were generated using hand-picked valence orbitals, chosen by their respective metal and ligand contributions. The RIXS maps ob-

tained by this method can be used to generate integrated XA spectra. Such derived XA spectra in principle will be more suitable for comparison with their experimental counterparts. Another objective of the RIXS calculations is to gather information about the intermediate states involved in the RIXS process. This information could explain the varying intensities observed in an experimental RIXS spectrum in detail.

In summary, this thesis presents the detailed electronic structure studies of $[Co(CN)_6]^{3-}$, $[Co(bpy)_3]^{2+}$ and $[Co(bpy)_3]^{3+}$ molecules in aqueous solution using soft X-ray spectroscopies, detecting energies of emitted electrons and photons.

List of Figures

List of Abbreviations

BE	binding energy
CC	coupled cluster
CCD	charge coupled device
CI	configuration interaction
CIS	configuration interaction singles
COSMO	conductor-like screening model
CPCM	conductor like polarizable continuum model
CT	charge transfer
DFT	density functional theory
DOMO	doubly occupied molecular orbital
EA	energy analyzer
HOMO	highest occupied molecular orbital
HPLC	high pressure liquid chromatography
HS	high spin
IS	intermediate spin
KE	kinetic energy
LS	low spin
LUMO	lowest unoccupied molecular orbitals
MCP	micro-channel plate
MLCT	metal-to-ligand charge transfer
MO	molecular orbital
MRCI	multi-reference configuration interaction
PE	photoelectron
PEY	partial electron yield
PFY	partial fluorescence yield
RIXS	resonant inelastic X-ray scattering
ROCIS	restricted open shell configuration interaction singles

RPE	resonant photoelectron
Si_3N_4	silicon nitride
SiC	silicon carbide
SOMO	singly occupied molecular orbital
TD-DFT	time dependant density functional theory
TEY	total electron yield
TM	transition metal
UV-Vis	Ultraviolet–visible spectroscopy
XA	X-ray absorption
XC	exchange-correlation-functional
XE	X-ray emission
XPS	X-ray photoelectron spectroscopy
ZORA	zeroth order regular approximation

Appendix

O_h	E	$8C_3$	$6C_2$	$6C_4$	$3C_2(=C_4{}^2)$	i	$6S_4$	$8S_6$	$3\sigma_h$	$6\sigma_d$		
A_{1g}	1	1	1	1	1	1	1	1	1	1		
A_{2g}	1	1	-1	-1	1	1	-1	1	1	-1		
E_g	2	-1	0	0	2	2	0	-1	2	0		$(2z^2-x^2-y^2,\ x^2-y^2)$
T_{1g}	3	0	-1	1	-1	3	1	0	-1	-1	$(R_x,\ R_y,\ R_z)$	
T_{2g}	3	0	1	-1	-1	3	-1	0	-1	1		$(xy,\ xz,\ yz)$
A_{1u}	1	1	1	1	1	-1	-1	-1	-1	-1		
A_{2u}	1	1	-1	-1	1	-1	1	-1	-1	1		
E_u	2	-1	0	0	2	-2	0	1	-2	0		
T_{1u}	3	0	-1	1	-1	-3	-1	0	1	1	$(x,\ y,\ z)$	
T_{2u}	3	0	1	-1	-1	-3	1	0	1	-1		

Table A0.0: The character table for O_h symmetry

References

1. Röntgen, W. C. On a new kind of rays. *Science* **3,** 227–231 (1896).
2. Van Bokhoven, J. A. & Lamberti, C. *X-ray Absorption and X-ray Emission Spectroscopy: Theory and Applications* (John Wiley & Sons, 2016).
3. Lin, F., Liu, Y., Yu, X., Cheng, L., Singer, A., Shpyrko, O. G., Xin, H. L., Tamura, N., Tian, C., Weng, T.-C., *et al.* Synchrotron X-ray analytical techniques for studying materials electrochemistry in rechargeable batteries. *Chemical Reviews* **117,** 13123–13186 (2017).
4. Tsakanov, V. & Wiedemann, H. *Brilliant Light in Life and Material Sciences* (Springer Science & Business Media, 2007).
5. Margaritondo, G. *Introduction to Synchrotron Radiation* (Oxford University Press, 1988).
6. Artero, V., Chavarot-Kerlidou, M. & Fontecave, M. Splitting Water with Cobalt. *Angewandte Chemie International Edition* **50,** 7238–7266 (2011).
7. Zhang, X.-M., Li, C.-R., Zhang, X.-H., Zhang, W.-X. & Chen, X.-M. Unusual Slow Magnetic Relaxation in Helical $Co_3(OH)_2$ Ferrimagnetic Chain Based Cobalt Hydroxysulfates. *Chemistry of Materials* **20,** 2298–2305 (2008).
8. Yella, A., Lee, H.-W., Tsao, H. N., Yi, C., Chandiran, A. K., Nazeeruddin, M. K., Diau, E. W.-G., Yeh, C.-Y., Zakeeruddin, S. M. & Grätzel, M. Porphyrin-Sensitized Solar Cells with Cobalt (II/III)–Based Redox Electrolyte Exceed 12 Percent Efficiency. en. *Science* **334,** 629–634 (2011).
9. Krishnan, C. V. & Sutin, N. Homogeneous catalysis of the photoreduction of water by visible light. 2. Mediation by a tris(2,2'-bipyridine)ruthenium(II)-cobalt(II) bipyridine system. *Journal of the American Chemical Society* **103,** 2141–2142 (1981).
10. Krishnan, C. V., Brunschwig, B. S., Creutz, C. & Sutin, N. Homogeneous catalysis of the photoreduction of water. 6. Mediation by polypyridine complexes of ruthenium(II) and cobalt(II) in alkaline media. *Journal of the American Chemical Society* **107,** 2005–2015 (1985).
11. Kellett, R. M. & Spiro, T. G. Cobalt(I) porphyrin catalysts of hydrogen production from water. *Inorganic Chemistry* **24,** 2373–2377 (1985).

12. Losse, S., Vos, J. G. & Rau, S. Catalytic hydrogen production at cobalt centres. *Coordination Chemistry Reviews. 18th International Symposium on the Photochemistry and Photophysics of Coordination Compounds Sapporo, 2009* **254,** 2492–2504 (2010).

13. Bigi, J. P., Hanna, T. E., Harman, W. H., Chang, A. & Chang, C. J. Electrocatalytic reduction of protons to hydrogen by a water-compatible cobalt polypyridyl platform. en. *Chemical Communications* **46,** 958–960 (2010).

14. Feldt, S. M., Gibson, E. A., Gabrielsson, E., Sun, L., Boschloo, G. & Hagfeldt, A. Design of Organic Dyes and Cobalt Polypyridine Redox Mediators for High-Efficiency Dye-Sensitized Solar Cells. *Journal of the American Chemical Society* **132,** 16714–16724 (2010).

15. Atkins, P. & Overton, T. *Shriver and Atkins' Inorganic Chemistry* (Oxford University Press, 2010).

16. Khnayzer, R. S., Thoi, V. S., Nippe M. and King, A. E., Jurss, J. W., Roz, K. A. E., Long, J. R., Chang, C. J. & Castellano, F. N. Towards a comprehensive understanding of visible-light photogeneration of hydrogen from water using cobalt(ii) polypyridyl catalysts. en. *Energy & Environmental Science* **7,** 1477–1488 (2014).

17. Sun, Y., Bigi, J. P., Piro, N. A., Tang, M. L., Long, J. R. & Chang, C. J. Molecular Cobalt Pentapyridine Catalysts for Generating Hydrogen from Water. *Journal of the American Chemical Society* **133,** 9212–9215 (2011).

18. Sasaki, Y., Kato, H. & Kudo, A. $[Co(bpy)_3]^{3+/2+}$ and $[Co(phen)_3]^{3+/2+}$ Electron Mediators for Overall Water Splitting under Sunlight Irradiation Using Z-Scheme Photocatalyst System. *Journal of the American Chemical Society* **135,** 5441–5449 (2013).

19. Seidel, R., Atak, K., Thürmer, S., Aziz, E. F. & Winter, B. Ti^{3+} Aqueous Solution: Hybridization and Electronic Relaxation Probed by State-Dependent Electron Spectroscopy. *The Journal of Physical Chemistry B* **119,** 10607–10615 (2015).

20. Kunnus, K., Zhang, W., Delcey, M. G., Pinjari, R. V., Miedema, P. S., Schreck, S., Quevedo, W., Schröder, H., Föhlisch, A., Gaffney, K. J., *et al.* Viewing the valence electronic structure of ferric and ferrous hexacyanide in solution from the fe and cyanide perspectives. *The Journal of Physical Chemistry B* **120,** 7182–7194 (2016).

21. Atak, K., Bokarev, S. I., Gotz, M., Golnak, R., Lange, K. M., Engel, N., Dantz, M., Suljoti, E., Kühn, O. & Aziz, E. F. Nature of the chemical bond of aqueous Fe2+ probed by Soft X-ray spectroscopies and ab initio calculations. *The Journal of Physical Chemistry B* **117,** 12613–12618 (2013).

22. Bokarev, S. I., Dantz, M., Suljoti, E., Kühn, O. & Aziz, E. F. State-dependent electron delocalization dynamics at the solute-solvent interface: soft-x-ray absorption spectroscopy and Ab initio calculations. *Physical Review Letters* **111,** 083002 (2013).

23. Golnak, R., Xiao, J., Atak, K., Khan, M., Suljoti, E. & Aziz, E. F. Local Energy Gap Opening Induced by Hemin Dimerization in Aqueous Solution. *The Journal of Physical Chemistry B* **119,** 3058–3062 (2015).

24. Atak, K., Golnak, R., Xiao, J., Suljoti, E., Pflueger, M., Brandenburg, T., Winter, B. & Aziz, E. F. Electronic structure of hemin in solution studied by resonant x-ray emission spectroscopy and electronic structure calculations. *The Journal of Physical Chemistry B* **118,** 9938–9943 (2014).

25. Xiao, J., Golnak, R., Atak, K., Pflüger, M., Pohl, M., Suljoti, E., Winter, B. & Aziz, E. F. Assistance of the iron porphyrin ligands to the binding interaction between the Fe center and small molecules in solution. *The Journal of Physical Chemistry B* **118,** 9371–9377 (2014).

26. Yin, Z., Inhester, L., Thekku Veedu, S., Quevedo, W., Pietzsch, A., Wernet, P., Groenhof, G., Föhlisch, A., Grubmüller, H. & Techert, S. Cationic and Anionic Impact on the Electronic Structure of Liquid Water. *The Journal of Physical Chemistry Letters* **8,** 3759–3764 (2017).

27. Nagasaka, M., Yuzawa, H. & Kosugi, N. Interaction between Water and Alkali Metal Ions and Its Temperature Dependence Revealed by Oxygen K-Edge X-ray Absorption Spectroscopy. *The Journal of Physical Chemistry B* **121,** 10957–10964 (2017).

28. Näslund, L.-Å., Cavalleri, M., Ogasawara, H., Nilsson, A., Pettersson, L. G., Wernet, P., Edwards, D. C., Sandström, M. & Myneni, S. Direct evidence of orbital mixing between water and solvated transition-metal ions: An oxygen 1s XAS and DFT study of aqueous systems. *The Journal of Physical Chemistry A* **107,** 6869–6876 (2003).

29. Seidel, R., Winter, B. & Bradforth, S. E. Valence electronic structure of aqueous solutions: Insights from photoelectron spectroscopy. *Annual Review of Physical Chemistry* **67,** 283–305 (2016).

30. Golnak, R., Bokarev, S. I., Seidel, R., Xiao, J., Grell, G., Atak, K., Unger, I., Thürmer, S., Aziz, S. G., Kühn, O., *et al.* Joint analysis of radiative and non-radiative electronic relaxation upon X-ray irradiation of transition metal aqueous solutions. *Scientific Reports* **6** (2016).

31. Attwood, D. & Sakdinawat, A. *X-rays and Extreme Ultraviolet Radiation: Principles and Applications* (Cambridge University Press, 2017).

32. Willmott, P. *An Introduction to Synchrotron Radiation : Techniques and Applications* first edition (Wiley, 2011).

33. Smith, J. W. & Saykally, R. J. Soft X-ray Absorption Spectroscopy of Liquids and Solutions. *Chemical Reviews* **117,** 13909–13934 (2017).

34. Bunker, G. *Introduction to XAFS: A Practical Guide to X-ray Bbsorption Fine Structure Spectroscopy* (Cambridge University Press, 2010).

35. Chantler, C. T., Olsen, K. J., Dragoset, R. A., Kishore, A. R., Kotochigova, S. A. & Zucker, D. S. *X-Ray form factor, attenuation and scattering tables (version 2.0)* tech. rep. (2003).

36. Miessler, G., Fischer, P. & Tarr, D. *Inorganic Chemistry* (Pearson, 2014).

37. Jmol. *Jmol: an open-source Java viewer for chemical structures in 3D.* `http://www.jmol.org/` (2018).

38. Vinogradov, A. S., Preobrajenski, A. B., Knop-Gericke, A., Molodtsov, S. L., Krasnikov, S. A., Nekipelov, S., Szargan, R., Hävecker, M. & Schlögl, R. Observation of back-donation in 3d metal cyanide complexes through NK absorption spectra. *Journal of Electron Spectroscopy and Related Phenomena* **114,** 813–818 (2001).

39. Jahn, H. A. & Teller, E. Stability of polyatomic molecules in degenerate electronic states - I–Orbital degeneracy. *Proceedings of the Royal Society of London. Series A - Mathematical and Physical Sciences* **161,** 220–235 (1937).

40. Winter, B., Weber, R., Widdra, W., Dittmar, M., Faubel, M. & Hertel, I. Full valence band photoemission from liquid water using EUV synchrotron radiation. *The Journal of Physical Chemistry A* **108,** 2625–2632 (2004).

41. Penner-Hahn, J. E. X-ray absorption spectroscopy in coordination chemistry. *Coordination Chemistry Reviews* **190-192,** 1101–1123 (1999).

42. Bressler, C. & Chergui, M. Ultrafast X-ray Absorption Spectroscopy. *Chemical Reviews* **104,** 1781–1812 (2004).

43. Eisenberger, P., Shulman, R. G., Kincaid, B. M., Brown, G. S. & Ogawa, S. Extended X-ray absorption fine structure determination of iron nitrogen distances in haemoglobin. *Nature* **274,** 30–34 (1978).

44. De Groot, F. & Kotani, A. *Core Level Spectroscopy of Solids* (CRC press, 2008).

45. De Groot, F. M. F. Ligand and metal X-ray absorption in transition metal complexes. *Inorganica Chimica Acta. Protagonists in Chemistry: Professor Edward I Solomon* **361,** 850–856 (2008).

46. Veenendaal, M. v. *Theory of Inelastic Scattering and Absorption of X-rays* en (Cambridge University Press, 2015).

47. Akgül, G., Aksoy, F., Bozduman, A., Ozkendir, O. M., Ufuktepe, Y. & Lüning, J. Study of the $L_{2,3}$ edges of 3d transition metals by X-ray absorption spectroscopy. *Thin Solid Films* **517,** 1000–1004 (2008).

48. Ruosi, A., Raisch, C., Verna, A., Werner, R., Davidson, B. A., Fujii, J., Kleiner, R. & Koelle, D. Electron sampling depth and saturation effects in perovskite films investigated by soft x-ray absorption spectroscopy. *Physical Review B* **90,** 125120 (2014).

49. Stöhr, J. *NEXAFS Spectroscopy* (Springer Berlin Heidelberg, 2014).

50. Achkar, A., Regier, T., Wadati, H., Kim, Y.-J., Zhang, H. & Hawthorn, D. Bulk sensitive x-ray absorption spectroscopy free of self-absorption effects. *Physical Review B* **83,** 081106 (2011).

51. Tröger, L., Arvanitis, D., Baberschke, K., Michaelis, H., Grimm, U. & Zschech, E. Full correction of the self-absorption in soft-fluorescence extended X-ray-absorption fine structure. *Physical Review B* **46,** 3283 (1992).

52. Eisebitt, S., Böske, T., Rubensson, J.-E. & Eberhardt, W. Determination of absorption coefficients for concentrated samples by fluorescence detection. *Physical Review B* **47,** 14103 (1993).

53. Rueff, J.-P. & Shukla, A. Inelastic x-ray scattering by electronic excitations under high pressure. *Reviews of Modern Physics* **82,** 847–896 (2010).

54. Ishii, K., Tohyama, T. & Mizuki, J. Inelastic X-ray Scattering Studies of Electronic Excitations. *Journal of the Physical Society of Japan* **82,** 021015 (2013).

55. Glatzel, P., Sikora, M., Smolentsev, G. & Fernández-García, M. Hard X-ray photon-in photon-out spectroscopy. *Catalysis Today. Time-resolved and in-situ study of heterogeneous catalysts and catalytic processes using X-rays: current possibilities and future prospects, European Synchrotron Radiation Facility, Grenoble, France, 5-7 February, 2008* **145,** 294–299 (2009).

56. Kramers, H. A. & Heisenberg, W. Über die Streuung von Strahlung durch Atome. *Zeitschrift für Physik* **31,** 681–708 (1925).

57. Rueff, J.-P. & Shukla, A. A RIXS cookbook: Five recipes for successful RIXS applications. *Journal of Electron Spectroscopy and Related Phenomena. Progress in Resonant Inelastic X-Ray Scattering* **188,** 10–16 (2013).

58. Marra, P. *Theoretical Approach to Direct Resonant Inelastic X-ray Scattering on Magnets and Superconductors* PhD thesis (Technische Universität Dresden, 2016).

59. Ament, L. J., Van Veenendaal, M., Devereaux, T. P., Hill, J. P. & Van Den Brink, J. Resonant inelastic x-ray scattering studies of elementary excitations. *Reviews of Modern Physics* **83,** 705 (2011).

60. Kotani, A. & Shin, S. Resonant inelastic x-ray scattering spectra for electrons in solids. *Reviews of Modern Physics* **73,** 203 (2001).

61. Van Schooneveld, M. M., Gosselink, R. W., Eggenhuisen, T. M., Al Samarai, M., Monney, C., Zhou, K. J., Schmitt, T. & de Groot, F. M. A Multispectroscopic Study of 3d Orbitals in Cobalt Carboxylates: The High Sensitivity of 2p3d Resonant X-ray Emission Spectroscopy to the Ligand Field. *Angewandte Chemie International Edition* **52,** 1170–1174 (2013).

62. Hüfner, S. *Photoelectron Spectroscopy: Principles and Applications* (Springer, 2003).

63. Winter, B. & Faubel, M. Photoemission from liquid aqueous solutions. *Chemical Reviews* **106,** 1176–1211 (2006).

64. Manne, R. & Åberg, T. Koopmans' theorem for inner-shell ionization. *Chemical Physics Letters* **7,** 282–284 (1970).

65. Carlson, T. A. *Photoelectron and Auger Spectroscopy* (Plenum Press, New York, 1975).

66. Stöhr, J., Jaeger, R. & Rehr, J. J. Transition from Adiabatic to Sudden Core-Electron Excitation: N_2 on Ni(100). *Physical Review Letters* **51,** 821–824 (1983).

67. Hofmann, S. *Auger-and X-ray Photoelectron Spectroscopy in Materials Science: A User-oriented Guide* (Springer Science & Business Media, 2012).

68. Morgenstern, R., Niehaus, A. & Ruf, M. Angular distributions of photoelectrons. *Chemical Physics Letters* **4,** 635–638 (1970).

69. Moguilevski, A. *Ultrafast Electron Dynamics in Transition Metal Complexes Studied in Solution by Means of Time-Resolved XUV Photoemission Spectroscopy* PhD dissertation (Freie Universität Berlin, 2018).

70. Jaeschke, E. BESSY II: A state of the art synchrotron light source for Berlin-Adlershof. *Conference Proceedings, 3rd European Particle Accelerator Conference (EPAC 92)* **C920324,** 43–48 (1992).

71. Jaeschke, E., Khan, S., Kramer, D. & Schirmer, D. *Status of the high brilliance synchrotron radiation source BESSY-II* in *Proceedings Particle Accelerator Conference* **3** (1995), 1411–1413 vol.3.

72. Bakker, R. J. *Status and commissioning-results of BESSY II* 197–199 vol.1 (1999).

73. Görner, W., Hentschel, M., Müller, B., Riesemeier, H., Krumrey, M., Ulm, G., Diete, W., Klein, U. & Frahm, R. BAMline: the first hard X-ray beamline at BESSY II. *Nuclear Instruments and Methods in Physics Research Section A: Accelerators, Spectrometers, Detectors and Associated Equipment* **467-468.** 7th Int.Conf. on Synchrotron Radiation Instrumentation, 703–706 (2001).

74. Kuske, P., Abo-Bakr, M., Anders, W., Birke, T., Buerkmann, K., Dirsat, M., Dressler, O., Duerr, V., Falkenstern, F., Gericke, W., *et al.* Preparations of BESSY for Top-Up operation. *EPAC08, Genoa, Italy,* 2067 (2008).

75. Follath, R. The versatility of collimated plane grating monochromators. *Nuclear Instruments and Methods in Physics Research Section A: Accelerators, Spectrometers, Detectors and Associated Equipment* **467-468.** 7th Int.Conf. on Synchrotron Radiation Instrumentation, 418–425 (2001).

76. Jung, C., Eggenstein, F., Hartlaub, S., Follath, R., Schmidt, J., Senf, F., Weiss, M., Zeschke, T. & Gudat, W. First results of the soft X-ray microfocus beamline U41-PGM. *Nuclear Instruments and Methods in Physics Research Section A: Accelerators, Spectrometers, Detectors and Associated Equipment* **467-468.** 7th Int.Conf. on Synchrotron Radiation Instrumentation, 485–487 (2001).

77. Brandenburg, T. *The Electronic Structure of Fluorinated Systems in the Liquid Phase* PhD dissertation (Freie Universität Berlin, 2017).

78. Kachel, T. The plane grating monochromator beamline U49-2 PGM-1 at BESSY II. *Journal of Large-scale Research Facilities JLSRF* **2,** 72 (2016).

79. Aziz, E. F., Xiao, J., Golnak, R. & Tesch, M. LiXEdrom: High Energy Resolution RIXS Station dedicated to Liquid Investigation at BESSY II. *Journal of Large-scale Research Facilities JLSRF* **2,** 80 (2016).

80. Lange, K. M., Könnecke, R., Ghadimi, S., Golnak, R., Soldatov, M. A., Hodeck, K. F., Soldatov, A. & Aziz, E. F. High resolution X-ray emission spectroscopy of water and aqueous ions using the micro-jet technique. *Chemical Physics* **377,** 1–5 (2010).

81. Seidel, R., Thürmer, S. & Winter, B. Photoelectron Spectroscopy Meets Aqueous Solution: Studies from a Vacuum Liquid Microjet. *The Journal of Physical Chemistry Letters* **2,** 633–641 (2011).

82. Thürmer, S. *Inquiring Photoelectrons about the Dynamics in Liquid Water* PhD dissertation (Universität Potsdam, 2012).

83. Seidel, R. *Electronic-Structure Interactions in Aqueous Solutions: A Liquid-Jet Photoelectron Spectroscopy Study* PhD dissertation (Technischen Universität Berlin, 2011).

84. Qiao, R., Xia, Y., Feng, X., Macdougall, J., Pepper, J., Armitage, K., Borsos, J., Knauss, K. G., Lee, N., Allézy, A., *et al.* Soft x-ray spectroscopy of high pressure liquid. *Review of Scientific Instruments* **89,** 013114 (2018).

85. Kolmakov, A., Dikin, D. A., Cote, L. J., Huang, J., Abyaneh, M. K., Amati, M., Gregoratti, L., Günther, S. & Kiskinova, M. Graphene oxide windows for in situ environmental cell photoelectron spectroscopy. en. *Nature Nanotechnology* **6,** 651–657 (2011).

86. Zemlyanov, D. Electron spectroscopy: A new window opens. en. *Nature Nanotechnology* **6,** 612–613 (2011).

87. Petit, T., Ren, J., Choudhury, S., Golnak, R., Lalithambika, S. S. N., Tesch, M. F., Xiao, J. & Aziz, E. F. X-Ray Absorption Spectroscopy of TiO_2 Nanoparticles in Water Using a Holey Membrane-Based Flow Cell. en. *Advanced Materials Interfaces* **4,** 1700755 (2017).

88. Faubel, M., Schlemmer, S. & Toennies, J. A molecular beam study of the evaporation of water from a liquid jet. *Zeitschrift fuer Physik D Atoms, Molecules and Clusters* **10,** 269–277 (1988).

89. Ali, H., Seidel, R., Pohl, M. N. & Winter, B. Molecular species forming at the α-Fe_2O_3 nanoparticle-aqueous solution interface. *Chemical Science* **9,** 4511–4523 (19 2018).

90. Wilson, K. R., Rude, B. S., Smith, J., Cappa, C., Co, D., Schaller, R., Larsson, M., Catalano, T. & Saykally, R. Investigation of volatile liquid surfaces by synchrotron x-ray spectroscopy of liquid microjets. *Review of Scientific Instruments* **75,** 725–736 (2004).

91. Golnak, R. *Investigation of the Electronic Structure of Transition Metal-Ions in Solution from Aqua-Complexes to Porphyrins* PhD dissertation (Freie Universität Berlin, 2016).

92. Neese, F. The ORCA program system. *Wiley Interdisciplinary Reviews: Computational Molecular Science* **2,** 73–78 (2012).

93. Roemelt, M., Maganas, D., DeBeer, S. & Neese, F. A combined DFT and restricted open-shell configuration interaction method including spin-orbit coupling: Application to transition metal L-edge X-ray absorption spectroscopy. *The Journal of Chemical Physics* **138,** 204101 (2013).

94. Ray, K., DeBeer George, S., Solomon, E. I., Wieghardt, K. & Neese, F. Description of the Ground-State Covalencies of the Bis (dithiolato) Transition-Metal Complexes from X-ray Absorption Spectroscopy and Time-Dependent Density-Functional Calculations. *Chemistry-A European Journal* **13,** 2783–2797 (2007).

95. Miertus, S., Scrocco, E. & Tomasi, J. Comparison of polarizable continuum model and quantum mechanics/molecular mechanics solute electronic polarization: study of the optical and magnetic properties of diazines in water. *Chemical Physics* **55,** 117 (1981).

96. Miertus, S. & Tomasi, J. Approximate evaluations of the electrostatic free energy and internal energy changes in solution processes. *Chemical Physics* **65,** 239–245 (1982).

97. Klamt, A. & Schürmann, G. COSMO: a new approach to dielectric screening in solvents with explicit expressions for the screening energy and its gradient. *Journal of the Chemical Society, Perkin Transactions 2,* 799–805 (1993).

98. Van Lenthe, E. v., Snijders, J. & Baerends, E. The zero-order regular approximation for relativistic effects: The effect of spin–orbit coupling in closed shell molecules. *The Journal of Chemical Physics* **105,** 6505–6516 (1996).

99. Jensen, F. *Introduction to Computational Chemistry* Second edition (Wiley, 2007).

100. Brewer, W., Haken, H. & Wolf, H. *Molecular Physics and Elements of Quantum Chemistry: Introduction to Experiments and Theory* (Springer Berlin Heidelberg, 2013).

101. Kohn, W. Nobel Lecture: Electronic structure of matter—wave functions and density functionals. *Reviews of Modern Physics* **71,** 1253 (1999).

102. Townsend, J., Kirkland, J. K. & Vogiatzis, K. D. in *Mathematical Physics in Theoretical Chemistry* 63–117 (Elsevier, 2019).

103. Shavitt, I. The history and evolution of configuration interaction. *Molecular Physics* **94,** 3–17 (1998).

104. Ritz, W. Über eine neue Methode zur Lösung gewisser Variationsprobleme der mathematischen Physik. *Journal für die reine und angewandte Mathematik* **135,** 1–61 (1909).

105. Maganas, D., Roemelt, M., Hävecker, M., Trunschke, A., Knop-Gericke, A., Schlögl, R. & Neese, F. First principles calculations of the structure and V L-edge X-ray absorption spectra of V_2O_5 using local pair natural orbital coupled cluster theory and spin–orbit coupled configuration interaction approaches. *Physical Chemistry Chemical Physics* **15,** 7260–7276 (2013).

106. Maganas, D., Roemelt, M., Weyhermüller, T., Blume, R., Hävecker, M., Knop-Gericke, A., DeBeer, S., Schlögl, R. & Neese, F. L-edge X-ray absorption study of mononuclear vanadium complexes and spectral predictions using a restricted open shell configuration interaction ansatz. *Physical Chemistry Chemical Physics* **16,** 264–276 (2014).

107. Fiolhais, C., Nogueira, F. & Marques, M. *A Primer in Density Functional Theory* (Springer Berlin Heidelberg, 2003).

108. Kryachko, E. S. & Ludena, E. V. Density functional theory: foundations reviewed. *Physics Reports* **544,** 123–239 (2014).

109. Löwdin, P.-O. in *Advances in Quantum Chemistry* 185–199 (Elsevier, 1970).

110. Neese, F. A critical evaluation of DFT, including time-dependent DFT, applied to bioinorganic chemistry. *JBIC Journal of Biological Inorganic Chemistry* **11,** 702–711 (2006).

111. Casida, M. E. Time-dependent density-functional theory for molecules and molecular solids. *Journal of Molecular Structure: THEOCHEM* **914,** 3–18 (2009).

112. George, S. D., Petrenko, T. & Neese, F. Time-dependent density functional calculations of ligand K-edge X-ray absorption spectra. *Inorganica Chimica Acta* **361,** 965–972 (2008).

113. Lalithambika, S. S. N., Atak, K., Seidel, R., Neubauer, A., Brandenburg, T., Xiao, J., Winter, B. & Aziz, E. F. Chemical bonding in aqueous hexacyano cobaltate from photon- and electron-detection perspectives. en. *Scientific Reports* **7,** 40811 (2017).

114. Atkins, P. & Paula, J. d. *Atkins' Physical Chemistry* en (OUP Oxford, 2010).

115. Zhou, X., Li, F., Li, H., Zhang, B., Yu, F. & Sun, L. Photocatalytic Water Oxidation by Molecular Assemblies Based on Cobalt Catalysts. *ChemSusChem* **7,** 2453–2456 (2014).

116. Velasco-Velez, J.-J., Wu, C. H., Pascal, T. A., Wan, L. F., Guo, J., Prendergast, D. & Salmeron, M. The structure of interfacial water on gold electrodes studied by x-ray absorption spectroscopy. *Science,* 1259437 (2014).

117. Griffith, W. Cyanide complexes of the early transition metals (groups IVa-VIIa). *Coordination Chemistry Reviews* **17,** 177–247 (1975).

118. Griffith, W. Cyanide complexes of the transition metals. *Quarterly Reviews, Chemical Society* **16,** 188–207 (1962).

119. Gray, H. B. & Beach, N. The Electronic Structures of Octahedral Metal Complexes. I. Metal Hexacarbonyls and Hexacyanides. *Journal of the American Chemical Society* **85,** 2922–2927 (1963).

120. Alexander, J. J. & Gray, H. B. Electronic structures of hexacyanometalate complexes. *Journal of the American Chemical Society* **90,** 4260–4271 (1968).

121. Hocking, R. K., Wasinger, E. C., de Groot, F. M., Hodgson, K. O., Hedman, B. & Solomon, E. I. Fe L-edge XAS studies of $K_4[Fe(CN)_6]$ and $K_3[Fe(CN)_6]$: a direct probe of back-bonding. *Journal of the American Chemical Society* **128,** 10442–10451 (2006).

122. Lundberg, M., Kroll, T., DeBeer, S., Bergmann, U., Wilson, S. A., Glatzel, P., Nordlund, D., Hedman, B., Hodgson, K. O. & Solomon, E. I. Metal–Ligand Covalency of Iron Complexes from High-Resolution Resonant Inelastic X-ray Scattering. *Journal of the American Chemical Society* **135,** 17121–17134 (2013).

123. Golnak, R., Xiao, J., Atak, K., Unger, I., Seidel, R., Winter, B. & Aziz, E. F. Undistorted X-ray Absorption Spectroscopy Using s-Core-Orbital Emissions. *The Journal of Physical Chemistry A* **120,** 2808–2814 (2016).

124. Davis, L. Photoemission from transition metals and their compounds. *Journal of Applied Physics* **59,** R25–R64 (1986).

125. Winter, B. Liquid microjet for photoelectron spectroscopy. *Nuclear Instruments and Methods in Physics Research Section A: Accelerators, Spectrometers, Detectors and Associated Equipment* **601,** 139–150 (2009).

126. Hanwell, M. D., Curtis, D. E., Lonie, D. C., Vandermeersch, T., Zurek, E. & Hutchison, G. R. Avogadro: an advanced semantic chemical editor, visualization, and analysis platform. *Journal of Cheminformatics* **4,** 17 (2012).

127. Seidel, R., Thürmer, S., Moens, J., Geerlings, P., Blumberger, J. & Winter, B. Valence Photoemission Spectra of Aqueous $Fe^{2+/3+}$ and $[Fe(CN)_6]^{4-/3-}$ and Their Interpretation by DFT Calculations. *The Journal of Physical Chemistry B* **115,** 11671–11677 (2011).

128. Weinhardt, L., Blum, M., Fuchs, O., Benkert, A., Meyer, F., Bär, M., Denlinger, J., Yang, W., Reinert, F. & Heske, C. RIXS investigations of liquids, solutions, and liquid/solid interfaces. *Journal of Electron Spectroscopy and Related Phenomena* **188,** 111–120 (2013).

129. Zhao, Y. & Truhlar, D. G. The M06 suite of density functionals for main group thermochemistry, thermochemical kinetics, noncovalent interactions, excited states, and transition elements: two new functionals and systematic testing of four M06-class functionals and 12 other functionals. *Theoretical Chemistry Accounts: Theory, Computation, and Modeling (Theoretica Chimica Acta)* **120,** 215–241 (2008).

130. Weigend, F. & Ahlrichs, R. Balanced basis sets of split valence, triple zeta valence and quadruple zeta valence quality for H to Rn: Design and assessment of accuracy. *Physical Chemistry Chemical Physics* **7,** 3297–3305 (2005).

131. Becke, A. D. Density-functional exchange-energy approximation with correct asymptotic behavior. *Physical Review A* **38,** 3098 (1988).

132. Becke, A. D. Density-functional thermochemistry. III. The role of exact exchange. *The Journal of Chemical Physics* **98,** 5648–5652 (1993).

133. Baerends, E., Ellis, D. & Ros, P. Self-consistent molecular Hartree—Fock—Slater calculations I. The computational procedure. *Chemical Physics* **2,** 41–51 (1973).

134. Dunlap, B. I., Connolly, J. & Sabin, J. On some approximations in applications of X α theory. *The Journal of Chemical Physics* **71,** 3396–3402 (1979).

135. Vahtras, O., Almlöf, J. & Feyereisen, M. Integral approximations for LCAO-SCF calculations. *Chemical Physics Letters* **213,** 514–518 (1993).

136. Eichkorn, K., Treutler, O., Öhm, H., Häser, M. & Ahlrichs, R. Auxiliary basis sets to approximate Coulomb potentials. *Chemical Physics Letters* **240,** 283–290 (1995).

137. Eichkorn, K., Weigend, F., Treutler, O. & Ahlrichs, R. Auxiliary basis sets for main row atoms and transition metals and their use to approximate Coulomb potentials. *Theoretical Chemistry Accounts: Theory, Computation, and Modeling (Theoretica Chimica Acta)* **97,** 119–124 (1997).

138. Weigend, F. Accurate Coulomb-fitting basis sets for H to Rn. *Physical Chemistry Chemical Physics* **8,** 1057–1065 (2006).

139. Sinnecker, S., Rajendran, A., Klamt, A., Diedenhofen, M. & Neese, F. Calculation of solvent shifts on electronic g-tensors with the conductor-like screening model (COSMO) and its self-consistent generalization to real solvents (Direct COSMO-RS). *The Journal of Physical Chemistry A* **110,** 2235–2245 (2006).

140. Thürmer, S., Seidel, R., Eberhardt, W., Bradforth, S. E. & Winter, B. Ultrafast hybridization screening in Fe^{3+} aqueous solution. *Journal of the American Chemical Society* **133,** 12528–12535 (2011).

141. Sun, Z.-Z., Zheng, K.-M., Li, Q.-S. & Li, Z.-S. Rational design of Co-based redox mediators for dye-sensitized solar cells by density functional theory. *RSC Advances* **4,** 31544–31551 (2014).

142. Atak, K., Golnak, R., Xiao, J., Pflüger, M., Brandenburg, T., Winter, B. & Aziz, E. F. Co(III) protoporphyrin IX chloride in solution: spin-state and metal coordination revealed from resonant inelastic X-ray scattering and electronic structure calculations. *Physical Chemistry Chemical Physics* **17,** 3409–3414 (2015).

143. Gütlich, P., Gaspar, A. B. & Garcia, Y. Spin state switching in iron coordination compounds. *Beilstein Journal of Organic Chemistry* **9,** 342–391 (2013).

144. Long Her, J., Matsuda, Y. H., Nakano, M., Niwa, Y. & Inada, Y. Magnetic field-induced spin-crossover transition in [MnIII (taa)] studied by x-ray absorption spectroscopy. *Journal of Applied Physics* **111,** 053921 (2012).

145. Nelyubina, Y., Polezhaev, A., Pavlov, A., Aleshin, D., Savkina, S., Efimov, N., Aliev, T. & Novikov, V. Intramolecular Spin State Locking in Iron (II) 2, 6-Di (pyrazol-3-yl) pyridine Complexes by Phenyl Groups: An Experimental Study. *Magnetochemistry* **4,** 46 (2018).

146. Halcrow, M. A. The Effect of Ligand Design on Metal Ion Spin State—Lessons from Spin Crossover Complexes. *Crystals* **6,** 58 (2016).

147. Masuda, Y. & Yamatera, H. Rotational motions of the tris(1,10-phenanthroline) and tris(2,2'-bipyridine) complexes of ruthenium(II) and cobalt(III) ions in solution. *The Journal of Physical Chemistry* **88,** 3425–3431 (1984).

148. PURELAB. *ELGA LabWater* `http://www.elgalabwater.com/products/purelab` (2017).

149. Potze, R. H., Sawatzky, G. A. & Abbate, M. Possibility for an intermediate-spin ground state in the charge-transfer material $SrCoO_3$. *Physical Review B* **51,** 11501–11506 (1995).

150. Stevens, J. S., Newton, L. K., Jaye, C., Muryn, C. A., Fischer, D. A. & Schroeder, S. L. M. Proton Transfer, Hydrogen Bonding, and Disorder: Nitrogen Near-Edge X-ray Absorption Fine Structure and X-ray Photoelectron Spectroscopy of Bipyridine–Acid Salts and Co-crystals. *Crystal Growth & Design* **15,** 1776–1783 (2015).

151. Bedoya-Pinto, A., Miralles, S. G., Vélez, S., Atxabal, A., Gargiani, P., Valvidares, M., Casanova, F., Coronado, E. & Hueso, L. E. Interface-Assisted Sign Inversion of Magnetoresistance in Spin Valves Based on Novel Lanthanide Quinoline Molecules. *Advanced Functional Materials* **28,** 1702099 (2018).

152. Magnuson, M., Butorin, S. M., Guo, J.-H. & Nordgren, J. Electronic structure investigation of CoO by means of soft x-ray scattering. *Physical Review B* **65,** 205106 (2002).

153. Nia, N. Y., Farahani, P., Sabzyan, H., Zendehdel, M. & Oftadeh, M. A combined computational and experimental study of the $[Co(bpy)_3]^{2+/3+}$ complexes as one-electron outer-sphere redox couples in dye-sensitized solar cell electrolyte media. *Physical Chemistry Chemical Physics* **16,** 11481–11491 (2014).

154. Weinhardt, L., Weigand, M., Fuchs, O., Bär, M., Blum, M., Denlinger, J. D., Yang, W., Umbach, E. & Heske, C. Nuclear dynamics in the core-excited state of aqueous ammonia probed by resonant inelastic soft x-ray scattering. *Physical Review B* **84,** 104202 (2011).

155. O'Shea, J. N., Handrup, K., Temperton, R. H., Gibson, A. J., Nicolaou, A. & Jaouen, N. Exploring ultra-fast charge transfer and vibronic coupling with N 1s RIXS maps of an aromatic molecule coupled to a semiconductor. *The Journal of Chemical Physics* **147,** 134705 (2017).

156. Magnuson, M., Yang, L., Guo, J. .-.-H., Såthe, C., Agui, A., Nordgren, J., Luo, Y., Ågren, H., Johansson, N., Salaneck, W. R., Horsburgh, L. E. & Monkman, A. P. Resonant inelastic soft X-ray scattering spectra at the nitrogen and carbon K-edges of poly(pyridine-2,5-diyl). *Journal of Electron Spectroscopy and Related Phenomena* **101-103,** 573–578 (1999).

157. Plakhutin, B. N. & Davidson, E. R. Koopmans' Theorem in the Restricted Open-Shell Hartree-Fock Method. 1. A Variational Approach. *The Journal of Physical Chemistry A* **113,** 12386–12395 (2009).

158. Plakhutin, B. N. & Davidson, E. R. Canonical form of the Hartree-Fock orbitals in open-shell systems. *The Journal of Chemical Physics* **140,** 014102 (2014).

159. Drzeżdżon, J., Sikorski, A., Chmurzyński, L. & Jacewicz, D. New type of highly active chromium (III) catalysts containing both organic cations and anions designed for polymerization of beta-olefin derivatives. *Scientific reports* **8,** 2315 (2018).

160. Ozdilek, Z. Teaching the properties of chromium's oxidation states with a case study method. *Chemistry Education Research and Practice* **16,** 39–52 (2015).

161. Hermann, G., Pohl, V., Tremblay, J. C., Paulus, B., Hege, H.-C. & Schild, A. ORBKIT: A modular python toolbox for cross-platform postprocessing of quantum chemical wavefunction data. *Journal of Computational Chemistry* **37,** 1511–1520 (2016).

162. Humphrey, W., Dalke, A. & Schulten, K. VMD – Visual Molecular Dynamics. *Journal of Molecular Graphics* **14,** 33–38 (1996).

163. Stone, J. *An Efficient Library for Parallel Ray Tracing and Animation* MA thesis (Computer Science Department, University of Missouri-Rolla, 1998).

164. Wernet, P., Kunnus, K., Schreck, S., Quevedo, W., Kurian, R., Techert, S., de Groot, F. M. F., Odelius, M. & Föhlisch, A. Dissecting Local Atomic and Intermolecular Interactions of Transition-Metal Ions in Solution with Selective X-ray Spectroscopy. *The Journal of Physical Chemistry Letters* **3,** 3448–3453 (2012).

165. Gotz, M. D., Soldatov, M. A., Lange, K. M., Engel, N., Golnak, R., Könnecke, R., Atak, K., Eberhardt, W. & Aziz, E. F. Probing Coster–Kronig Transitions in Aqueous Fe2+ Solution Using Inverse Partial and Partial Fluorescence Yield at the L-Edge. *The Journal of Physical Chemistry Letters* **3,** 1619–1623 (2012).

Acknowledgments

I acknowledge my indebtedness to all those who have offered their cooperation and guidance in the completion of my dissertation work.

First and foremost I express my sincere gratitude to Dr. Bernd Winter for his kindness to accept me as a Ph.D. student. This work would not have been complete without his constructive criticism and guidance. A major portion of this thesis is about photoelectron spectroscopy from aqueous solution. Bernd's vast knowledge and experience in the field of liquid-jet photoelectron spectroscopy were extremely resourceful.

I express my heartfelt thanks to Prof. Dr. Wolfgang Kuch for his goodwill to co-supervise this thesis. My sincere thanks for inviting me to his yearly group meetings and providing me a platform for presenting my work and getting involved in fruitful discussions.

I express my immense gratitude to Dr. Kaan Atak for being my day-to-day supervisor who regularly monitored this work for the last four years. His patience and willingness to share knowledge were crucial for the completion of this work. All the computations presented in this would not have been possible without his support. I will be grateful for all his support both inside and outside of the academia; I will cherish our friendship for the rest of my life.

Thanks to Dr. Tim Brandenburg for introducing me to the group, and also helping me with German administrative matters. Thanks for all the help while I was in the hospital. I am sure we will have a beautiful friendship for a long time.

I offer my thanks to Dr. Ronny Golnak for his help and valuable inputs during beamtimes and throughout this thesis work. His knowledge about beamlines and the LiXEdrom experimental station were crucial for the completion of this thesis.

I also thank Dr. Robert Seidel for introducing me to liquid-jet photoemission technique. His support was invaluable for the liquid photoemission measurement of certain samples, and also for the data analysis.

I would also like to thank Dr. Antje Neubauer for supervising me for the first six months of my Ph.D. Her support and knowledge were crucial for the initial take-off of this project. Thanks for making me feel comfortable with my first beamtime.

Next, I sincerely thank Dr. Iain Wilkinson, his support and advice as the EM-IMM institute director was crucial in securing financial aid when an extension was necessary for this project.

Dr. Matthias Berg was very inspirational in the latter part of this work. His opinions and perspectives as a computational chemist always introduced an eagerness in my mind about various theoretical methods. I thank him for all his support.

Many thanks to Dr. Jie Xiao, Dr. Marc F. Tesch and Dr. Tristan Petit for their support during beamtimes. I also thank my fellow Ph.D. students for their support.

I would like to thank the European Commission for the scholarship grant as part of

the ERASMUS MUNDUS (EMINTE) scholarship program. Also, my sincere thanks to Mrs. Nicole Putbrese, coordinator at Freie University Berlin's international office and also to other fellow staffs (Stefanie Böhler, Stefanie Schmidt, and Nicole Lorenz) for all the support. I also offer my thanks to EMINTE coordinating team at Lund University Sweden for all their assistance. Many thanks also to the management of Helmholtz-Zentrum Berlin for providing me a guest status, final phase financial assistance, and most importantly for giving access to the outstanding BESSY II synchrotron research facility.

Last but not least, I express my thanks to my family and all my friends who have directly or indirectly supported and encouraged me during this period.

List of publications

Part of this thesis

- **S. S. N. Lalithambika**, K. Atak, R. Seidel, A. Neubauer, T. Brandenburg, J. Xiao, B. Winter, E. F. Aziz. Chemical Bonding in Aqueous Hexacyano Cobaltate from Photon- and Electron-Detection Perspectives *Scientific Reports*, 2017, Vol 7, page 40811
- **S. S. N. Lalithambika**, R. Golnak, B. Winter, and K. Atak. Electronic Structure of $[Co(bpy)_3]^{2+/3+}$ Electron Mediators in Aqueous Solution *Inorganic Chemistry*, 2019, Vol 58, Issue 8, page 4731-4740
- Matthias Berg, **Sreeju Sreekantan Nair Lalithambika**, Kaan Atak. RIXS Investigation of Aqueous Hexacyanochromate (in preparation)

Contribution to other publications

- T. Petit, J. Ren, S. Choudhury, R. Golnak, **S. S. N. Lalithambika**, M. F. Tesch, J. Xiao, E. F. Aziz. X-Ray Absorption Spectroscopy of TiO_2 Nanoparticles in Water Using a Holey Membrane-Based Flow Cell *Advanced Materials Interfaces*, 2017, Vol 4, Issue 23, Page 1700755
- T. Brandenburg, R. Golnak, M. Nagasaka, K. Atak, **S. S. N. Lalithambika**, N. Kosugi, E. F. Aziz. Impacts of Conformational Geometries in Fluorinated Alkanes *Scientific Reports*, 2016, Vol 6, Page 31382

Selbstständigkeitserklärung

Hiermit erkläre ich, dass ich alle Hilfsmittel und Hilfen angegeben habe und versichere, dass ich auf dieser Grundlage die Arbeit selbständig verfasst habe.
Meine Arbeit ist nicht schon einmal in einem früheren Promotionsverfahren eingereicht worden.

Sreeju Sreekantan Nair Lalithambika
Berlin, 19.03.2019